FINAL REPORT

SPATIAL AND TEMPORAL DISTRIBUTION OF BOUNDARY SHEAR STRESS IN OPEN CHANNEL FLOWS

(Grant No. ENG76-05896)

Prepared for

National Science Foundation
Washington, D.C.

Prepared by

Civil Engineering Department
Engineering Research Center
Colorado State University
Fort Collins, Colorado 80523

D. B. Simons
R. M. Li
J. D. Schall

September 1979

CER79-80DBS-RML-JDS16

FINAL REPORT

SPATIAL AND TEMPORAL DISTRIBUTION OF BOUNDARY SHEAR STRESS IN OPEN CHANNEL FLOWS

(Grant No. ENG76-05896)

Prepared for

National Science Foundation
Washington, D.C.

Prepared by

Civil Engineering Department
Engineering Research Center
Colorado State University
Fort Collins, Colorado 80523

D. B. Simons
R. M. Li
J. D. Schall

September 1979

CER79-80DBS-RML-JDS16

AUTHORIZATION

This research was sponsored by the National Science Foundation under the Research Grant No. ENG7605896. The project dealt with the spatial and temporal distribution of boundary shear stress in rigid boundary open channel flows. The investigations included theoretical and experimental approachs. The period of the project was from November 1976 to October 1978. The principal investigators at Colorado State University were Daryl B. Simons and Ruh-Ming Li.

In accordance with the National Science Foundation grant policy, a summary of the project objectives, the techniques used and the findings and implications of the research has been submitted (NSF form 98A). This report is provided in addition to form 98A and contains a detailed account of the investigation.

NATIONAL SCIENCE FOUNDATION
Washington, D.C. 20550

FINAL PROJECT REPORT

NSF FORM 98A

PLEASE READ INSTRUCTIONS ON REVERSE BEFORE COMPLETING

PART I–PROJECT IDENTIFICATION INFORMATION

1. Institution and Address	2. NSF Program	3. NSF Award Number
Colorado State University Fort Collins, Colorado 80523	Water Resources, Urban, and Environmental Engineering	NSF ENG76-05896
	4. Award Period From 11/15/76 To 4/30/79	5. Cumulative Award Amount $90,300

6. Project Title

Spatial and Time Distribution Boundary Shear Stress in Open Channel Flows

PART II–SUMMARY OF COMPLETED PROJECT *(FOR PUBLIC USE)*

Analytical and experimental investigations were conducted to evaluate the characteristics of turbulent boundary shear stress in open channel flows. Experimental studies were conducted in a rigid boundary, variable laboratory flume with hydraulically smooth roughness. The spatial and temporal distributions of turbulent boundary shear stress were obtained with hot-film anemometry and computer data acquisition techniques. A sequence of four experiments were conducted to determine: 1) the cross streamwise variation of the boundary shear stress characteristics for different channel shapes, 2) the influence of non-uniform flow conditions on the streamwise mean boundary shear stress, 3) the characteristics of turbulent velocity fluctuations near the channel boundary, and 4) the relationship of the near wall turbulent velocity and boundary shear stress processes, and the influence of secondary current on the spatial distribution of mean boundary shear stress. Using measured data probablistic structures describing the processes involved were developed.

Results indicated the general trends of the spatial distribution of boundary shear stress can be mathematically described and the temporal distribution of instantaneous boundary shear stress resembles a lognormal distribution. An analytical model of the turbulent intensity of velocity was developed and tested against experimental data with excellent results. The measured correlation of the instantaneous velocity and boundary shear stress was found to decrease as relative depth increased, and a qualitative relationship between secondary current patterns and mean boundary shear stress patterns was observed.

As a result of this investigation several significant contributions were made to the field of engineering hydraulics. An increased awareness and understanding was obtained of the complicated mechanisms that occur in turbulent open channel flow. Mathematical models of some of these mechanisms were developed and are available for use as tools in prediction and design. Knowledge gained has application to the processes of sediment transport, incipient motion, solid particle settlement, riprap design and to the design of hydraulically stable channels.

PART III–TECHNICAL INFORMATION *(FOR PROGRAM MANAGEMENT USES)*

1. ITEM *(Check appropriate blocks)*	NONE	ATTACHED	PREVIOUSLY FURNISHED	TO BE FURNISHED SEPARATELY TO PROGRAM	
				Check (✓)	Approx. Date
a. Abstracts of Theses		X			
b. Publication Citations		X			
c. Data on Scientific Collaborators		X			
d. Information on Inventions	X				
e. Technical Description of Project and Results				X	Sept. 1979
f. Other *(specify)*					

2. Principal Investigator/Project Director Name *(Typed)*	3. Principal Investigator/Project Director Signature	4. Date
Daryl B. Simons, Associate Dean Ruh-Ming Li, Associate Professor	D.B. Simons R.M. Li	9-13-7

NSF Form 98A (5-78) Supersedes All Previous Editions

Form Approved OMB No. 99R0

ABSTRACT

SPATIAL AND TEMPORAL DISTRIBUTION OF BOUNDARY

SHEAR STRESS IN OPEN CHANNEL FLOWS

The objective of this project was to develop a better understanding of turbulent boundary shear stress processes. Experimental investigation of the spatial and temporal distributions of boundary shear stress were conducted using hot-film anemometry techniques.

Spatial variation and turbulence characteristics of boundary shear stress in the cross-streamwise direction were investigated in a rigid boundary variable geometry flume. Three trapezoidal and one rectangular cross section with bottom widths of eight inches were considered. Discharge rates ranged from 2832 cm^3/s to 14158 cm^3/s. Experimental results verified Lane's relation of maximum mean tractive force for the channel sides and bottom. Probability density estimates of turbulent boundary shear stress at a point were consistently skewed and resembled a lognormal distribution.

Streamwise variation of boundary shear stress was measured in the nonuniform flow behind a weir. Experimental data compared well to analytical computations based on backwater calculations, providing the pressure distribution remained hydrostatic.

An analytical model for prediction of turbulent intensity of velocity fluctuations was calibrated and tested. Prediction of velocity fluctuations near the wall is important to understanding turbulent boundary shear stress processes. Probability density functions of the

experimentally measured longitudinal and vertical components of velocity were approximately Gaussian distributed. Measured turbulent intensity compared well to values predicted by the model.

Correlation analysis between instantaneous velocity and boundary shear stress indicated a strong similiarity of the time series near the wall. As the relative depth increased, the correlation coefficient between the signals decreased. Secondary current patterns of mean velocity were observed to influence the mean boundary shear stress pattern around the wetted perimeter of the channel.

ACKNOWLEDGEMENTS

Successful completion of this research project is due to the effort and cooperation of many individuals. The writers wish to acknowledge some of these people and their contributions. The expertise of Professor V. A. Sandborn was invaluable during the laboratory work and is greatly appreciated. Special thanks are due to Tai-Fang Lu for her assitance in data analysis. The shop foreman, Mr. Ewald Patzer, and machinist Karl Albrecht did an excellent job in constructing the laboratory equipment. Appreciation is extended to Debbie Price for reviewing and editing the manuscript, and to technical typing supervisor, Arlene Nelson and typist, Sue Barnes, for their careful preparation of the manuscript. Hanae Akari and her staff in the drafting office provided the excellent drawings on short notice.

This work was supported by the National Science Foundation under Grant No. ENG76-05896.

TABLE OF CONTENTS

LIST OF FIGURES

LIST OF TABLES

LIST OF PLATES

I. EXECUTIVE SUMMARY

1.1 Importance of Research

The flow of water along an alluvial channel bottom produces forces that initiate sediment motion. The amount of sediment entrained depends on the characteristics of these forces, referred to as hydrodynamic forces in literature on channel stability. For a given sediment particle a critical or threshold value of the hydrodynamic forces must be reached before sediment motion begins. The magnitude of force necessary to initiate motion depends on grain size and bed material properties. After traveling some distance downstream, sediment entrained with the flow can also settle back to the bed surface. The process of sediment transport is characterized by this cycle of motion and rest. The rates and frequencies at which the cycle occurs are random variables depending on sediment characteristics, flow conditions, channel shape, turbulent velocity fluctuations and many other factors. The complexity of the problem makes design of a stable channel and prediction of geomorphic changes in a river bed difficult. According to Lane (1), "A stable channel is an unlined earth channel (a) which carries water, (b) the banks and bed of which are not scoured objectionably by moving water, and (c) in which objectionable deposits of sediment do not occur." Knowledge of the hydrodynamic forces at the channel bank and bottom is essential for the proper design of a stable channel cross section.

1.2 Definition of the Problem

Tractive force, or boundary shear stress, is the tangential component of the hydrodynamic forces acting in a direction parallel to the channel bottom. (Unless stated otherwise, boundary shear stress and shear stress are considered synonymous in this report.) In steady

uniform flow the theoretical tractive force is related to channel bed slope, hydraulic radius and unit weight of the fluid. According to the theoretical derivation the tractive force is assumed uniformly distributed over the channel perimeter. However, it is known that such forces are not uniformly distributed nor are they constant at a given location. The tractive force is a turbulent quantity consisting of a fluctuating component superimposed on the mean value. Stability of a channel will depend not only on spatial distribution of the mean value, but also on the instantaneous values and statistical characteristics at a given point. The influence of turbulent velocity fluctuations on the shear flow structure and thus on the turbulent wall shear stress was qualitatively stated by Blinco (2). Turbulence affects the processes of sediment transport, incipient motion and solid particle sediment and is important in the design of stable channels. Additionally, the influence of the mean velocity distribution and secondary current has been suggested to be significant in determining the spatial distribution of the boundary shear stress (18). The nonuniform spatial distribution of mean boundary shear stress and the stochastic nature of the instantaneous values creates a very complex turbulent structure near the wall boundary. The relation of the mean and instantaneous boundary shear stress is important if one is to understand open channel flow processes.

Prediction of spatial distribution of mean boundary shear stress has relied on mathematical formulations and semi-empirical relationships. The models are derived from the assumption that local boundary shear stress is expressible in terms of a postulated velocity distribution in the channel cross section, or by analogy to laminar flow. The influence of channel bank resistance, secondary current and the turbulent

characteristics of the instantaneous component of shear stress are neglected. Due to a lack of systematic quantitative and qualitative information on the spatial and time variation of the tractive forces in channels, the available design of stability criterion is reduced to empirical relationships and trial and error. This conventional deterministic approach to stable channel design, taking parameters as exact known values, attempts to cope with uncertainty by means of an overall stability criterion. However, the implied sense of stability associated with a stability criterion may be false, due to the randomness of the tractive force. Despite immense interest in boundary shear stress processes, no systematic information is available that describes the instantaneous boundary shear stress in terms of its spatial and time distributions. The effects of channel geometry and hydraulic condition on these distributions is inadequate for design purposes.

1.3 Scope of Work

Lack of systematic, consistent and complete experimental data has hindered development of a more comprehensive understanding of free surface turbulent flows. The complexity of the turbulent boundary shear stress process makes direct mathematical formulation extremely difficult. By investigating the spatial and time distribution of the boundary shear stress through a series of systematic experiments, an improved understanding of processes that are involved can be achieved. To study the problem experimentally requires simplifications. Before investigating alluvial channel systems, where sediment transport processes are important, a thorough understanding of boundary shear stress in rigid channels must be obtained. Rigid channel results would not be directly applicable to sediment transport problems; however, it is a necessary simplification

in a long-term research effort, where the final objective is a complete understanding of alluvial systems. Therefore, the experimental work of this project was confined to a rigid boundary system. Coupling the experimental effort with mathematical modeling can give new insight into the nature of boundary shear stress in open channel flow.

Hot-film anemometry is a heat transfer technique for measurement of turbulence properties in a fluid flow field. Anemometry techniques have proven invaluable as research tools for turbulence characteristics due to the extremely rapid response of a heated platinum element measuring probe placed in the flow field. Originally, the technique was limited to use in air flows. However, technological improvements in the design of measuring probes have expanded the capabilities to allow efficient operation in rigid boundary water flows as well.

Recent work at Colorado State University indicates that the statistical character of the boundary shear stress process can be determined by anemometry techniques using flush surface hot-film sensors (2). Use of this type of sensor is well suited to the measurement of the local boundary shear stress in steady uniform and nonuniform flows with smooth hydraulic boundaries. Hot-film velocity anemometer systems have also proven valuable for measurement of turbulent velocity. These techniques were used in this investigation to study the characteristics of turbulent boundary shear stress. A sequence of four separate but related experiments were conducted to determine: 1) the cross-streamwise variation of mean boundary shear stress in different channel shapes, 2) the influence of nonuniform flow conditions on the streamwise boundary shear stress distribution, 3) the characteristics of turbulent velocity fluctuations, and 4) the relationship of the turbulent velocity and

boundary shear stress processes and the influence of secondary current on the spatial distribution of mean boundary shear stress.

The cross-streamwise variation of boundary shear stress was studied using one rectangular and three trapezoidal cross sections. The trapezoidal sections had side slopes of 0:1, 0.5:1, 1:1 and 2:1 (x:y refers to horizontal:vertical). Flow conditions for 15 Reynolds numbers in the range of 10^5 and 10^6 were studied for each of the four cross sections. The length dimension used in the Reynolds number was four times the hydraulic radius. The first four moments and the probability distribution of boundary shear stress were calculated for eight locations around one-half the wetted perimeter.

Streamwise boundary shear stress distributions were studied in nonuniform flow conditions created by a 2.5-inch sharp crested weir placed in the 1:1 trapezoidal cross section. Measured mean boundary shear stress values for nine flow conditions were compared with analytical values computed from backwater calculations.

Characteristics of the turbulent velocity fluctuations were investigated for nine flow conditions. Statistical analysis on the longitudinal and vertical components of velocity fluctuation was performed at eight relative depth locations. A mathematical model to predict the velocity fluctuation characteristics as a function of relative depth was developed and calibrated with the experimental data.

Relationships between turbulent velocity fluctuations and turbulent boundary shear stress fluctuations were examined for nine flow conditions. Correlation coefficients were evaluated between the boundary shear stress fluctuations, and the velocity fluctuations occurring at a given distance from the wall. Relative depths of 0.1 to 0.8 provided correlation

coefficient estimates for eight distances from the wall boundary. To examine potential relationships in the region very near the wall boundary, additional data were taken at relative depths ranging from 0.01 to 0.09. The influence of secondary current circulation on the spatial distribution of mean boundary shear stress was qualitatively evaluated by considering velocity isovels. Point mean velocity measurements over one-half the channel were taken for two flow conditions. For each flow condition the matrix of mean velocity data points were used to determine the mean velocity isovel patterns.

1.4 Brief Summary and Conclusions

Cross-streamwise distribution of boundary shear stress was not predictable using mean flow parameters; however, the maximum boundary shear stress was predictable. For 60 flow conditions, the average value of the ratio of measured maximum shear stress on the side to the theoretical shear stress was 0.67. The theoretical shear stress is defined as $\gamma y S_f$ where γ is the fluid specific weight, y is the depth of flow and S_f is the energy slope. The average value of the ratio of the measured maximum shear stress on the bottom to $\gamma y S_f$ was 0.97. The values of the two ratios ranged from 0.44 to 1.28. Therefore, in the design of stable channels where the maximum tractive force is the controlling factor, the use of $\gamma y S$ is adequate for predicting the most probable maximum value of boundary shear stress. The maximum relative shear stress (where the relative shear stress is the shear stress at a given point divided by the mean shear stress for the cross section) occurred off the channel centerline 70 percent of the time. The value of relative shear stress on the channel bottom was generally greater than 1.0 and on the channel side it was less than 1.0. For increasing

aspect ratio (where aspect ratio is the ratio of channel width to flow depth) and increasing channel side slope the range of relative shear stress decreased, implying the shear stress became more uniform. The absolute shear stress generally decreased near the corners and water surface, but did not go to zero.

The root-mean-square (RMS) of the shear stress fluctuations was relatively constant regardless of location; however, the RMS value on the bottom was generally higher than the RMS on the side of the channel. For higher aspect ratio and higher channel side slope the RMS became relatively constant around the channel perimeter. The RMS increased with increasing Reynolds number.

The probability density function (PDF) of the fluctuating component of shear stress was positively skewed. The skewness and kurtosis parameters indicated a similarity to the theoretical lognormal distribution. The chi-square and Smirnov-Kolmogorov statistics for goodness of fit indicated that the experimental distributions more closely followed a lognormal distribution. The goodness of fit improved with increasing Reynolds number.

Streamwise variation of mean boundary shear stress in nonuniform flow was predictable using the theoritical tractive force equation. Measured mean boundary shear stress in gradually varied nonuniform flow behind a weir conpared favorably to calculated values. Using standard backwater computations the variation of depth and energy slope was evaluated and used to determine the streamwise shear stress distribution. Good agreement between measured data and calculated values occurred, providing the pressure distribution remained hydrostatic. The influence of a hydraulic jump in the flume

modified the pressure distribution and increased the shear stress at the locations nearest the jump.

An analytical model for predicting turbulent velocity fluctuations was calibrated and tested. Model prediction of root-mean-square (RMS) values of turbulent velocity fluctuations compared excellently to measured data. The PDF of the velocity fluctuations near the wall were approximately normally distributed as compared to the approximately lognormally distributed shear stress fluctuations.

Evaluation of the correlation coefficients between fluctuating velocity and fluctuating boundary shear stress indicated a strong relationship near the wall boundary. As the distance from the wall boundary increased the correlation coefficients steadily decreased. Isovels of mean velocity were used to evaluate the secondary current influence on the spatial distribution of mean boundary shear stress. Compression of the isovels generally indicated higher boundary shear stress.

1.5 Objectives Identified in the Proposal and the Degree of Completion by the Project

In the original proposal to the National Science Foundation specific objectives were outlined for the project. To evaluate the success of the project, the degree of completion of each of these objectives must be considered.

The first and second objectives of the proposal related to the investigation of the spatial variation of the probabilistic distribution, and the statistical moments of boundary shear stress as a function of flow condition and channel geometry. To accomplish these objectives four prismatic channel cross sections were considered with 15 different

flow conditions, resulting in 60 experimental runs. For each experimental run eight locations of boundary shear stress were measured and a complete probabilistic analysis performed at each measuring location. Chapter VI summarizes these results. In addition, the variation of the mean boundary shear stress in the nonuniform flow behind a dam was considered. Nine flow conditions were experimentally measured and results compared to analytical computations. Chapter VII presents these results. The degree of completion on these two objectives was 100 percent.

The third objective considered the influence of secondary current on the boundary shear stress characteristics. Two flow conditions and one channel cross section were used in this effort. It was apparent after performing the experimental work that an entirely separate investigation should be conducted to thoroughly document the complex interactions of secondary flow and boundary shear stress. As much time could have been spent on this objective as was spent on the rest of the project all together. The work completed indicated some basic trends and relationships (Chapter IX), but the influence of geometric shape and a wide range of hydraulic flow conditions remains unknown. The degree of completion on this objective was 50 percent.

The fourth objective evaluated the relationship of the hydraulic and geometric conditions to the probability distribution parameters. The large amount of data resulting from objectives 1 and 2 made this a simple task. Chapter VI details the results. The degree of completion on this objective was 100 percent.

The fifth objective was to "study the interrelationship of the turbulent velocity structure to the shear stress process." A

mathematical model was calibrated and tested that predicts the turbulent intensity of the velocity fluctuations. The model prediction was compared to experimental data with excellent results. Chapter VIII outlines the model formulation, calibration and testing. The correlation of the turbulent velocity fluctuations with the turbulent boundary shear stress fluctuations was thoroughly evaluated. Chapter IX presents the results and describes the decreasing correlation with increasing distance from the wall. The degree of completion on this objective was 100 percent.

The final objective was to relate the results of the investigation to open channel flow problems. An initial step towards this objective was to consider the theoretical background of boundary shear stress relationships, and to review previous investigations of boundary shear stress processes that are available in the literature. Chapters II and III summarize the pertinent information, respectively. As explained previously, the results of this investigation are not directly applicable to alluvial channel hydraulics problems; however, the investigation has verified some of the relationships used in stable channel design. The most significant contribution to river mechanics due to this investigation result from the basic research that was involved. A framework has been developed to continue specific investigations contributing to a long-term research effort of alluvial river systems. The complexity of alluvial river mechanics requires this step-by-step approach, especially when the influences of turbulence are considered. The answers to difficult questions relating to sediment transport processes will not be apparent from any one investigation; only from the combined experience of many research efforts will the answers become known. The contributions of this investigation to the scientific community have been made

available in papers presented at two international conferences and in an additional six papers presented to the American Society of Civil Engineers (ASCE) for possible publication. These publications are:

1. "Modeling of Turbulent Intensity in Open Channel Flows," paper presented at the International Conference on Numerical Methods in Laminar and Turbulent Flow, held at the University College of Swansea, Wales, on July 18-21, 1978.
2. "Prediction of Turbulent Intensity in Open Channel Flows," paper presented to the XVIIIth International Congress of the International Association for Hydraulic Research, Italy, 1979.
3. "Tractive Force Variation in a Backwater Area," technical note submitted to ASCE, Journal of the Hydraulics Division, for possible publication, May, 1979.
4. "Tractive Force Variation in Open Channel Flow," paper submitted to ASCE, Journal of the Hydraulics Division, for possible publication, September, 1979.
5. "Turbulence Prediction in Open Channel Flow," paper submitted to ASCE, Journal of the Hydraulics Division, for possible publication, May, 1979.
6. "Hot-Film Calibration with Nonlinear Response," paper submitted to ASCE, Journal of the Engineering Mechanics Division, for possible publication, May, 1979.
7. "Calibration Facility for Flush Mount Hot-Films," technical note submitted for possible publication to ASCE, Journal of the Engineering Mechanics Division, April, 1979.

8. "Turbulent Velocity and Boundary Shear Stress Relationships," technical note presented to ASCE, Journal of the Hydraulics Division for possible publication, September, 1979.

The degree of completion of this objective was 100 percent.

The overall success of the project was excellent. Completion of project objectives was extremely good. Additionally, several extra benefits are available as a result of the research. Specifically, a new calibration facility was designed and tested for hot-film boundary shear stress probes, and a complete computer package for real-time data acquisition and analysis was developed. Both of these factors will make further research increasingly more efficient and effective.

II. THEORETICAL REVIEW

2.1 General

A brief review of boundary layer concepts relating to shear stress at the wall and smooth boundary velocity relations are given to provide a framework for further discussion. Understanding the general characteristics of boundary shear stress and the nature of the velocity gradient near the wall is necessary before discussing spatial and temporal distributions of boundary shear stress in fully developed turbulent open channel flow. In addition, the derivation of the tractive force equation and the governing equations for nonuniform flow are presented.

2.2 Boundary Layer Concepts

The theoretical pattern of fluid motion follows the geometric shape of the channel boundary when viscosity is neglected. The effects of viscosity alter the velocity distribution by creating a no-slip condition at the boundary where the flow velocity is zero. Therefore, the velocity gradient has a maximum value at the wall and decreases into the fluid. The steepness of the velocity gradient very near the wall implies that the only significant viscous shear occurs within a relatively thin layer near the wall. According to Prandtl's theory this narrow zone is called a boundary layer. Outside this thin layer of fluid the effects of viscous action are small and the flow pattern is determined by the geometric conditions as well as the inertia, pressure gradient, and body forces.

The boundary layer thickness, δ, is defined as the point separating the boundary layer from the zone of negligible viscous influence. Since this distance is difficult to establish, δ is generally defined as the

distance where the velocity is within one percent of its asymptotic or free stream value. The relative magnitude of δ varies inversely with the root of the Reynolds number. It has been shown analytically and experimentally for laminar flow that the velocity distribution is roughly parabolic and that (3)

$$\frac{\delta}{x} = \frac{5}{R_x^{1/2}} \tag{2-1}$$

where x is the distance downstream from the beginning of the boundary layer and R_x is the Reynolds number based on x.

For the velocity distribution to remain parabolic as the boundary layer thickness increases, the velocity gradient must decrease in magnitude. The velocity gradient at the wall is the local shear stress, or

$$\tau_o(x) = \mu\left(\frac{dU}{dy}\right)\Big|_{y = 0} \tag{2-2}$$

where $\tau_o(x)$ is the wall shear stress at location x, U is the velocity, y is the distance from the wall and μ is the dynamic viscosity. If we assume that the velocity gradient very near the wall is linear, then

$$\tau_o(x) = \mu\left(C\,\frac{U_o}{\delta}\right) \tag{2-3}$$

where C is a constant and U_o is the free stream velocity. Solving Equation (2-1) for δ and substituting into Equation (2-3) gives

$$\tau_o(x) = \frac{\mu C U_o \sqrt{U_o x/\nu}}{5x} \quad . \tag{2-4}$$

Rearranging to more convenient terms,

$$\tau_o(x) = \frac{2C}{5\sqrt{U_o x/\nu}} \frac{\rho U_o^2}{2} \tag{2-5}$$

where ν is the kinematic viscosity and ρ is the fluid density. Therefore, the intensity of shear at the boundary decreases with x as the boundary layer develops. Defining the local drag coefficient as

$$c_f = \frac{2C}{5\sqrt{U_o x/\nu}} \tag{2-6}$$

and substituting the drag coefficient into Equation (2-5) gives

$$\tau_o(x) = c_f \frac{\rho U_o^2}{2} \quad . \tag{2-7}$$

The coefficient $2/5\ C$ has been shown both analytically and experimentally to be 0.664 in laminar flow. Therefore, the laminar flow local drag coefficient is

$$c_f = \frac{0.664}{R_x^{1/2}} \quad . \tag{2-8}$$

Integrating Equation (2-7) gives the total drag exerted by the fluid on either side of a plate of width B and length L. The resulting equation is

$$F = c_f BL \frac{\rho U_o^2}{2} \tag{2-9}$$

where c_f is a mean drag coefficient.

As the Reynolds number increases, a transition from a laminar to a turbulent boundary layer occurs. When the retarded flow of the boundary

layer becomes unstable, more fluid mixing occurs as turbulence reaches further out into the main stream. The velocity distribution becomes more uniform throughout a greater part of the layer, while producing a very large velocity gradient near the wall. For turbulent boundary layers it can be shown that

$$c_f = \frac{0.059}{R_x^{1/5}} \tag{2-10}$$

where R_x is less than 10^7.

2.3 Smooth Boundary Velocity Relations

Turbulent boundary layers are composed of zones of different types of flow due to viscosity effects. Therefore, no single relationship can be developed to predict the mean velocity magnitude throughout the boundary layer. Three basic zones and two velocity relations have been developed to describe the continuous mean velocity profile. The law of the wall applies to the zone close to the wall and the velocity defect law applies to the outer regions of flow.

In the laminar sublayer, molecular viscosity has a dominant effect on the velocity profile and turbulence. The velocity gradient is nearly linear and the shear stress away from the wall is assumed constant and equal to the shear at the wall,

$$\tau \simeq \tau_o = \mu \left.\frac{dU}{dy}\right|_{y=0} = \mu \frac{U}{y} \quad . \tag{2-11}$$

For smooth boundaries the law of the wall describing the velocity profile is then

$$\frac{U}{u_*} = f\left(\frac{u_* y}{\nu}\right) \tag{2-12}$$

where u_* is the shear velocity equal to $\sqrt{\frac{\tau_o}{\rho}}$. Defining the laminar (or viscous) sublayer, δ', as the thickness of y at $\frac{u_* y}{\nu} = 4$, then

$$\delta' = \frac{4\nu}{u_*} = \frac{4\nu}{U\sqrt{c_f/2}} \quad . \tag{2-13}$$

Since $\tau_o = c_f \rho \frac{U^2}{2}$ (Equation 2-7) the viscous sublayer thickness decreases as the shear stress increases.

For the outer regions of flow, a logarithmic velocity relation can be derived from Prandtl-von Karman boundary layer theory. For smooth boundaries in the transitional zone, or buffer zone, the equation takes the form

$$\frac{\overline{U}}{u_*} = \frac{2.3}{\kappa} \log\left(\frac{u_* y}{\nu}\right) + \text{Constant} \tag{2-14}$$

where κ is the von Karman constant and $\overline{U}$ is the mean velocity. For the logarithmic zone, the Reynolds stresses dominate the molecular viscous stresses to produce the velocity profile. A velocity-defect law of the form

$$\frac{U - \overline{U}}{u_*} = g\left(\frac{y}{\delta}\right) \tag{2-15}$$

is observed to be characteristic of the region. A logarithmic relation for the function g is obtained by assuming Equation (2-14) will give $\overline{U} = U$ at $y = \delta$. Then, by subtracting

$$\frac{U - \overline{U}}{u_*} = -\frac{2.3}{\kappa} \log\left(\frac{y}{\delta}\right) + \text{Constant} \tag{2-16}$$

where a different constant results. A velocity-defect relation can be developed to describe the buffer zone defined by Equation (2-14). Therefore, two equations in the form of the law of the wall and the velocity-defect law can be defined with the proper constants to describe

the entire velocity profile over a smooth boundary. These equations seem to be universal in that they apply over a wide range of Reynolds numbers (4).

2.4 Tractive Force Equation

The theoretical equation relating the tractive force, or boundary shear stress, to the flow depth and a characteristic slope can be derived by a force balance approach (5). Consider the channel section shown in Figure 2-1 with the small element of dimensions y, Δx and Δb. Due to the net hydrostatic thrust on the element there is a small horizontal force acting that is taken as positive in the downstream direction. Assuming the slopes are small and the pressure distribution hydrostatic, the pressure difference along any horizontal line drawn longitudinally through the element has a magnitude of $\gamma\Delta h$ where Δh is the difference in water surface elevation from the upstream to the downstream face of the element. If $\Delta h/y$ and $\Delta z/y$ are small, the total hydrostatic thrust is $-\gamma y\Delta b\Delta h$. The summation of this force over the whole section is $-\gamma A\Delta h$ where A is the cross-sectional area. This force is the effective component of the gravity force acting on the fluid element.

The gravity component is resisted by a shear force equal to $\tau_o P\Delta x$ where P is the wetted perimeter and τ_o is the mean longitudinal shear stress acting over this perimeter. The two forces resulting from gravity and shear stress can be considered parallel with the assumption of small bed slope. Therefore, the net force in the direction of flow is

$$(-\gamma A\Delta h - \tau_o P\Delta x) \ . \qquad (2\text{-}17)$$

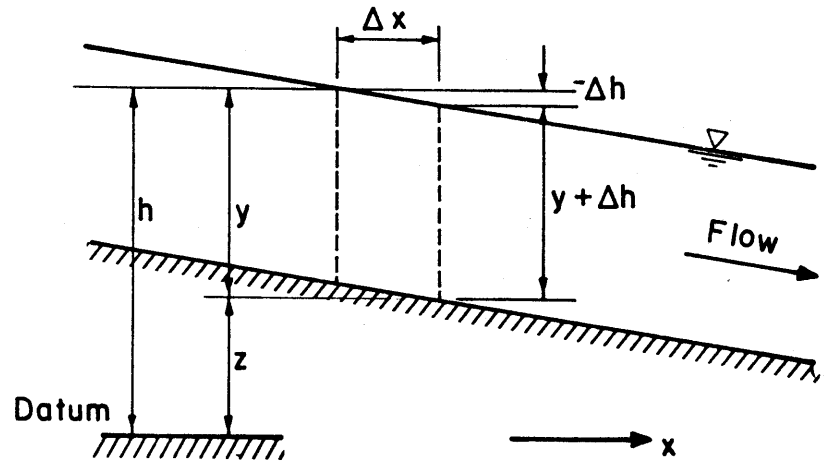

Longitudinal Section

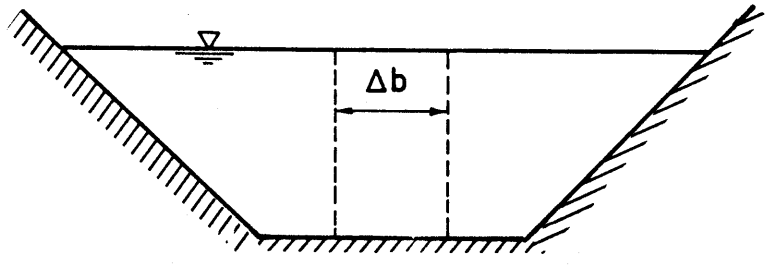

Cross Section

Figure 2-1. Definition sketch of channel section for development of tractive force equation.

For uniform flow the channel slope, cross section, flow depth and mean velocity remain constant. There is no acceleration and the net force on the element is zero. Solving Equation (2-17) for τ_o the tractive force equation is

$$\tau_o = \gamma R S_o \tag{2-18}$$

where $R = A/P$ is the hydraulic radius and S_o is the bed slope, $-dz/dx$, which equals the water surface slope $-dh/dx$ for uniform flow.

For the case of nonuniform flow the velocity is not constant and the net force is no longer zero due to acceleration or deceleration. Considering steady flow, the only acceleration is convective and equal to $U\frac{dU}{dx}$. The net force given by Equation (2-17) applies to a mass $\rho A \Delta x$ and the equation of motion becomes

$$-\gamma A \Delta h - \tau_o P \Delta x = \rho A \Delta x \left(U\frac{dU}{dx}\right)$$

Solving for τ_o the tractive force equation is

$$\begin{aligned} \tau_o &= -\gamma R \left(\frac{dh}{dx} + \frac{U}{g}\frac{dU}{dx}\right) \\ &= -\gamma R \frac{d}{dx}\left(h + \frac{U^2}{2g}\right) \\ &= \gamma R S_f \end{aligned} \tag{2-19}$$

where H is the total energy $\left(h + \frac{U^2}{2g}\right)$ and $S_f = -dH/dx$ is defined as the total energy slope.

In general the tractive force equation can be written as

$$\tau_o = \gamma R S \tag{2-20}$$

provided the slope S is properly defined. For uniform flow the bed slope, water surface slope and total energy slope are all equal so Equation (2-18) is a special case of (2-19) when $S_o = S_f$.

2.5 Governing Equations for Nonuniform Flow Computations

Determining the gradual variation of depth that takes place in a channel when the flow is nonuniform is based on the integration of the equation of motion (5). Newton's second law, $F = ma$, defines the force required to accelerate the mass m, at a rate a, as being the product ma. In applying this equation to fluid flow, consideration must be given to a continuous mass of moving fluid rather than a discrete single body.

Considering force as the net impressed force, Newton's second law can be stated as

$$\Sigma F = ma \tag{2-21}$$

where ΣF is the difference between the total impressed force and any force such as friction or viscous drag that resists the motion of the body. Applying Equation (2-21) to a single fluid element (Figure 2-2) having unit thickness at right angles to the plane of the paper, only two kinds of impressed forces can exist. Using s to indicate any chosen direction, the force due to a pressure gradient would be expressed as

$$-(\partial p/\partial s)\ \Delta s \Delta n \tag{2-22}$$

and the force due to the weight of the element would be expressed as

$$(\gamma \Delta s \Delta n)\ \sin\theta \tag{2-23}$$

where Δn is the width of the element, Δs is the length (in the chosen direction) of the element, p is the pressure, γ is the specific weight of fluid, and θ is the orientation with respect to the horizontal direction. Equation (2-23) can also be expressed as

$$-(\gamma \Delta s \Delta n)\ \partial z/\partial s \tag{2-24}$$

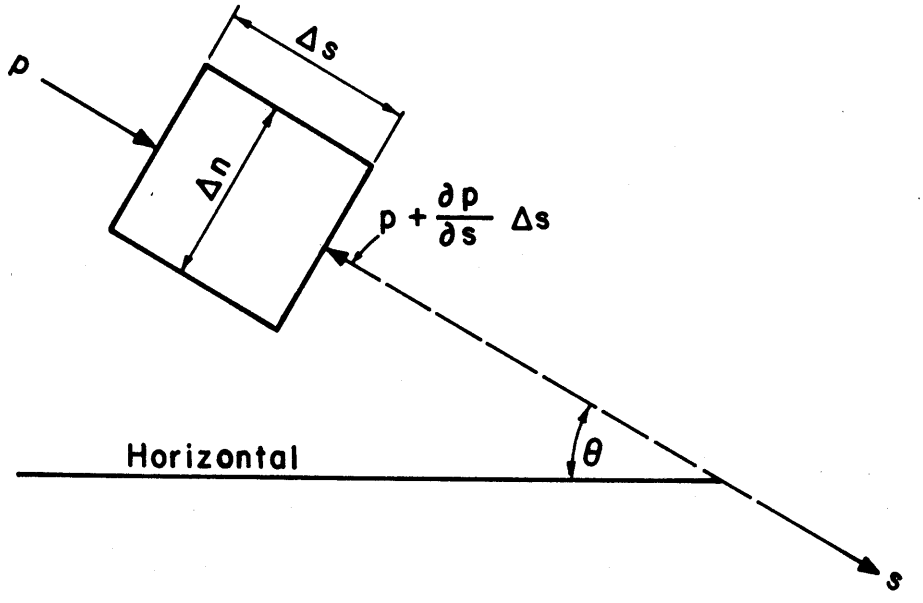

Figure 2-2. Definition sketch for development of nonuniform flow equations.

where z is the vertical height above a datum. If ρ is the mass density of the fluid then

$$ma = (\rho \Delta s \Delta n)\, a_s \tag{2-25}$$

where a_s is the fluid acceleration in the s direction. Substituting Equations (2-22), (2-24) and (2-25) into Equation (2-21) gives

$$\frac{\partial}{\partial s}(p + \gamma z) + \rho a_s = 0 \tag{2-26}$$

which is the Euler equation.

In a moving fluid velocity can vary with time and position. When the flow is irrotational the acceleration term a_s can be defined as

$$a_s = \frac{dU}{dt} = U\frac{\partial U}{\partial s} + \frac{\partial U_s}{\partial t} \tag{2-27}$$

where the two terms are named convective and local acceleration, respectively. Considering steady flow where the local acceleration is zero, Equation (2-26) becomes

$$\frac{\partial}{\partial s}(p + \gamma z) + \rho U\frac{\partial U}{\partial s} = 0 \tag{2-28}$$

which can be integrated directly to

$$p + \gamma z + \frac{1}{2}\rho U^2 = \text{Constant, H (total energy)} \tag{2-29}$$

which is the Bernoulli equation along the streamline. For steady irrotational flow the equation of motion normal to the streamline is of exactly the same form as the equation of motion along a streamline (Equation (2-26)). Integration again leads to the Bernoulli equation, therefore, the Bernoulli expression is the same throughout the entire fluid, not only along individual streamlines but also across streamlines (6). Since the Bernoulli equation was obtained by integrating a

force equation with respect to distance, it is an energy equation.

To determine the longitudinal depth variation in a nonuniform flow condition, the derivative with respect to x (streamwise direction) of the Bernoulli equation gives

$$\frac{dH}{dx} = \frac{d}{dx}\left(z + y + \frac{U^2}{2g}\right) = -S_f \tag{2-30}$$

where S_f is the slope of the energy line. Rewriting Equation (2-30)

$$\frac{d}{dx}\left(y + \frac{U^2}{2g}\right) = -\frac{dz}{dx} - S_f \tag{2-31}$$

or

$$\frac{dE}{dx} = S_o - S_f \tag{2-32}$$

where S_o is the bed slope and E is the specific energy $\left(y + \frac{U^2}{2g}\right)$. Equation (2-32) is the form of the equation of motion commonly integrated to evaluate water surface profiles in nonuniform flow conditions.

III. LITERATURE REVIEW

3.1 General

Literature on boundary shear stress can be categorized into the topics of instantaneous characteristics, spatial characteristics, analytical prediction and experimental measurement. To determine the extent of research in each of these topics a computer literature search was utilized. Data bases searched were Compendex and NTIS through Lockhead Information Systems. Considering the importance of boundary shear stress processes in open channel flows, there has been a relatively small amount of literature published.

3.2 Instantaneous Characteristics of the Hydrodynamic Forces

In open channel flow, instantaneous hydrodynamic forces at the wall are known to have turbulent characteristics. The instantaneous nature of lift and drag forces on discrete roughness elements in turbulent open channel flow was clearly demonstrated by Einstein and El-Samni (7), and by Cheng and Clyde (8). For hydraulically smooth boundaries, Blinco and Simons (9) measured the instantaneous boundary shear stress directly. These investigations indicated that a complete description of hydrodynamic forces must be done statistically.

Einstein and El-Samni measured lift and drag forces on 0.225 feet semi-spherical balls. The drag force, or shear stress, was determined indirectly by measuring vertical velocity distributions. The shear stress was determined from the Prandtl-von Karman velocity relation (Equation 2-14) by extrapolating the velocity gradient to the wall. Only the mean shear stress can be determined by this method. Lift force was measured as a pressure difference between the top and bottom of the spheres. The measurement technique allowed identification of turbulent

fluctuations of lift. The lift force was divided into the average value and a random fluctuation superimposed over the average. Statistical analysis showed that the frequency of lift forces at the wall followed the normal error law.

In a later investigation Cheng and Clyde measured fluctuations of lift and drag forces on an individual spherical roughness element 1.0 feet in diameter. Direct measurements were made by a delicate system of semiconductor strain gages. Results indicated that lift and drag forces were independent of each other and that the probability distributions of the fluctuations followed the normal distribution. The mean lift and drag forces were measured in terms of lift and drag coefficients of the form given in Equation (2-9).

In a hydraulically smooth boundary, Blinco and Simons measured the instantaneous boundary shear stress with flush surface hot-film anemometry. The statistical nature of the instantaneous boundary shear stress was fully investigated and documented for measuring locations on the centerline of a 20 cm wide rectangular plexiglas flume. The results indicated that turbulent intensity (coefficient of variation) of boundary shear stress decreased with increasing Reynolds number. Skewness and kurtosis parameters (third and fourth moments) were Reynolds number dependent, both slightly decreasing as Reynolds number increased. The general trend of the higher moments indicated that the distribution became less skewed and more gaussian as the Reynolds number increased. The probability density estimates were positively skewed to the right and the modes were to the left of the expected values. The probability density functions were best fit by gamma and lognormal theoretical distributions.

3.3 Analytical Prediction of Boundary Shear Stress Distribution

Several analytical models have been postulated for predicting the spatial variation of the mean value of boundary shear stress in prismatic channels. Most of the models are derived by assuming the boundary shear stress is expressible in terms of a postulated velocity distribution in the channel cross section or by using laminar flow analogies. In general, these models are in poor agreement with field observations due to the effects of inconsistent velocity distribution throughout the cross section, influence of channel bank resistance and the effects of secondary current circulation. Additionally, the inherent complexity of the instantaneous boundary shear stress at a point creates conditions where present analytical models can only approximately define the magnitude and spatial distribution of boundary shear stress. A summary of current analytical models includes techniques using the Prandtl-von Karman logarithmic velocity relation, a power law velocity relation, finite difference solutions and membrane analogies. Many of these are analyzed in publications by Lane (1) and Leliavsky (10).

In a 1935 publication, O'Brien and Rindlaub (11) suggested using the Prandtl-von Karman theory of flow near a flat surface to predict shear stress. Measuring velocity profiles at points perpendicular to the perimeter of the profile, the shear stress can be computed from

$$\tau_o = \rho \frac{c(v_1 - v_2)}{\log_e \frac{z_1}{z_2}} \qquad (3\text{-}1)$$

where v_1 and v_2 are velocities at distances z_1 and z_2 from the boundary and c is a constant. This equation can be derived from Equation (2-14).

The Bureau of Reclamation published a report in 1952 outlining two analytical and one semi-analytical method for predicting boundary shear stress distribution (12). Mathematical solutions based on a velocity distribution expressed as a power function were used for rectangular channels with a width-depth ratio of two. Application of mathematical solutions for trapezoidal channels was not feasible; however, a semi-analytical method using a membrane analogy was successful. Solutions were also made by finite difference techniques. Results indicated that for trapezoidal channels of width-depth ratio less than 8, the maximum shear on the bottom was close to the theoretical shear, $\gamma y S_o$, and on the sides the maximum was 0.76 $\gamma y S_o$. For all channel shapes, the shear stress at the corners and at the surface was zero.

Replogle and Chow (13) developed a semi-analytical approach that reduced prediction of tractive force distribution to a solution laminar-flow-type equation. The solution was the sum of assumed laminar velocity distributions for natural channels and laminar shear distributions. Solutions were obtained by finite-difference methods using a computer. Constants were evaluated experimentally in a circular conduit flowing part full by a comparison of measured tractive force distributions with computer generated distributions. Results showed the maximum tractive force occurred off center at a displacement approximately ten percent of the wetted perimeter. Distributions were independent of Reynolds and Froude numbers in the turbulent flow range, but were a function of the depth-to-top-width ratio (d/T). For shallow channels ($d/T < 0.3$) the effects of free surface and secondary currents were negligible and the turbulent flow tractive force distribution was similar to laminar

flow. The values of tractive force near the surface decreased, but did not go to zero.

3.4 Boundary Shear Stress Distribution from Experimental Data

Several investigators have reported measuring the shear stress distribution around the channel perimeter for both laboratory flumes and natural streambeds. The techniques used included indirect measurement by application of Prandtl-von Karman turbulent flow theory (Equation 3-1) and direct measurement using Preston tubes and hot-film anemometry.

Boundary shear stress measurements for a straight reach approaching a bend in a trapezoidal channel are reported by Ippen and Drinker (14). Local shear stresses were measured by Preston-type devices for width-depth ratios of 7 to 12. Results indicated that the boundary shear stress patterns could not be predicted quantitatively from the mean hydraulic flow characteristics. Four flow conditions gave values of relative shear stress ($\tau/\overline{\tau}$) near the centerline ranging from 0.85 to 1.6, with a wide degree of scatter within each flow condition. The general trend showed relative shear values of 1.1 near the centerline, increasing to approximately 1.2 toward each side before slightly decreasing near the corners.

Shear stress distribution relationships to Froude number were given by Davidian and Cahal (15). Two width-depth ratios (2.25 and 3.60) were studied using Preston tube measurements in a smooth rectangular flume. As the Froude number increased over a range of 0.1 to 1.5, the ratio of maximum wall shear to average wall shear decreased from 1.3 to approximately 1.0, the ratio of average bed shear to average total cross-sectional shear decreased from 1.2 to approximately 1.0, and the ratio of average wall shear to average bed shear increased from 0.7 to

approximately unity. Shear distributions became more uniform with increasing Froude number, implying that a shift in aspect ratio (width-depth ratio) towards two-dimensional flow produces more uniform shear at the boundary.

Preston tube measurements in smooth rectangular channels with aspect ratios of 0.83 to 20.28 are reported by Rajaratnam and Muralidhur (16). For the centerline shear stress to equal the theoretical $\gamma y S_o$, the aspect ratio had to be greater than 15. Relative shear values ranged from 0.3 to 1.15 for Froude numbers of 1.1 to 2.4. The ratio of maximum side shear stress to maximum bed shear stress varied with aspect ratio and Reynolds number. Similar to the results of Davidian and Cahal, the bed shear stress was observed to be more uniform as aspect ratio increased.

Tractive force variation in smooth rectangular channels, based on analytical laminar flow calculations and experimental measurements, were presented by Kartha and Leutheusser (17). Preston tube measurements of boundary shear stress for aspect ratios of 1 to 12.5 were studied. Results indicate that maximum relative shear stress values of 1.3 along the channel side occur at an aspect ratio of 1, and maximum relative shear stress values of 1.6 along the channel bottom occur for an aspect ratio of 3. Maximum shear stress on the channel bottom always occurred on the centerline for analytical computations using laminar flow theory, while for turbulent flows of small aspect ratio, the experimentally measured maximum was off center. For laminar flow calculations and turbulent flow measurements, the shear stress appeared to approach zero near the corners of the cross section. Near the water

surface only the measured turbulent shear stress approached zero; in laminar flow calculations the maximum shear stress occurred at the surface.

Distribution of boundary shear stress in cobble bed rivers was reported in 1977 by Bathurst (18). Boundary shear stress was indirectly determined using vertical velocity profile measurements. In straight channel reaches the cross-stream distribution of shear stress was characterized by peaks and troughs with no distinct maximum. It is theorized that this resulted from multicell stress-induced secondary current systems that created regions of upwelling and downwelling flow. Uniformity of shear stress distribution was observed to increase as Reynolds number increased, due to decreased influence of secondary circulation relative to the mean flow. It is suggested that factors influencing the shear stress distribution are purely Reynolds number dependent and that other influences, such as cross-sectional shape, are negligible when large width-depth ratios exist.

Stochastic properties of the spatial variation of boundary shear stress were first presented by Wylie et al. (19). Boundary shear stress distributions for a smooth rectangular channel were measured using hot-film anemometry. Measurements were taken over half the wetted perimeter for a single aspect ratio of 4.4. Statistical moments and probability density functions were computed through digital time series analysis for each measuring location. The coefficient of variation followed trends similar to relative shear stress trends reported by Kartha and Leutheusser (17). Skewness and kurtosis coefficients exhibited quasi-periodic variations along the bed and sidewall with similarities in the fluctuations. Probability density function estimates were positively

skewed and fit by the theoretical two-parameter gamma distribution only near the corners. In the remainder of the channel, neither gamma nor lognormal distributions fit the measured data.

IV. EXPERIMENTAL FACILITIES

4.1 Flume

Investigation of the boundary shear stress relationship to channel shape required design and construction of a variable geometry flume. Critical factors in design included the ease in changing the side slope, rigidity of the flume and minimization of water leakage. In order to meet project requirements, several alternative structures were considered.

The first alternative involved using a wedge between the bottom of the flume and the sidewalls to maintain a trapezoidal cross section. A different wedge would have been necessary for each channel side slope, requiring that the wedge could be easily removed and replaced. Excessive support devices for the channel sidewalls would have been necessary because the wedge junction would not have been rigid. Leakage was also a potential problem. This design did not meet any of the design requirements satisfactorily.

The second alternative involved constructing a permanent trapezoidal cross section based on the largest anticipated side slope (2:1). Styrofoam or similar filler material could then be used to create trapezoidal channels of steeper side slopes. A permanent structure could have been readily made watertight and rigid, however, modifying the channel geometry would have been difficult. This alternative was considered better than the first alternative, but not flexible enough to meet project requirements.

The design used involved a long continuous hinge, referred to as a piano hinge, to join the bottom and sidewalls. The piano hinge provided support without excessive bracing and was extremely flexible. Channel

geometry could be changed in less than one hour by adjusting the side supports.

From the rectangular headbox water entered the flume through a transitional section as shown in Figure 4-1. Water exited the flume in a free-fall to the tailbox. To reduce agitation of the water, a spillway was later added to dampen the free-fall.

The flume was constructed entirely of plexiglas to insure uniformity and to allow easy visualization of flow patterns. Plexiglas also avoids problems of oxidation and provides hydraulically smooth boundary conditions. Plexiglas thickness of 3/4 inch was used throughout, except at the bottom of the channel where 1-inch thick plexiglas was used. Plate 4-1 shows the completed flume and support system. The channel supports were bolted to an aluminum I-beam 48.9 cm wide and 50.8 cm tall. The I-beam supported the entire flume, including the headbox and tailbox. Bed slope was adjusted by a screw jack attached to the I-beam at the upstream end over a range of 0.000 to 0.030 with a setting accuracy of $\pm$ 0.0005. Plate 4-2 shows an end view of the flume with the tailbox, I-beam and channel support system.

Initially, leakage was a problem between the piano hinge and plexiglas. Silicon sealant was used to stop the leakage; however, uniform application was difficult, resulting in questionable flow patterns. After several attempts to apply the silicon adequately, the channel was disassembled and a narrow strip of nylon reinforced vinyl was laid over the hinge. After reassembly, the vinyl served the same purpose as the silicon by sealing the hinge and eliminating leakage, while maintaining a sharp corner. The completed flume satisfied all of the requirements

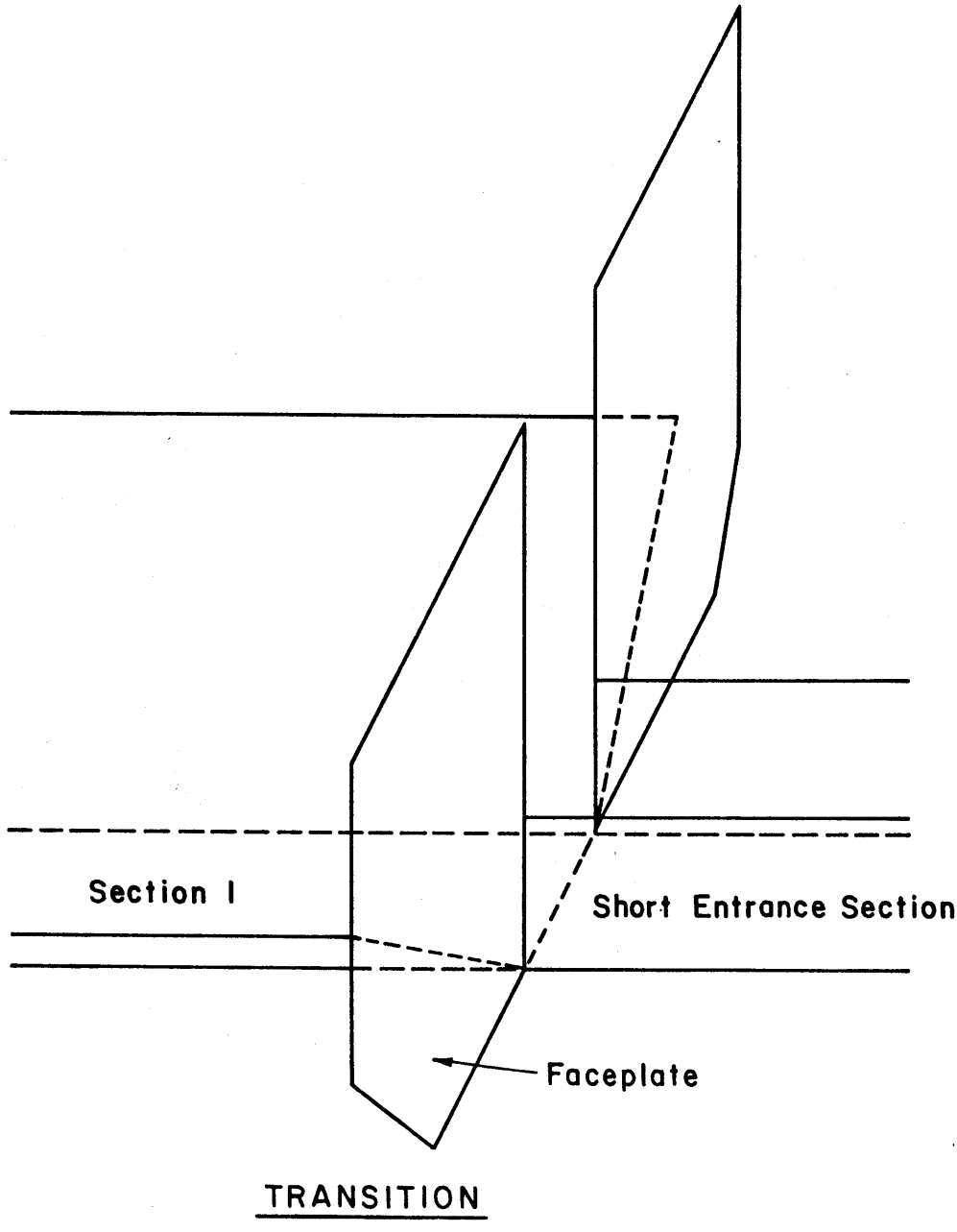

Figure 4-1. Three-dimensional view of transition region.

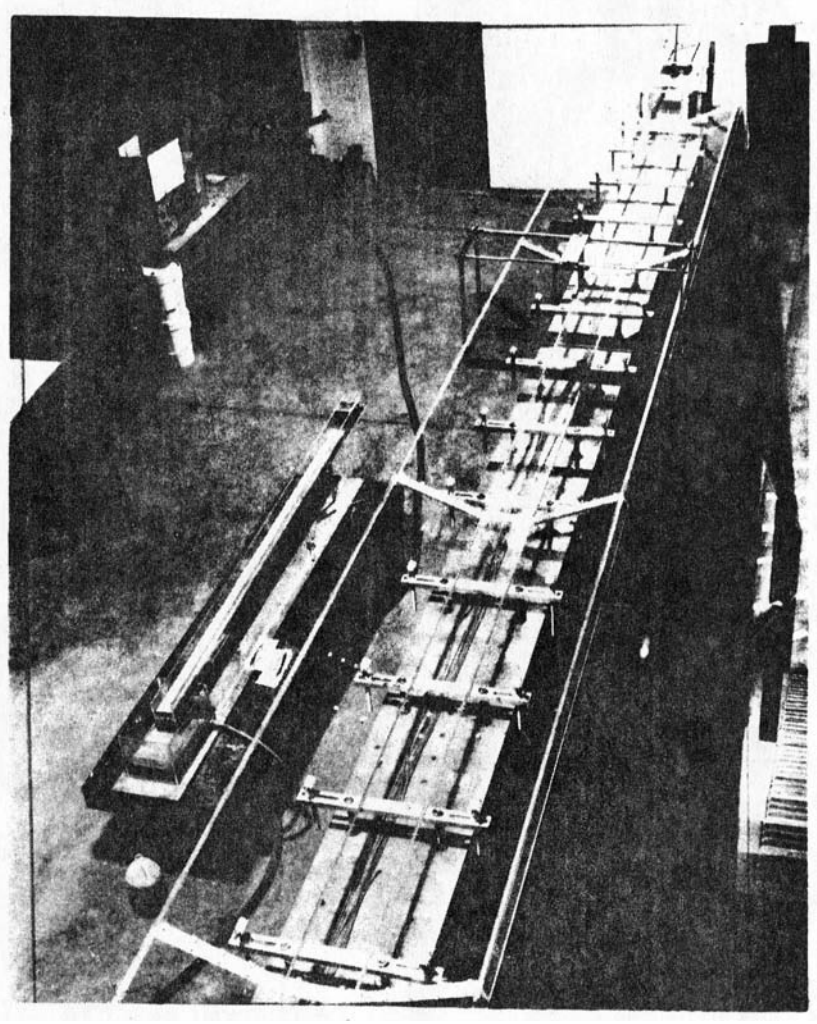

Plate 4-1. Top view of trapezoidal channel showing support system.

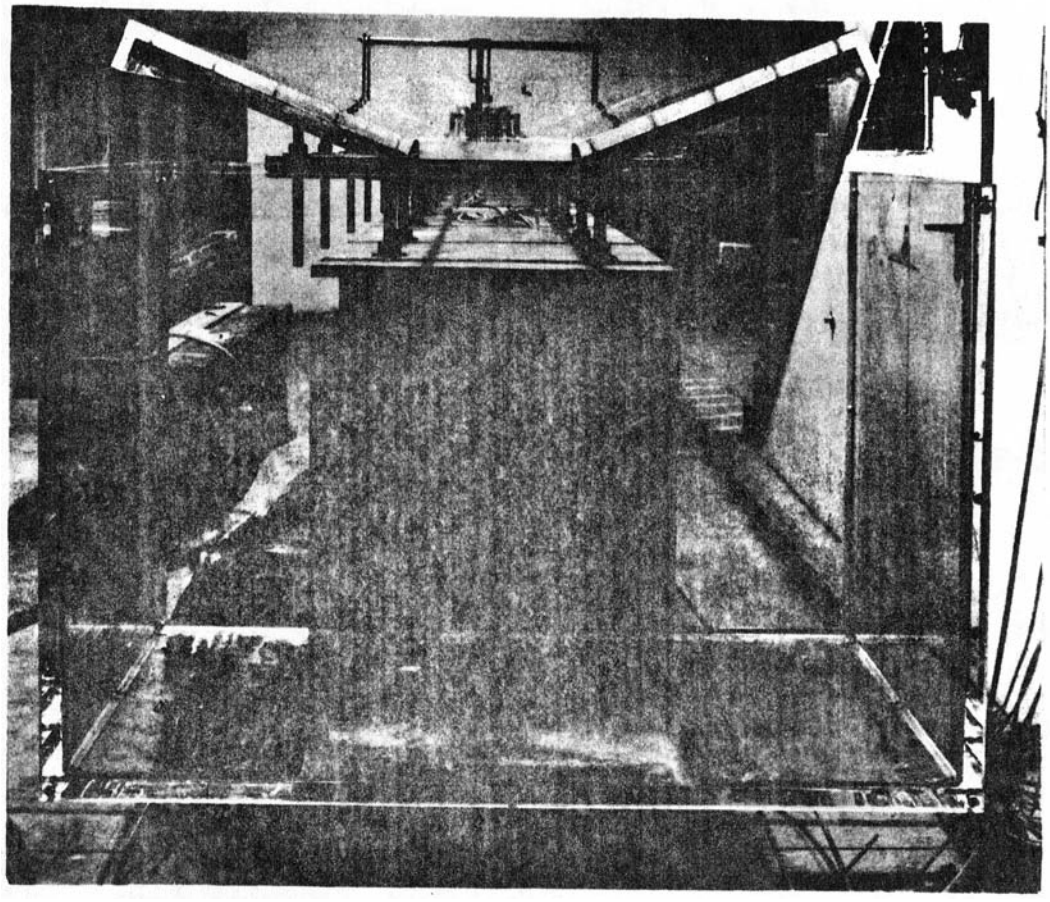

Plate 4-2. End view of trapezoidal channel and tailbox.

of a variable geometry flume by providing ease and flexibility in channel modification, a strong rigid support system and minimum leakage.

The flume discharge was supplied by a brass axial flow pump connected to a 3-speed electric motor. Water was recirculated from the tailbox to the headbox by a 4-inch plexiglas pipe mounted beneath the I-beam. The recirculating system insured consistency in water quality. Discharge was determined by a sharp-edged orifice mounted in the return pipe. Pressure loss across the orifice was measured by single-leg manometers. The orifice calibration was verified volumetrically before the project started.

4.2 Boundary Shear Stress Calibration Facility

The nature of this investigation required both measurement of very small shear stresses and detection of very small differences in shear stress. Over the entire range of flow conditions investigated, the mean shear stress was always less than 35 dynes/cm^2. Accuracy to one dyne/cm^2 required a very accurate calibration flow field where the boundary shear stress was precisely known and repeatable to a high degree of accuracy. The two calibration flow fields considered were fully developed turbulent pipe flow and fully developed laminar flow between two parallel plates. Appendix A outlines fully developed turbulent pipe flow calibration and the reasons for not utilizing it in this project. The following paragraphs describe the laminar flow calibration facility.

Similar to fully developed pipe flows, the wall shear stress for two-dimensional flow between two parallel plates is a linear function of the pressure gradient. This can be shown by considering fully developed laminar flow between two parallel walls as illustrated in Figure 4-2.

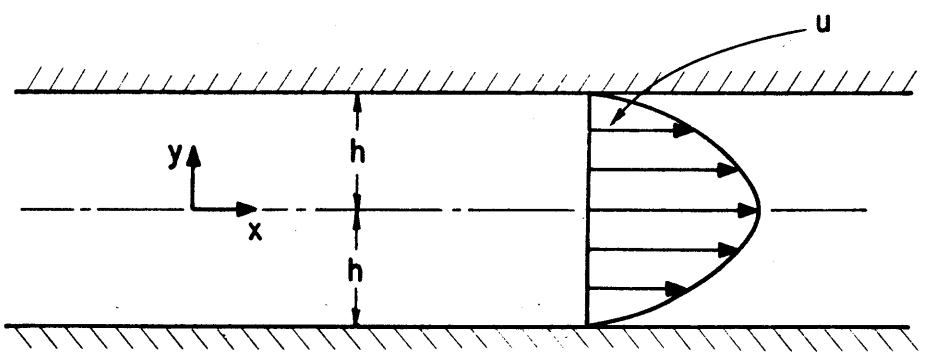

Figure 4-2. Definition sketch for laminar flow between two parallel plates.

The velocity is at maximum at the center and zero at the walls. In the x-direction, the equation of motion can be written as

$$0 = -\frac{dp}{dx} + \mu\left(\frac{d^2U}{dy^2}\right) \tag{4-1}$$

where p is pressure, x is longitudinal distance, μ is the absolute viscosity of the fluid, U is the velocity and y is vertical distance. Integrating once gives

$$\mu\left(\frac{dU}{dy}\right) = \left(\frac{dp}{dx}\right)y + C \tag{4-2}$$

where C is a constant. Assuming the velocity distribution is parabolic then

$$\frac{dU}{dy} = 0 \text{ at } y = 0 \tag{4-3}$$

and therefore C must be zero. Since dp/dx is a constant for fully developed flow and shear stress is

$$\tau = \mu \frac{dU}{dy}\,, \tag{4-4}$$

then

$$\tau = \left(\frac{dp}{dx}\right)y\,. \tag{4-5}$$

A flow facility generating essentially two-dimensional flow between two parallel plates would satisfy the assumptions of this derivation and provide a suitable calibration environment. Such a calibration stand was designed and built and is shown in Figure 4-3. It consisted of two plexiglas sheets spaced 0.25 inches apart. To satisfy the two-dimensional flow assumption, the width of the facility was set at 28.5 inches giving a width-depth ratio (w/d) of 114. Width-depth ratios greater

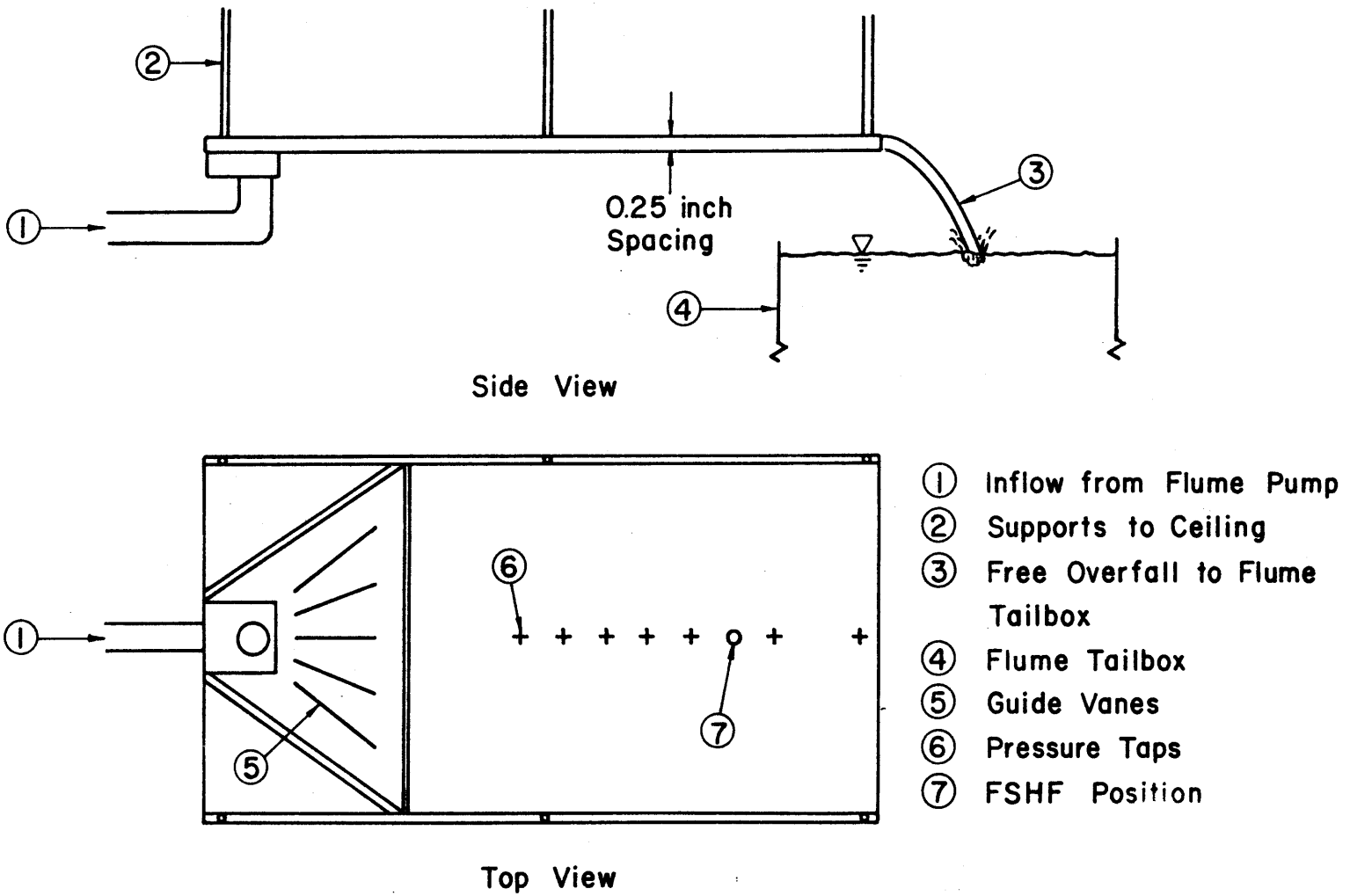

Figure 4-3. Laminar flow calibrating facility for boundary shear stress probes.

than 100 are commonly assumed to minimize influence of the sides, providing essentially two-dimensional flow. To insure fully developed flow, the length of the facility was set at 48.0 inches giving a length-depth ratio (L/d) of 192. Measurement of the pressure gradient later verified that the flow was fully developed in the calibration region (Figure 4-4). The calibration facility was suspended above the flume and the water discharged in a free-fall to the tailbox. Observation of the nappe under all calibration flow conditions resulted in the conclusion that the calibration stand did generate laminar flow. In the 2-foot fall to the tailbox the nappe remained laminar, never making the transition to turbulent flow.

Water was supplied to the calibration stand from the tailbox so that calibrations were always in the same environment as experiments. The plates were maintained at a uniform spacing by a truss system built from aluminum angle. Excellent repeatability was obtained since the probe was easily mounted flush to the surface and the laminar flow field made readings stable and consistent. Pressure gradient measurements were made with a Pace model DP-7 pressure transducer. The calibration procedures for this transducer are explained in Appendix B.

4.3 Velocity Calibration Stand

The velocity calibration facility had to be capable of calibrating both one- and two-dimensional hot-film velocity probes. One-dimensional probes are calibrated only with respect to the magnitude of velocity. Two-dimensional split-film probes require calibration with respect to magnitude and incident angle of velocity. Common methods used to calibrate velocity devices include pitot tubes and towing tanks, however, pitot tubes are insensitive to small changes of incident angle and the towing

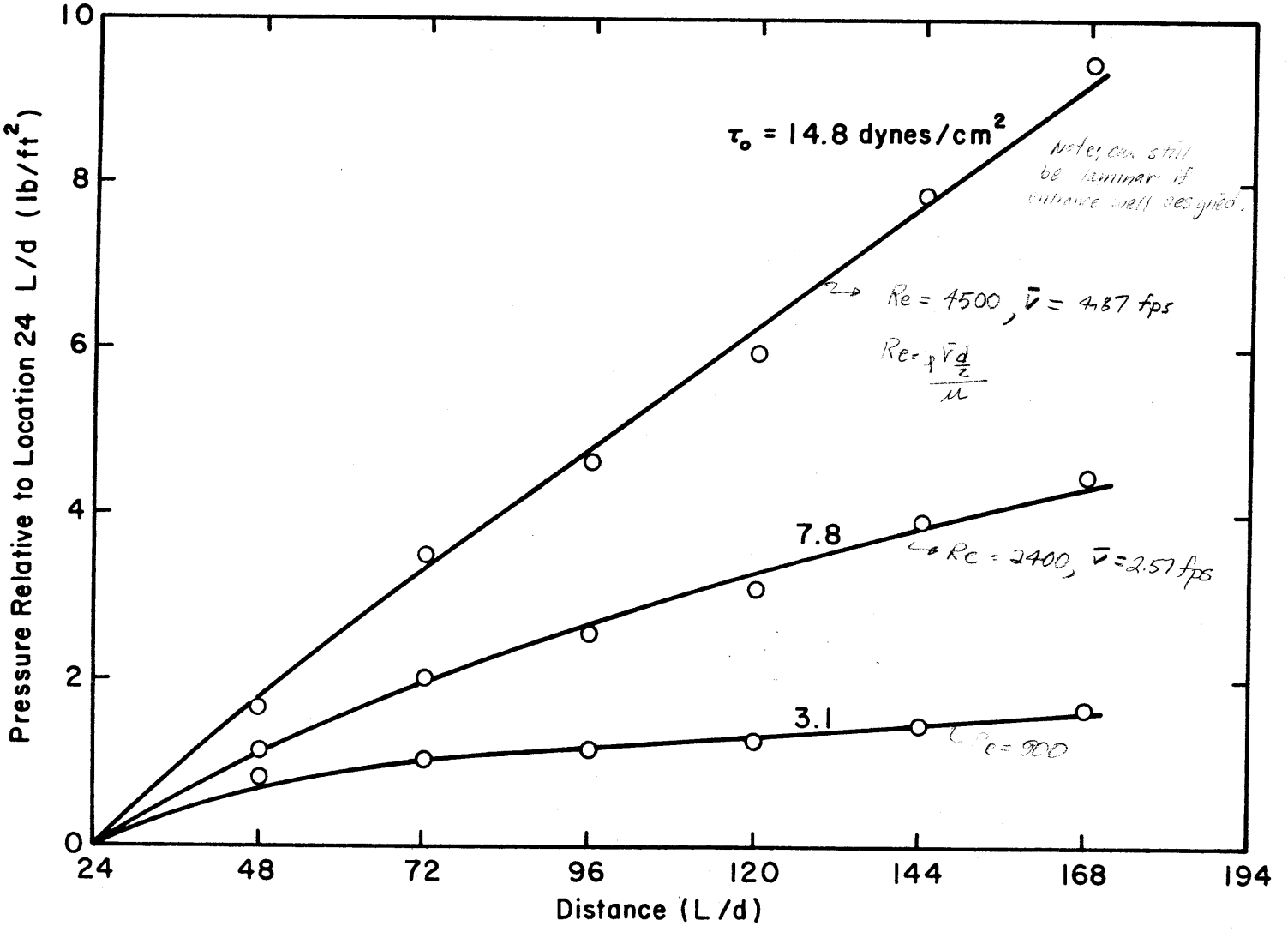

Figure 4-4. Graph of pressure versus distance for laminar calibration facility.

method was not adaptable to the variable geometry flume. A special calibrating device that was sensitive to magnitude and incident angle had to be built to calibrate the hot-film velocity probes used in this project.

The velocity calibration system consisted of a constant head tank that supplied a steady discharge to a cylindrical chamber with a 0.99 cm internally rounded orifice. The jet from the orifice discharged into a second cylindrical tank that maintained a constant head by a free overflow. Water for the calibration system was pumped out of the tailbox and returned to the tailbox insuring the water quality in calibration was the same as used in data collection. Discharge through the orifice was controlled by a gate valve and measured by a Fisher and Porter Mass flow meter. Figure 4-5 illustrates the velocity calibration system.

The centerline velocity of the jet from the orifice was computed from the continuity equation. Use of the continuity equation assumes that the velocity profile across the orifice is uniform. To determine the characteristics of the orifice, a one-dimensional cylindrical hot-film velocity probe (TSI Model 1219W) was used.

According to turbulent jet theory, the length of the potential core, L_o, is the distance from the orifice in which the centerline velocity remains constant. For an axially symmetric jet the potential core length is $7d_o$ where d_o is the jet diameter (4). However, the velocity profiles begin to flatten and lose similarity to a uniform distribution as the distance from the orifice increases. Therefore, the optimum calibration location is relatively close to the orifice. Figure 4-6 shows the measured centerline jet velocity at several flow

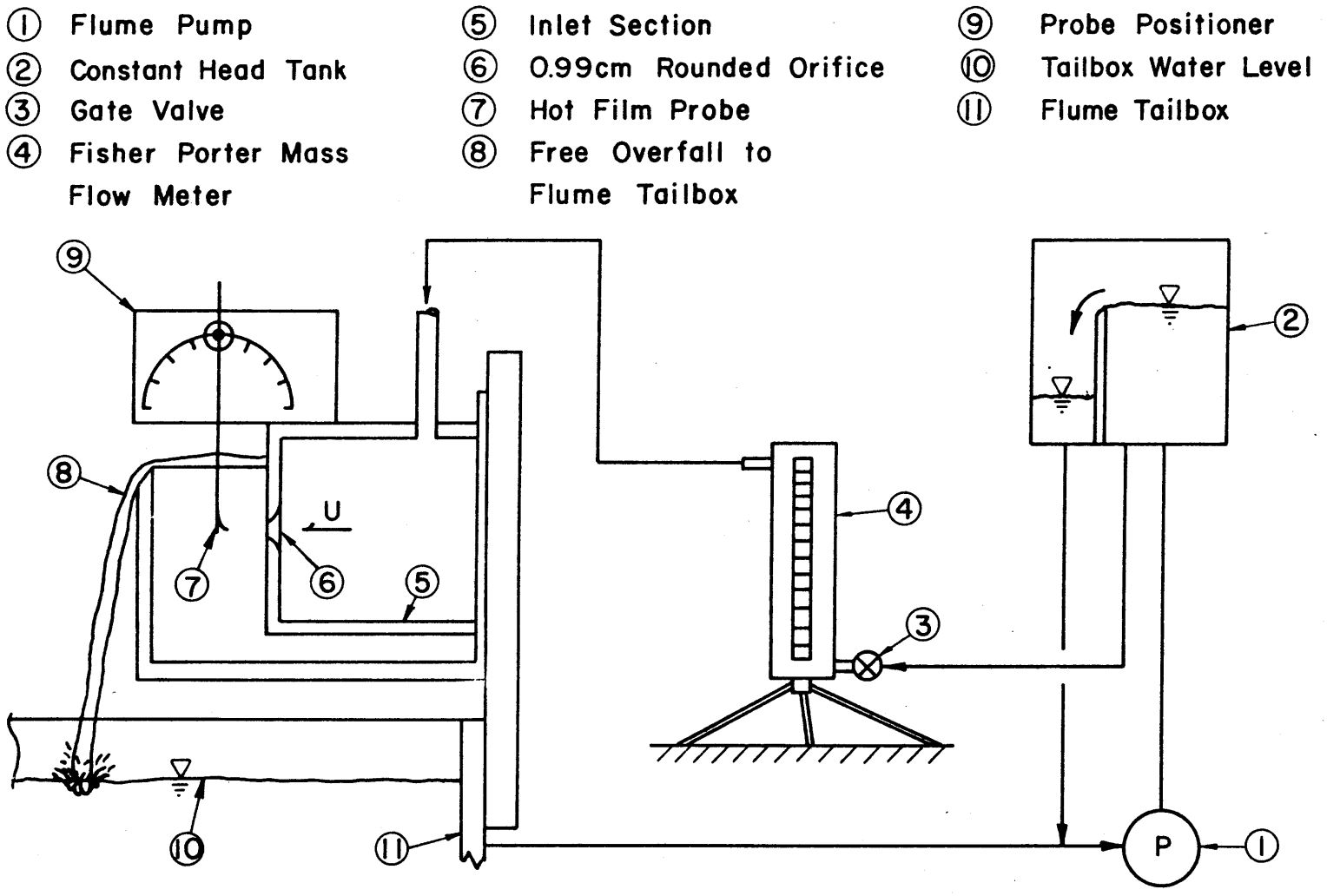

Figure 4-5. Velocity calibration facility.

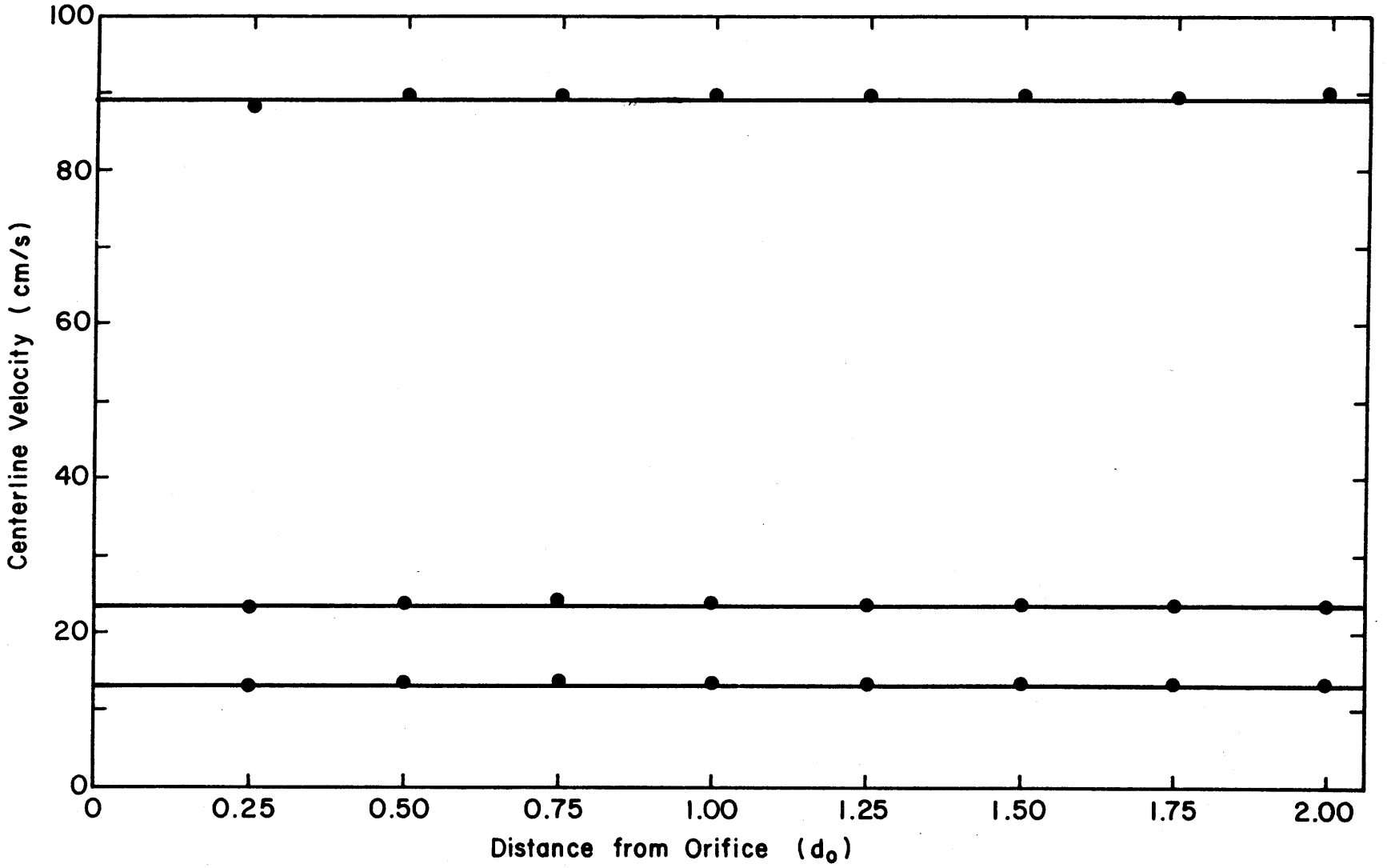

Figure 4-6. Centerline jet velocity for 0.99 cm orifice.

rates for the distances of interest in calibration. The centerline velocity is quite stable up to a distance $2d_o$.

Velocity profiles were then taken at a distance 1.5 d_o from the orifice to determine distribution characteristics. For the flow rates of interest in calibration, the velocity distribution was flat across the middle and approximately uniform in shape. Figure 4-7 shows the velocity profiles at four discharge rates.

To calibrate split-film velocity probes a device to control the incident angle of velocity on the probe is required. Rotating the probe in the centerline of the jet simulates this effect. Figure 4-5 illustrated the split-film velocity probe supported in front of the orifice by the device for controlling the angle of incidence.

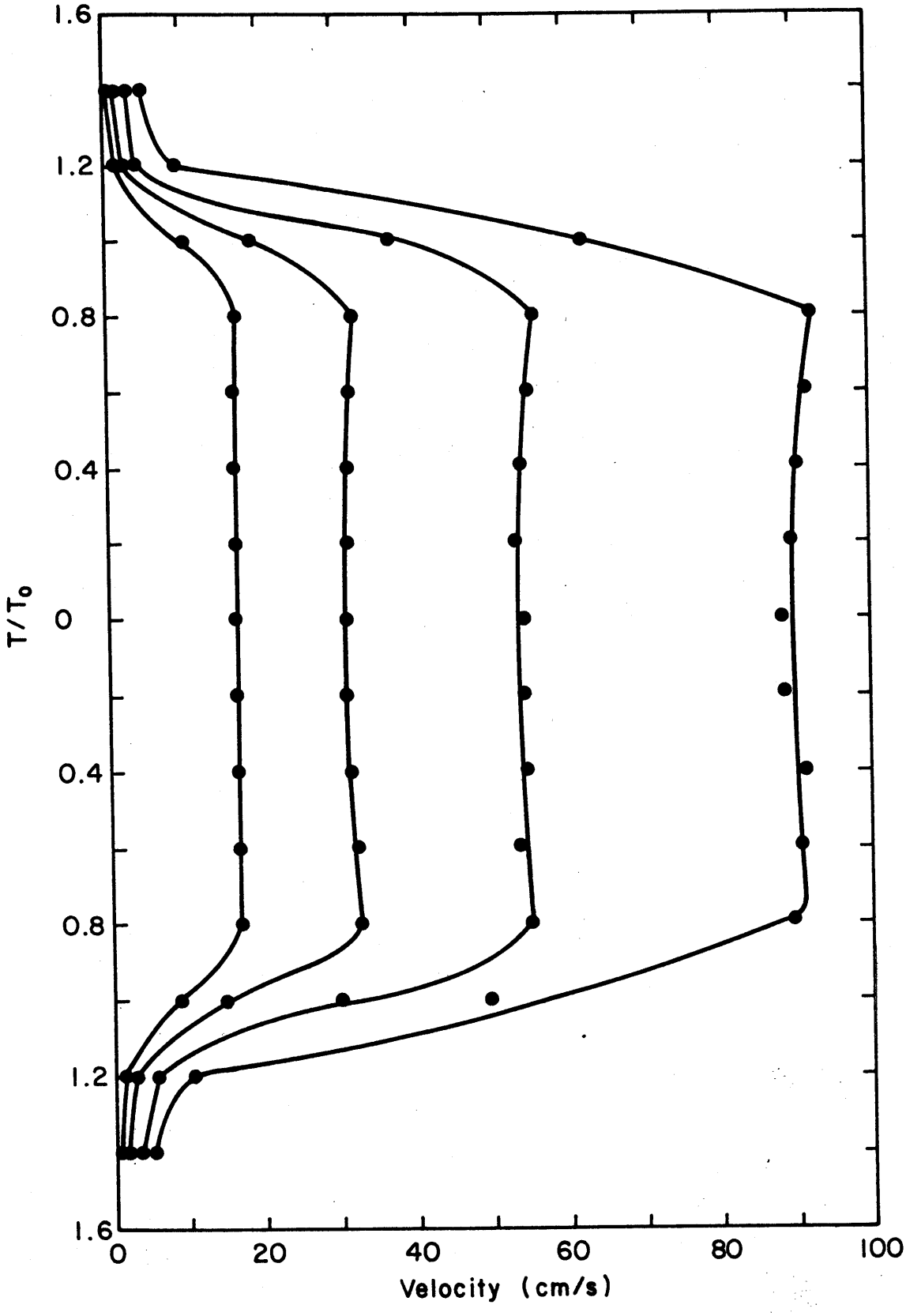

Figure 4-7. Velocity profiles for 0.99 cm orifice.

V. DATA COLLECTION, PROCESSING AND ANALYSIS

5.1 Water Quality Considerations

Water quality is critical when using in hot-film anemometry techniques. Control of water quality variables can reduce problems of voltage drift and inconsistent data. The three basic water quality variables of conductivity, temperature and air content account for most operational difficulties encountered with hot films (20). Contaminants and impurities in the water represent additional sources of operational difficulties. To avoid these problems special precautions were taken with the water used in this study.

Conductivity of ordinary tap water in the hydraulics laboratory is approximately 60 micro-mhos/cm. For hot-film measurements it is necessary to minimize the conductivity of the water. Conductivity of 18 megaohms/cm and 2 micro-mhos/cm has been reported as adequate for hot-film measurements (20,21). A Culligen Dou-Bed industrial deionization system was used in this investigation. Tap water conductivity was reduced to 4 micro-mhos/cm after passing through the system, which was found adequate in achieving consistent data. Conductivity was measured with a Beckman conductivity bridge.

Tap water for the flume was also filtered with a Culligen Filtr-Cleer multimedia filter. Minimum particle size removed by this filter was 8 microns, according to the manufacturer. The filter capacity of 9 gpm at 20 to 120 psi was not high enough to allow the system to be mounted in-line with the flume recirculation system. Therefore, all of the water passed through the filter-deionization system as the flume was filled and was then recycled in a parallel circuit with the recirculation pipe as necessary. During long periods without operation the water

in the flume was drained and then refilled. Before filling the flume with the filtered and deionized water the plexiglas surfaces were cleaned with solvent alcohol. This eliminated dust particles and other airborne contaminants that had settled into the flume surfaces. To further control airborne particulates, the flume was isolated from the rest of the hydraulics lab by plastic sheets supported on a timber framework. This was necessary because of the amount of sand and sediment used in neighboring projects.

A change in water temperature can significantly affect the hot-film calibration curve. Under some conditions a change of 5.5°F can result in a 100 percent error in mean velocity readings (20). There are two approaches to controlling this effect. The first involves sophisticated temperature compensating circuitry to automatically correct for temperature changes. The second involves maintaining a constant overheat resistance difference, rather than a constant overheat resistance ratio, by continuously monitoring the water temperature and manually correcting the resistance difference for any changes. Temperature compensating circuitry for the number of probes used in this study was prohibitive in cost. The second approach was adopted and water temperature was continuously monitored by a Yellow Springs Model 42-SF Tele-Thermometer that detected changes of temperature to 0.5°C. If the water temperature changed more than 1.0°C the experiment was stopped and calibrations were checked. During the course of experimental work it was discovered that the flume water temperature was very stable and no problems ever developed.

Air bubbles on hot-film probes can decrease the amount of heat transfer resulting in erroneous readings. Bubbles are caused by

hydrogenation or result by deposition from super-aerated water. To minimize this problem low overheat ratios for the hot-film probes were used and water was allowed to deaerate for 72 hours or more after filling. The amount of agitation of water during the experiments was also minimized. If an air bubble appeared on a probe it was removed with a small camel's hair brush.

Taking the precautions discussed above to control water quality minimized the amount of operational difficulties with the hot films. The extra time and effort required was considered beneficial to obtaining quality data.

5.2 Instrumentation

A Thermo-Systems, Inc. (TSI) Model 1053B constant temperature anemometer system was used to measure the instantaneous boundary shear stresses and velocities. The anemometer was a four channel system allowing simultaneous measurement at up to four locations. Signals were monitored on a Tektronic dual trace oscilloscope. Plate 5-1 shows the anemometer, oscilloscope and other related equipment. Two data processing schemes were employed requiring use of different pieces of electronic equipment; however, in both cases the Hewlett-Packard 1000 series minicomputer (Appendix C) was used for data reduction and analysis. The two schemes differed in their method of conveying the voltage signal from the anemometer to the minicomputer.

Initially, the voltage signals were recorded on a 7-track Sandborn FM tape recorder. The input voltage limitation to this recorder was $\pm$ 1.4 volts requiring the anemometer voltage to be suppressed before recording. This was accomplished with a Tektronix Type 127 Preamplifier power supply coupled with a Type 1A7 high gain differential amplifier.

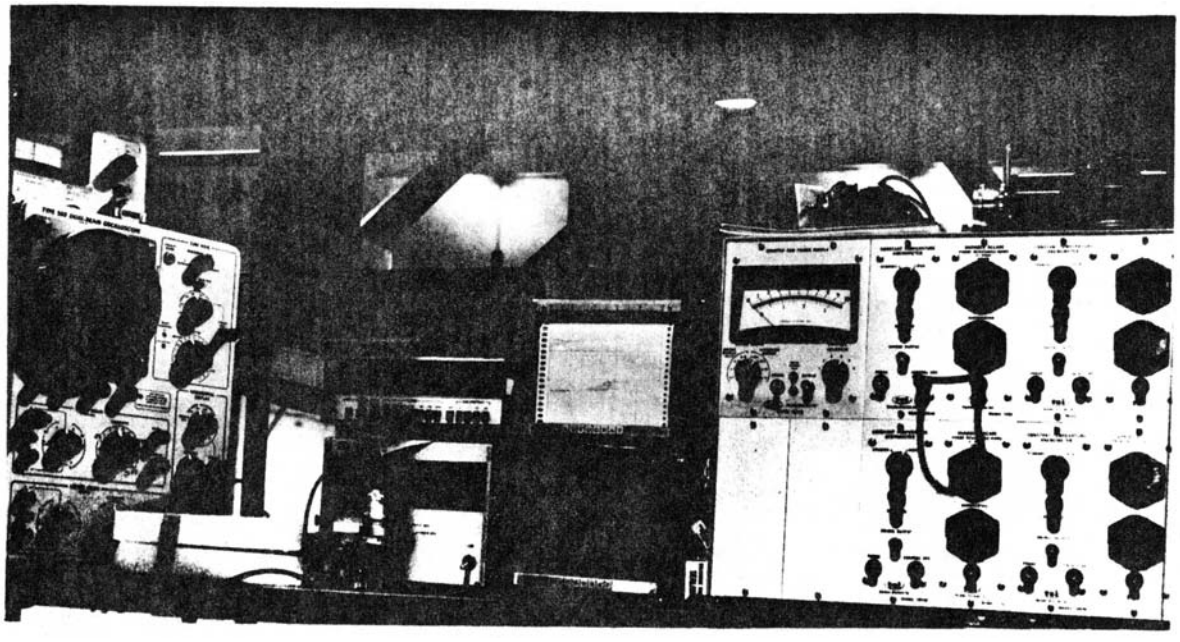

Plate 5-1. Hot-film anemometry system.

Operating as an alternating current (AC) amplifier it suppressed the mean value and amplified only the fluctuating component of voltage. The fluctuating voltage signal was then amplified ten times before being recorded on the tape drive. Using the maximum amplification possible while maintaining the voltage within the input tolerance of the tape drive greatly increased the signal sensitivity and decreased the signal-to-noise (S/N) ratio. To determine the mean value of the voltage signal a TSI Model 1076 true root-mean-square (RMS) voltmeter was used. After recording the voltage signal the tape drive was taken to the HP-1000 minicomputer and replayed into the computer system. Data reduction programs were written to incorporate the amplification and mean values into the voltage time series before data analysis. Figure 5-1 shows a block diagram of the major components required in collecting and analyzing data by this approach.

This system was operational and is a widely used technique for digital data acquisition and analysis, but is a time consuming procedure. Considering the massive amount of data required for this project a more efficient method was implemented.

The HP-1000 minicomputer is capable of interactive input (Appendix C). Using a multi-wire cable from the remote data taking location to the minicomputer allows direct communication with the computer. This eliminates recording the voltage signal on an FM tape recorder and replaying the analog tape into the computer. Considerable time savings can be achieved along with other benefits discussed in Appendix C. Therefore, an 18 conductor cable was installed from the flume location to the minicomputer allowing six data lines and a terminal connection to talk and receive with the minicomputer.

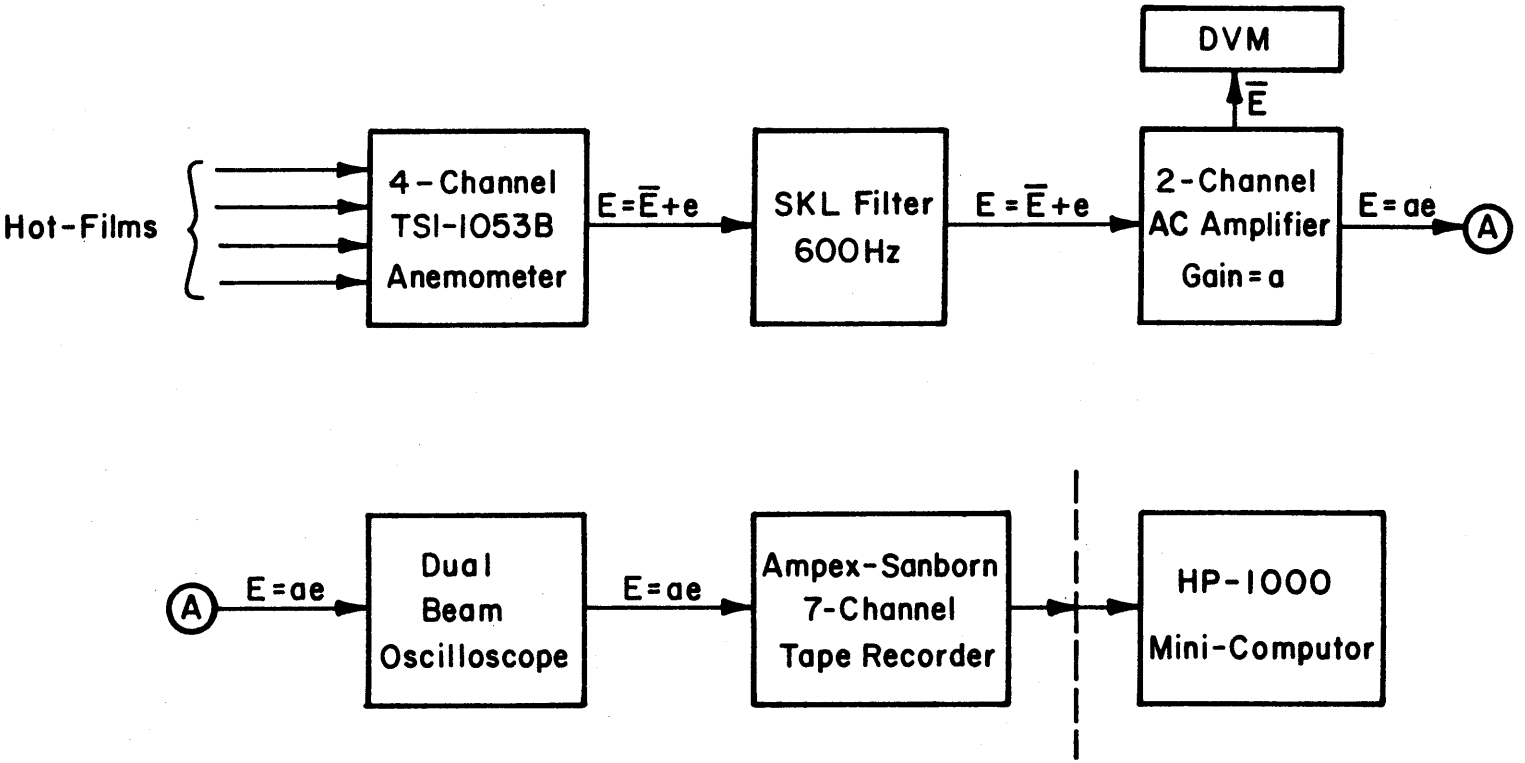

Figure 5-1. Block diagram showing the major electronic components used with 7-channel tape recorder.

To increase sensitivity and accuracy, a suppression and amplification system similar to the data processing technique previously discussed was employed. The input voltage limitation to the minicomputer analog-to-digital converter (A/D) was $\pm$ 15.00 volts. The wider input voltage range of the A/D converter over the FM tape recorder allowed a different system to suppress and amplify the voltage signal that eliminated the need to independently measure the mean value of the signal before amplification. A four channel direct current (DC) suppression circuit was designed and built by the Engineering Research Center Electronics Shop. The suppression circuit was adjusted to suppress the same mean value for each run and the signal was then amplified by a DC amplifier set at a constant amplification of 11 times. A DC amplifier does not automatically suppress the DC value and, therefore, the mean of the voltage signal did not have to be independently measured for each run. With this system of data acquisition and analysis, the signal was transferred directly to the minicomputer, specific data analysis was performed and results were printed on a Texas Instruments Silent 700 computer terminal located at the flume. The system was considerably more efficient because it eliminated the tape drive and the time lag involved between data acquisition and analysis. Figure 5-2 shows a block diagram illustrating the major components required in collecting and analyzing data by this method.

A Spencer-Kennedy Laboratories (SKL) Model 328A variable electronic filter was also used to condition the signal before suppression and amplification. The maximum frequency of interest in hydraulic structures is approximately 250 hz with a mean value around 5 hz (2). Therefore, it was assumed that any signal above 600 hz was the result of electronic noise and should be filtered out.

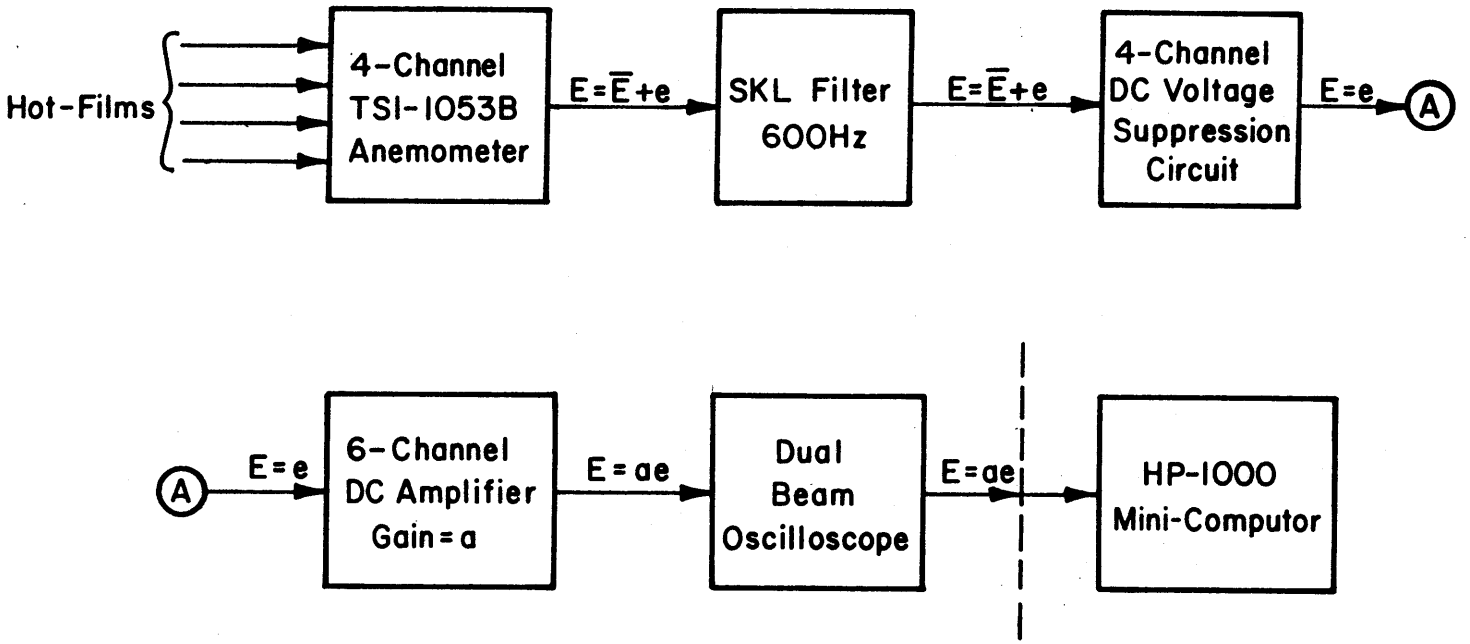

Figure 5-2. Block diagram showing the major electronic components used with the direct connection to the minicomputer.

5.3 Hot-Film Probes and Mounting Procedures

Boundary shear stress was measured with TSI Model 1237W flush surface hot-film (FSHF) probes. The 1237W probe consisted of a 0.25 mm long by 1.0 mm wide platinum film bonded to a quartz body. A round stainless steel casing enclosed the probe body and the exposed platinum film was coated with quartz to insulate it from the water. Figure 5-3 illustrates the design of the probe. The probes were calibrated in the laminar flow facility (Section 4.2) according to the relationships in Appendix D.

Operation of the 1237W probe required mounting it flush with the boundary of the flume. Initially, the probes were inserted through 0.130 inch holes drilled through the plexiglass; however, it was difficult to start the probe into the hole without bumping it. When the probe was bumped a change occurred in the calibration creating serious problems in collecting accurate data. To avoid bumping the probes a special plexiglas mounting device was designed. The probe was first positioned flush in the plexiglas mount and then the mount was positioned in the flume. The two piece assembly could be easily mounted and remounted without disturbing the probe. This significantly increased probe life and the accuracy of the data.

Measuring the shear stress distribution around the channel perimeter through a series of holes drilled across the bottom and up the side of the flume did not give satisfactory results. Unless many holes were drilled in the flume the measuring locations were too far apart. The relative depth locations of the measuring points on the sides also changed from one flow condition to the next, eliminating the basis for comparison. Therefore, traversing slide mounts were designed giving

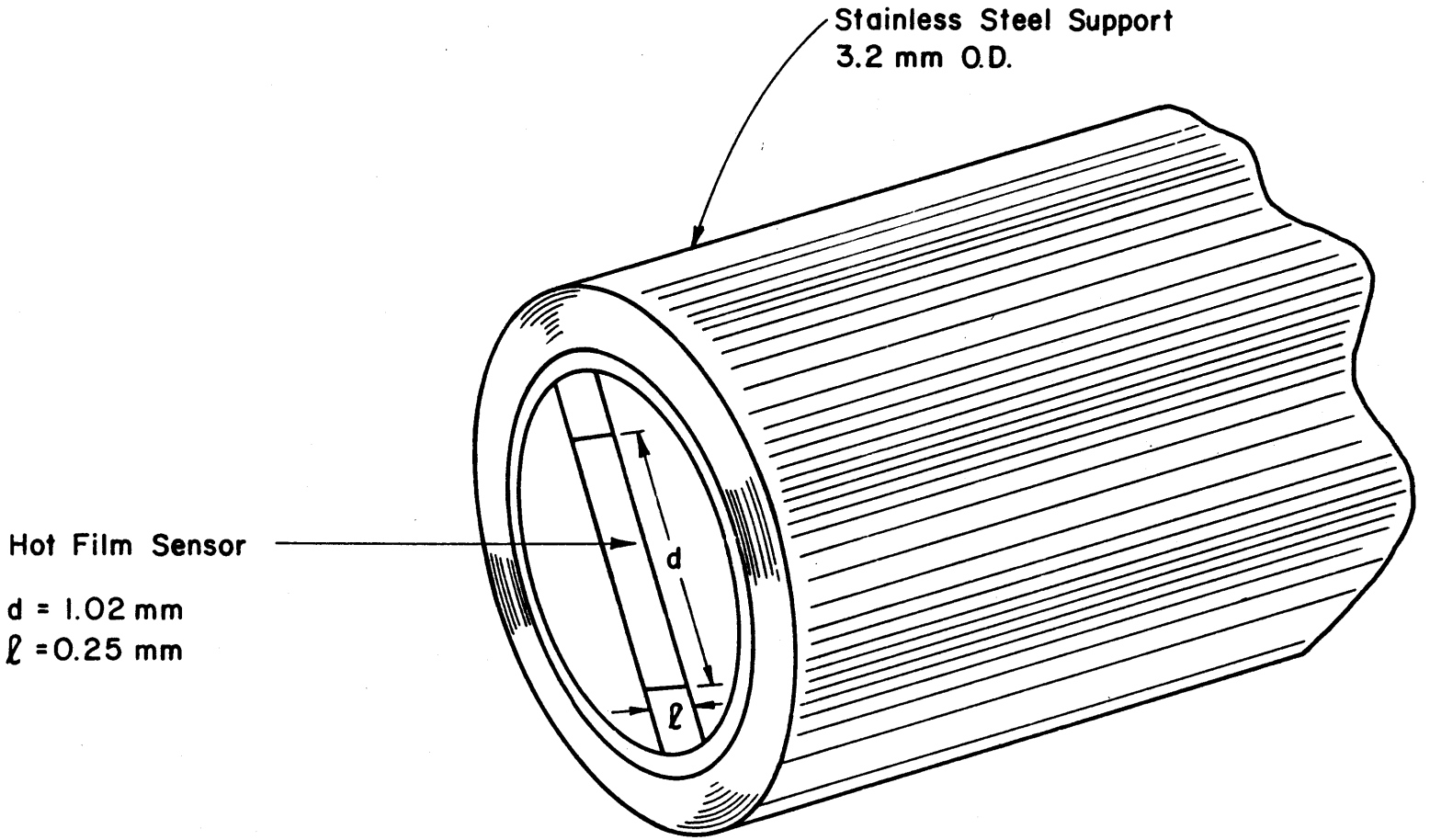

Figure 5-3. Flush surface hot-film sensor.

an infinite range of measuring locations and allowing the same relative depth locations to be measured for all flow conditions. A traverse was also located in the bottom of the flume. The traverses were manually operated by turning a screw and the entire system kept leakproof with rubber seals. The traversing system was a timesaving method of probe positioning and insured quality data.

Detailed measurements of the turbulent velocities near the wall for correlation analysis with simultaneous boundary shear stress measurements were obtained with TSI Model 1218-20W one-dimensional boundary layer probes. The small size of the cylindrical sensor on the 1218-20W probe minimizes the effects of flow interference, and the unique design for boundary layer applications allows measurements very near the wall boundary. This probe was also used to measure velocity profiles for secondary current analysis. The 1218-20W probe was calibrated in the orifice facility described in Section 4.3. Two-dimensional turbulent velocity components were measured with a TSI Model 1287W split-film probe. Due to the small size and unique design of the 1287W probe, it can measure velocity at locations very near the boundary. The split-film sensor consists of a 0.153 mm diameter, 1.01 mm long platinum film fused to a 2.04 mm long quartz rod. The film is split into independent sensors along a plane parallel to the mean flow and perpendicular to the wall. Similar to the 1237W boundary shear stress probes, the 1287W probe is coated with quartz to electrically insulate it from the water. Figure 5-4 illustrates the split-film probe and its use. The split-film probe was calibrated in the orifice facility (Section 4.3) according to the relationships developed in Appendix E.

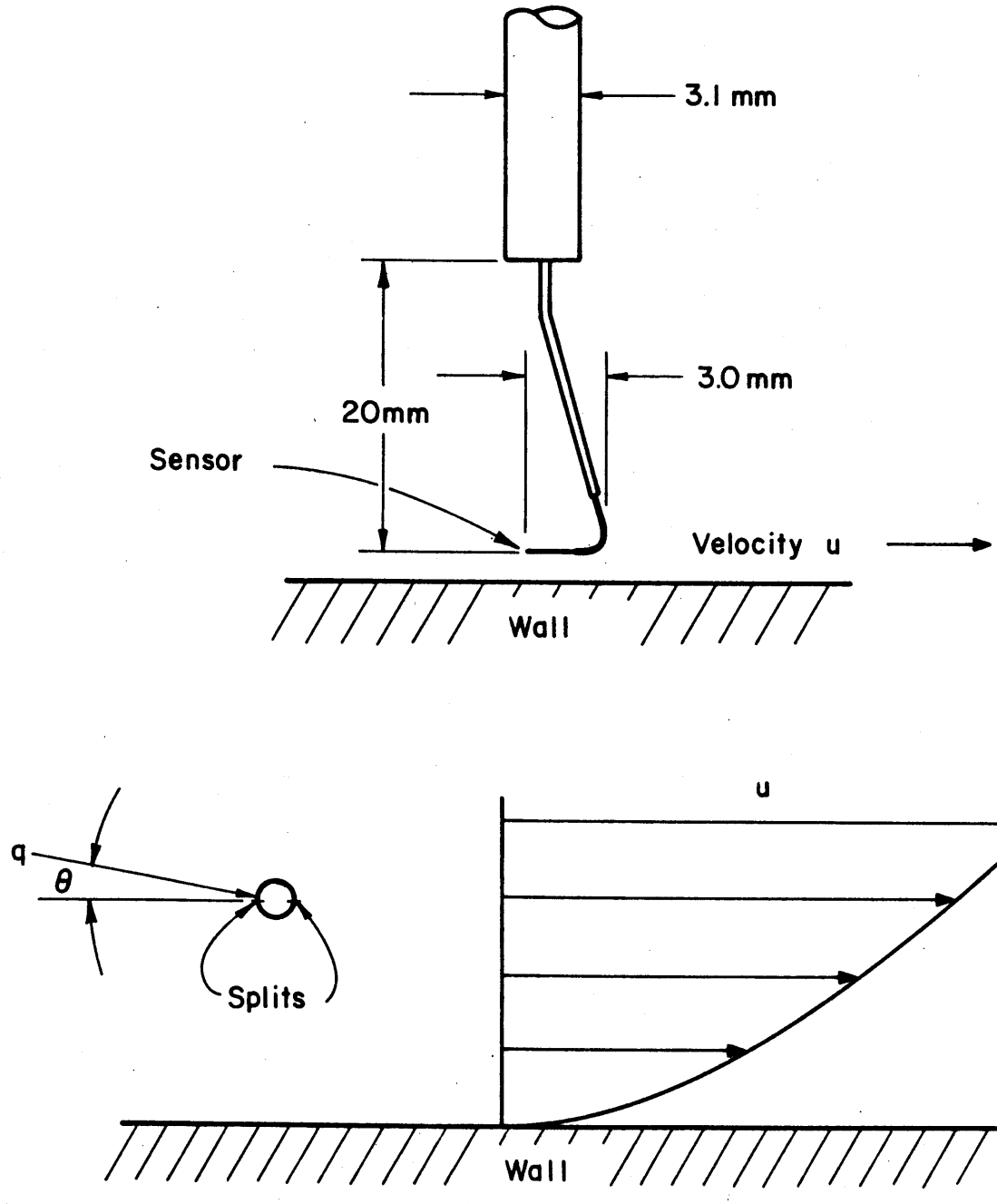

Figure 5-4. Schematic of split-film hot-film sensor and its use.

The velocity probes were positioned across the channel with a motorized traverse and vertically positioned with a depth point gage. Typically, the depth was set and the probe traversed across the channel with the motorized traverse. The system is illustrated in Figure 5-5. A 12-volt DC motor geared down to a low rpm powered the traverse. A potentiometer connected by a worm and worm gear was used to determine the position of the traverse, knowing the change in resistance per inch of travel. For measurements very close to the boundary an X-Y micrometer system was mounted on the depth point gage. The traverse system provided fast, accurate positioning for complete velocity contours or for velocity gradient analysis near the wall.

5.4 Digital Data Acquisition Techniques

When converting analog signals to digital form the sampling rate must be considered. Sampling at points that are too close together will yield highly correlated and redundant data, while sampling at points too far apart leads to confusion of low and high frequency components in the original data (22). According to sampling theory at least two samples per cycle are required to define a frequency component in the original data. The Nyquist or cutoff frequency is defined as the highest frequency component that can be defined for a given sampling rate and equals two times the maximum frequency of interest in the data. Previous research has shown that the maximum frequency of boundary shear stress processes in open channel flows is on the order of 250 hz with an average value of approximately 10 hz (2). Therefore, the sampling rate for this study was chosen to be 500 samples per second.

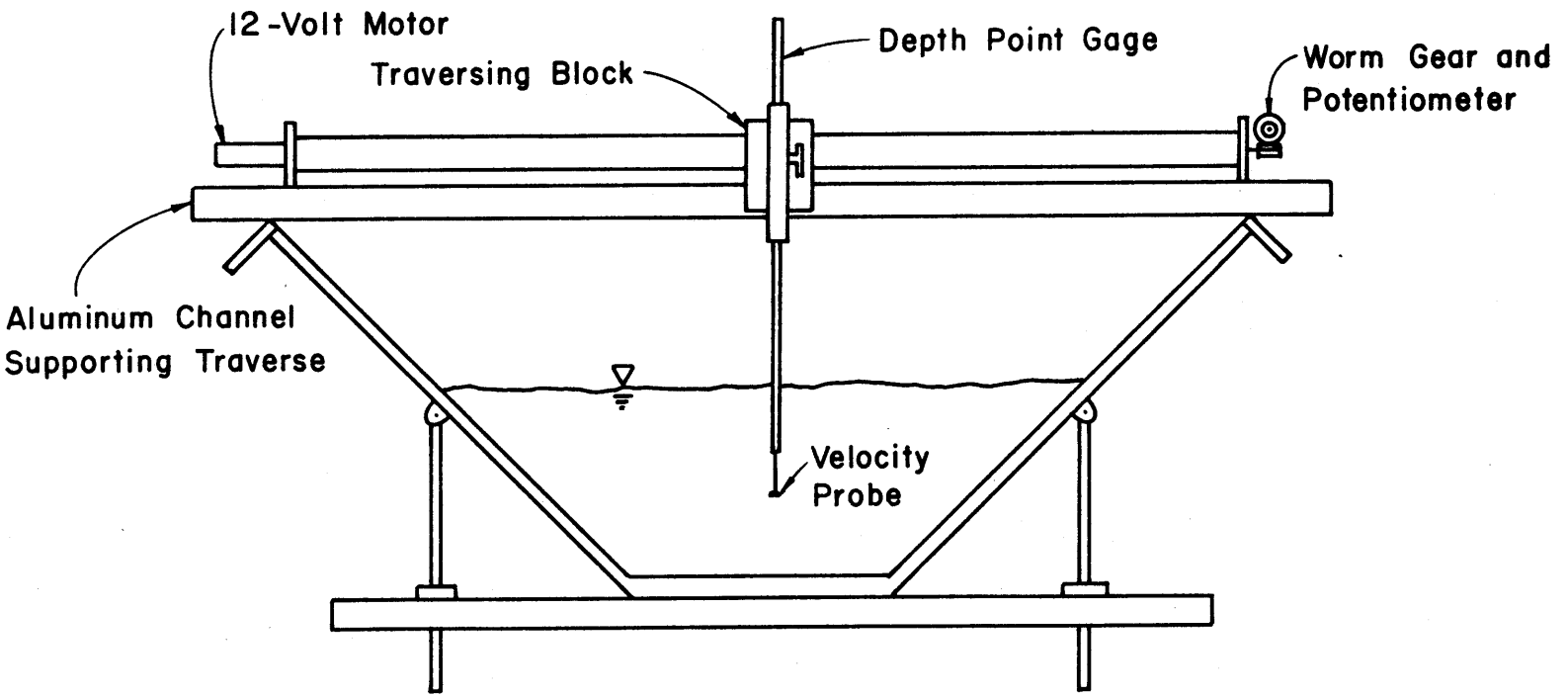

Figure 5-5. Traversing device for positioning velocity probes.

After selection of the sampling rate the analog voltage signal is transformed into a digital time series ready for analysis. If linear transfer functions were used data analysis involving the higher moments could be performed on the digital voltage time series and only the final results transformed into physical units. However, the nonlinear transfer functions of boundary shear stress (Appendix D) and velocity (Appendix E) require that the digital voltage time series be converted to physical units before analysis. With the transformed time series in physical units of boundary shear stress or velocity, the statistical moments and probability density functions (PDF) can be calculated on the computer using simple equations.

Sequential calculation of the unbiased mean and root-mean-square (RMS) of the time series of N data points (where N is large) can be calculated with only one pass through the data using the following equations:

$$\overline{X} = \frac{1}{N} \sum_i X_i \tag{5-1}$$

$$\begin{aligned} VAR &= \frac{1}{N} \sum_i (X_i - \overline{X})^2 \\ &= \frac{1}{N} \sum_i (X_i^2 - 2X_i\overline{X} + \overline{X})^2 \\ &= \frac{1}{N} \sum_i X_i^2 - \frac{1}{N} \sum_i 2X_i\overline{X} + \frac{1}{N} \sum_i \overline{X}^2 \\ &= \frac{1}{N} \sum_i X_i^2 - \frac{2\overline{X}}{N} \sum_i X_i + \frac{N}{N} \overline{X}^2 \end{aligned}$$

however,

$$\frac{2\overline{X}}{N} \sum_i X_i = \frac{2\overline{X}}{N} N\overline{X} = 2\overline{X}^2$$

therefore,

$$VAR = \frac{1}{N} \sum_i X_i^2 - 2\bar{X}^2 + \bar{X}^2$$

$$VAR = \frac{1}{N} \sum_i X_i^2 - \bar{X}^2 \qquad (5\text{-}2)$$

where X_i represents the ith value of the time series with N total points, $\bar{X}$ is the mean value and VAR is the variance of the time series. The RMS is the square root of the variance. Using Equations (5-1) and (5-2), the mean and RMS of the time series can be calculated simultaneously by summing X_i and X_i^2.

Calculation of the PDF on a computer is a counting process. Summing the number of occurrences in a given interval (called a pocket or bin) and dividing by the total number of occurrences gives the probability histogram:

$$P_i = \frac{N_i}{N} \qquad (5\text{-}3)$$

where P_i is the sample probability that $[d_{j-1} \leq X \leq d_j]$, N_i is the number of occurrences in the interval from d_{j-1} to d_j and N is the total number of data points. The probability density function is

$$p_j = \frac{N_i K}{N(b-a)} \qquad (5\text{-}4)$$

where K is the number of subintervals for the range $a < X < b$. The proper number of subintervals is (23)

$$K = 1.87\ (N - 1)^{2/5} - 2\ . \qquad (5\text{-}5)$$

A standardized PDF is computed by transforming the time series according to

$$XS_i = \frac{X_i - \overline{X}}{\sigma} \tag{5-6}$$

where XS is the standardized variable, and σ is the RMS. Computation of the first four moments of the standardized variable is then

$$X^i = \frac{1}{N} \sum_i XS_i{}^i \tag{5-7}$$

where X^i is the ith moment.

Testing the hypothesis that the experimental distribution follows a theoretical distribution can be done with chi-square or Smirnov-Kolmogorov statistics. The chi-square statistic is based on the averaged cumulative difference between the two distributions, while the Smirnov-Kolmogorov is based on the maximum difference between the two distributions. The chi-square statistic is computed digitally on a computer by the formula

$$X^2 = \sum_{J=1}^{K} \frac{(N_j - F_j)^2}{F_j} \tag{5-8}$$

where F_j is the expected frequency in the interval of the theoretical distribution. The Smirnov-Kolmogorov statistic is computed as

$$\Delta = MAX|CD(X) - P(x)| \tag{5-9}$$

where Δ is the maximum absolute difference between the theoretical cumulative density function, $CD(X)$, and the experimental density function, $P(x)$. The number of degrees of freedom for the statistics equals the number of windows or bins (subintervals) minus 3. One degree

of freedom is lost because of the requirement that the summation of the probability, P_i, must be equal to one. The additional two degrees of freedom are lost since the population mean and standard deviation are estimated from the sample data.

The two theoretical distributions to which experimental data are commonly tested for goodness of fit are the normal and lognormal distributions. An error function approximation for the theoretical normal distribution is commonly assumed in digital data analysis (23). Rather than defining a lognormal distribution for goodness of fit testing, the log values of the experimental data are tested against the normal distribution. This eliminates defining two theoretical distributions in the computer programs while still allowing goodness of fit testing to the two distributions. Proper use of this technique requires redefining the standardized variable to

$$XS_i = \frac{\log(X_i) - \overline{X}_{log}}{\sigma_{log}} \tag{5-10}$$

where $\overline{X}_{log}$ and σ_{log} are the mean and standard deviation of the log data, respectively.

VI. RESULTS OF BOUNDARY SHEAR STRESS VARIATION IN DIFFERENT GEOMETRIC SHAPE

6.1 General

The variation of boundary shear stress in the cross streamwise direction was investigated in four trapezoidal channel cross sections. Side slope ratios of 2:1, 1:1, 0.5:1 and 0:1 (where x:y refers to horizontal:vertical) were used in the variable geometry flume previously discussed. Fifteen hydraulic flow conditions consisting of five discharges and three slopes were studied for each trapezoidal cross section, resulting in a total of 60 experimental conditions. For each experiment eight locations of boundary shear stress were measured using TSI Model 1237W FSHF sensors. Measurements were taken on one-half of the channel bottom at four evenly spaced locations and also on the channel side at the 0.2, 0.4, 0.6 and 0.8 relative depths (y_i/h).

6.2 Basic Hydraulic Data and Experimental Accuracy

A summary of the hydraulic flow conditions for the 60 experimental runs is presented in Table 6-1. A complete listing of the boundary shear stress data is provided in Appendix F. Different hydraulic and geometric flow conditions are identified in these tables by a four digit experiment number. The first digit identifies the measuring location. Locations 1, 3, 5, and 7 were on the channel bottom with location 1 on the centerline. The centerline value is reported thoughout Table 6-1. Locations 2, 4, 6 and 8 refer to relative depths, y/h, of 0.2, 0.4, 0.6 and 0.8. A definition sketch of measuring locations is given in Figure 6-1. The second digit identifies the geometric side slope of the trapezoidal channels. The values 0,5,1 and 2 refer to side slope ratios of 0:1, 0.5:1, 1:1 and 2:1. The final two digits of the experiment number identify the hydraulic flow condition according to Table 6-2.

Table 6-1. Hydraulic flow conditions.

Experiment Number	Discharge (cm^3/s)	Bed Slope	Depth (cm)	Hydraulic Radius (cm)	Aspect Ratio	Reynolds Number	Froude Number	Measured τ ($dynes/cm^2$)	$\gamma y S$ $dynes/cm^2$
1001	2832	0.001	3.72	2.73	5.51	4.11×10^4	0.62	5.7	3.6
1002	2832	0.003	2.80	2.20	7.32	4.41	0.94	8.5	8.2
1003	2832	0.006	2.19	1.80	9.36	4.62	1.36	17.8	12.9
1004	5663	0.001	5.64	3.64	3.64	7.24	0.66	10.3	5.5
1005	5663	0.003	4.45	3.10	4.61	7.82	0.94	13.4	13.1
1006	5663	0.006	3.47	2.59	5.91	8.38	1.36	22.6	20.4
1007	8495	0.001	7.25	4.25	2.83	9.86	0.68	10.4	7.1
1008	8495	0.003	6.49	4.00	3.16	10.30	0.80	15.8	19.1
1009	8495	0.006	4.39	3.07	4.67	11.78	1.45	19.0	25.8
1010	11327	0.001	8.44	4.63	2.43	12.30	0.72	8.9	8.3
1011	11327	0.003	6.89	4.12	2.97	13.46	0.98	21.5	20.3
1012	11327	0.006	5.39	3.53	3.80	14.70	1.41	28.6	31.7
1013	14158	0.001	9.60	4.96	2.13	14.48	0.74	11.7	9.4
1014	14158	0.003	8.35	4.60	2.45	15.46	0.91	18.0	24.6
1015	14158	0.006	6.34	3.92	3.23	17.33	1.38	33.6	37.3

Table 6-1 (continued)

Experiment Number	Discharge (cm^3/s)	Bed Slope	Depth (cm)	Hydraulic Radius (cm)	Aspect Ratio	Reynolds Number	Froude Number	Measured τ ($dynes/cm^2$)	γyS $dynes/cm^2$
1501	2832	0.001	3.63	2.83	5.65	4.02×10^4	0.59	5.7	3.6
1502	2832	0.003	2.93	2.38	7.00	4.25	0.82	9.3	8.6
1503	2832	0.006	2.19	1.86	9.36	4.53	1.29	19.0	12.9
1504	5663	0.001	5.24	3.76	3.91	7.14	0.65	8.0	5.1
1505	5663	0.003	4.27	3.22	4.80	7.66	0.91	11.3	12.6
1506	5663	0.006	3.29	2.61	6.23	8.26	1.37	22.5	19.4
1507	8495	0.001	6.80	4.55	3.01	9.66	0.64	7.3	6.7
1508	8495	0.003	5.24	3.76	3.91	10.71	0.98	14.3	15.4
1509	8495	0.006	4.18	3.16	4.90	11.56	1.40	25.0	24.6
1510	11327	0.001	7.80	5.02	2.63	12.12	0.68	11.0	7.6
1511	11327	0.003	5.70	4.00	3.60	13.83	1.14	18.0	16.8
1512	11327	0.006	4.75	3.49	4.32	14.78	1.53	28.2	28.0
1513	14158	0.001	8.96	5.52	2.29	14.18	0.67	11.5	8.8
1514	14158	0.003	7.35	4.81	2.79	15.67	0.94	21.4	21.6
1515	14158	0.006	5.85	4.08	3.50	17.12	1.36	30.1	34.4

Table 6-1 (continued)

Experiment Number	Discharge (cm^3/s)	Bed Slope	Depth (cm)	Hydraulic Radius (cm)	Aspect Ratio	Reynolds Number	Froude Number	Measured τ ($dynes/cm^2$)	$\gamma y S$ $dynes/cm^2$
1101	2832	0.001	3.38	2.68	6.06	3.82×10^4	0.61	4.3	3.3
1102	2832	0.003	2.59	2.15	7.92	4.13	0.94	8.2	7.6
1103	2832	0.006	2.07	1.77	9.90	4.36	1.34	12.9	12.2
1104	5663	0.001	4.91	3.63	4.17	6.69	0.65	8.3	4.8
1105	5663	0.003	3.93	3.04	5.22	7.27	0.95	12.8	11.6
1106	5663	0.006	3.14	2.53	6.53	7.83	1.37	22.0	18.4
1107	8495	0.001	6.25	4.38	3.28	9.04	0.65	10.4	6.1
1108	8495	0.003	4.97	3.66	4.13	9.98	0.96	13.2	14.6
1109	8495	0.006	3.87	3.00	5.30	10.97	1.46	26.7	22.8
1110	11327	0.001	7.34	4.95	2.79	11.15	0.65	10.0	7.2
1111	11327	0.003	5.76	4.11	3.56	12.50	1.00	16.0	16.9
1112	11327	0.006	4.42	3.34	4.64	13.94	1.56	25.5	26.0
1113	14158	0.001	8.11	5.34	2.53	13.24	0.68	11.0	8.0
1114	14158	0.003	6.71	4.62	3.05	14.56	0.96	22.2	19.7
1115	14158	0.006	5.36	3.89	3.82	16.12	1.41	33.6	31.5

Table 6-1 (continued)

Experiment Number	Discharge (cm^3/s)	Bed Slope	Depth (cm)	Hydraulic Radius (cm)	Aspect Ratio	Reynolds Number	Froude Number	Measured τ ($dynes/cm^2$)	$\gamma y S$ $dynes/cm^2$
1201	2832	0.001	3.20	2.47	6.41	3.3×10^4	0.59	4.1	3.1
1202	2832	0.003	2.41	1.95	8.51	3.68	0.95	7.0	7.1
1203	2832	0.006	1.92	1.61	10.68	3.95	1.40	11.5	11.3
1204	5663	0.001	4.69	3.80	4.37	5.55	0.60	6.6	4.6
1205	5663	0.003	3.35	2.57	6.12	6.48	1.08	11.2	9.9
1206	5663	0.006	2.80	2.21	7.32	6.96	1.49	16.9	16.5
1207	8495	0.001	5.49	3.84	3.73	7.66	0.67	9.1	5.4
1208	8495	0.003	4.15	3.06	4.94	8.83	1.11	15.0	12.2
1209	8495	0.006	3.54	2.69	5.79	9.49	1.48	22.2	20.8
1210	11327	0.001	6.43	4.36	3.19	9.34	0.66	8.5	6.3
1211	11327	0.003	5.12	3.63	4.00	10.60	1.01	15.1	15.1
1212	11327	0.006	4.30	3.15	4.77	11.58	1.39	18.3	25.3
1213	14158	0.001	7.39	4.87	2.77	10.74	0.64	8.0	7.25
1214	14158	0.003	5.49	3.84	3.73	12.76	1.12	14.4	16.2
1215	14158	0.006	4.72	3.40	4.34	13.82	1.47	25.5	27.8

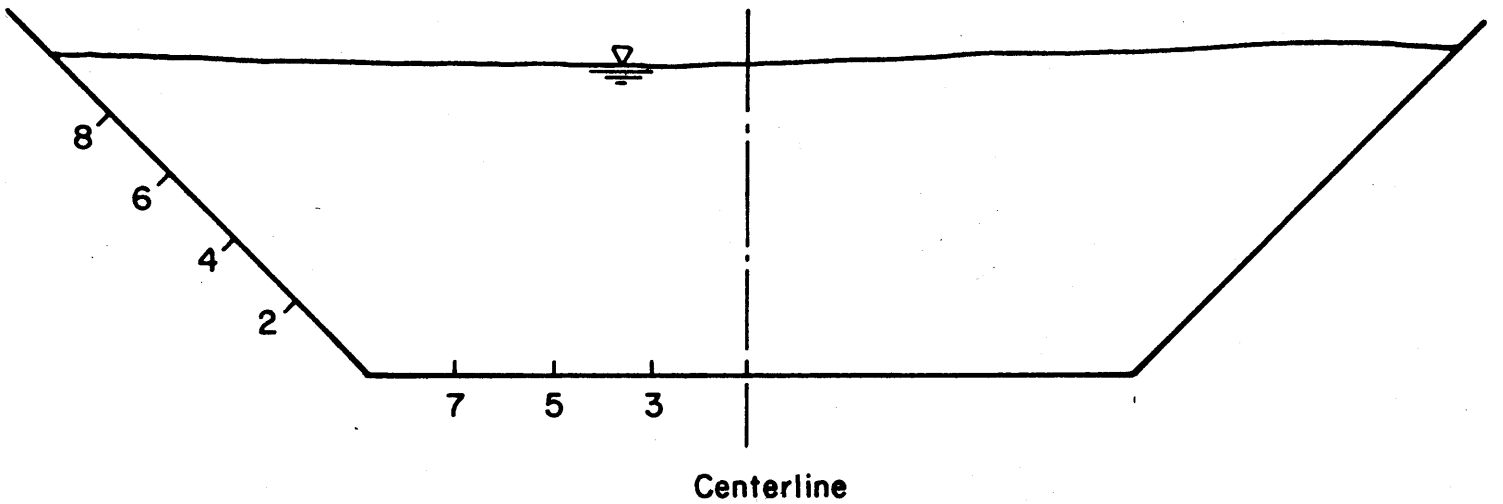

Figure 6-1. Definition sketch showing location numbers for boundary shear stress measurement.

Table 6-2. Hydraulic flow condition identification numbers.

Number	Discharge cm^3/s	Bed Slope
01	2832	0.001
02	2832	0.003
03	2832	0.006
04	5663	0.001
05	5663	0.003
06	5663	0.006
07	8495	0.001
08	8495	0.003
09	8495	0.006
10	11327	0.001
11	11327	0.003
12	11327	0.006
13	14158	0.001
14	14158	0.003
15	14158	0.006

The Reynolds number range was from 3.30×10^5 to 1.73×10^5 and the Froude number range was from 0.59 to 1.48. The length dimension in the Reynolds number was 4R, where R is the hydraulic radius. Aspect ratios (width to depth ratios) were all less than 11.

To evaluate the accuracy of the experimental data the measured centerline boundary shear stress was compared to the theoretical value, $\gamma y S$. Use of the depth, y, rather than the hydraulic radius, R, as derived in Equation (2-20), results from considering a point value (centerline) rather than the mean value. The primary difficulty in using $\gamma y S$ is the evaluation of the energy slope. When the flow is uniform the bed slope is used to estimate the energy slope. However, if the flow is not strictly uniform the local energy slope may not equal the bed slope. The accuracy of shear stress prediction using $\gamma y S$ depends on the uniform flow and parallel slope assumptions. Complicating the estimate of the slope term is the accuracy of the mechanical apparatus controlling the flume bed slope. The difference in the upstream and downstream bed elevations in the variable geometry flume for a bed slope of 0.001 was only 0.36 inch. A ten percent accuracy in bed slope implies that the accuracy in bed elevation was 0.036 inch. The problems of evaluating the true slope in the tractive force equation makes accurate determination of the theoretical boundary shear stress difficult.

To estimate the true value of slope and to evaluate the accuracy of the experimental data the measured boundary shear stress values were initially assumed correct. An objective function was defined as the sum of squared differences between the theoretical shear stress, $\gamma y S$, and the assumed correct measured data, or

$$OBJ = \sum_{i=1}^{60} (\gamma y_i S - \hat{\tau}_i)^2 \qquad (6\text{-}1)$$

where $\hat{\tau}_i$ is the assumed correct measured shear stress on the flume centerline. To minimize the objective function, optimization of the slope was required. Nearly uniform flow existed for all 60 flow conditions; therefore, if the optimized slope and the known bed slope were approximately equal, the assumption that the measured shear stress values were the correct values would be valid by indirect proof. If wide discrepancies existed in the slope calculation, the assumption that the measured shear stress was correct would be unreasonable. The results are presented in Table 6-3 and indicate that the higher values of bed slope were more accurate.

Table 6-3. Bed slope optimization results.

Assumed Bed Slope	Optimized Bed Slope
0.0010	0.0014
0.0030	0.0029
0.0060	0.0060

However, it can be concluded that on the average the measured values were correct. The higher discrepancy at bed slope 0.0010 could result from local nonuniform flow because at the lower slopes water surface disturbances were more pronounced. Water surface slopes that were measured for bed slopes of 0.0010 on the average were closer to the optimized slope value than the assumed bed slope.

Using the optimized slope values, the correlation coefficient between γyS and the measured centerline shear stress was computed. The correlation values were all greater than 0.86 and indicated a strong relationship between the two estimates at each bed slope. Figures 6-2 to 6-4 show γyS and the measured values plotted with the line of

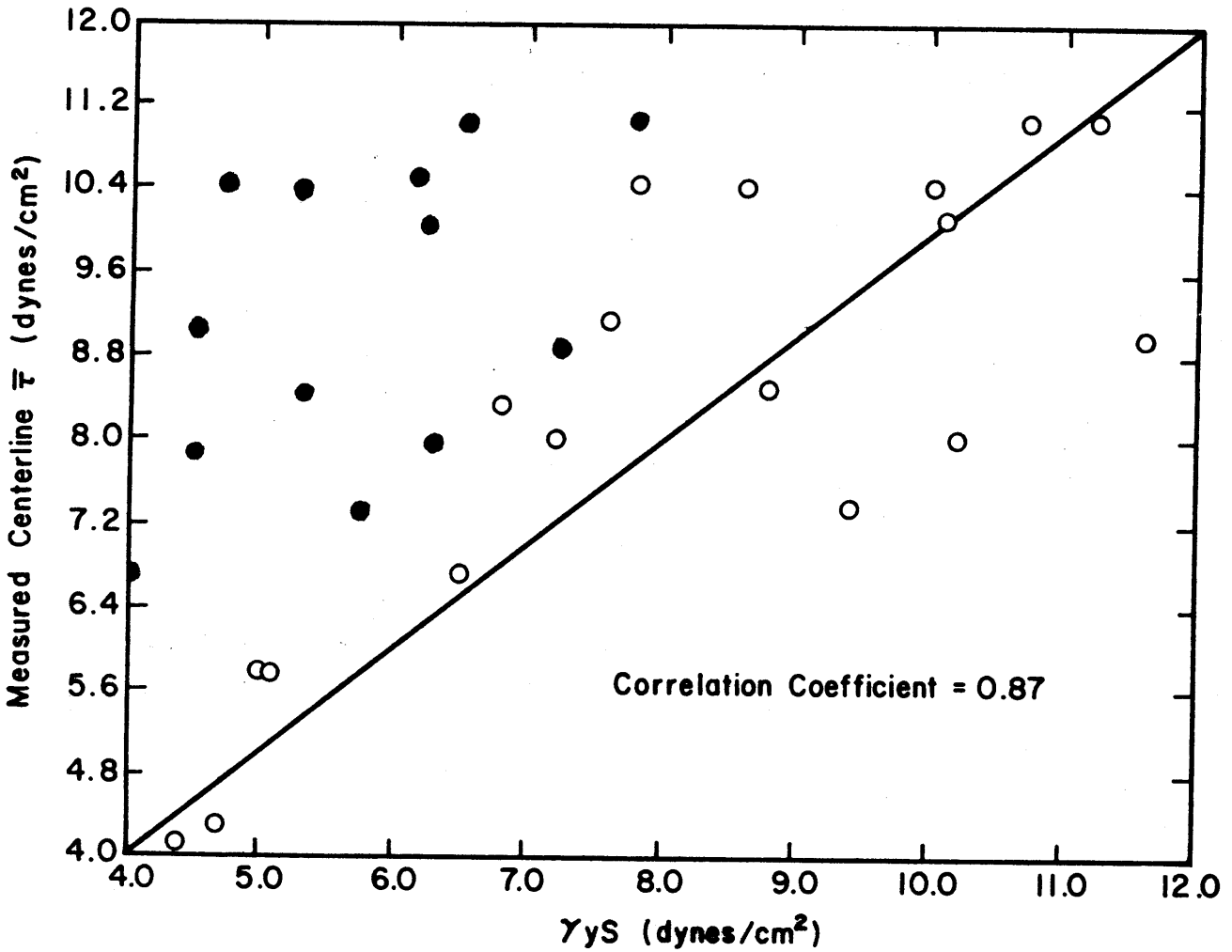

Figure 6-2. Relation of γyS and measured shear stress for bed slope 0.001 (open circles based on optimized bed slope, solid circles based on assumed bed slope).

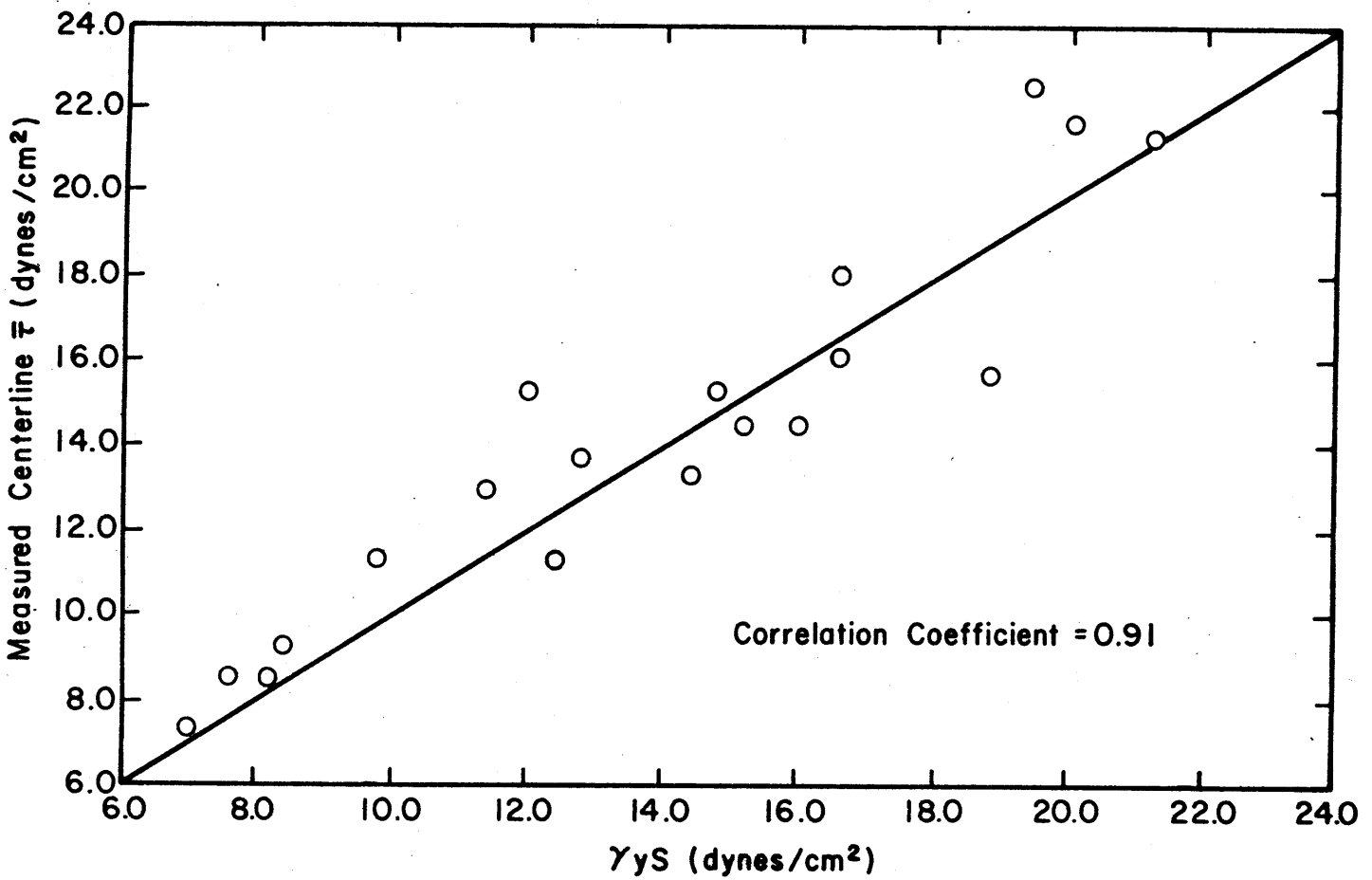

Figure 6-3. Relation of γyS and measured shear stress for bed slope 0.003.

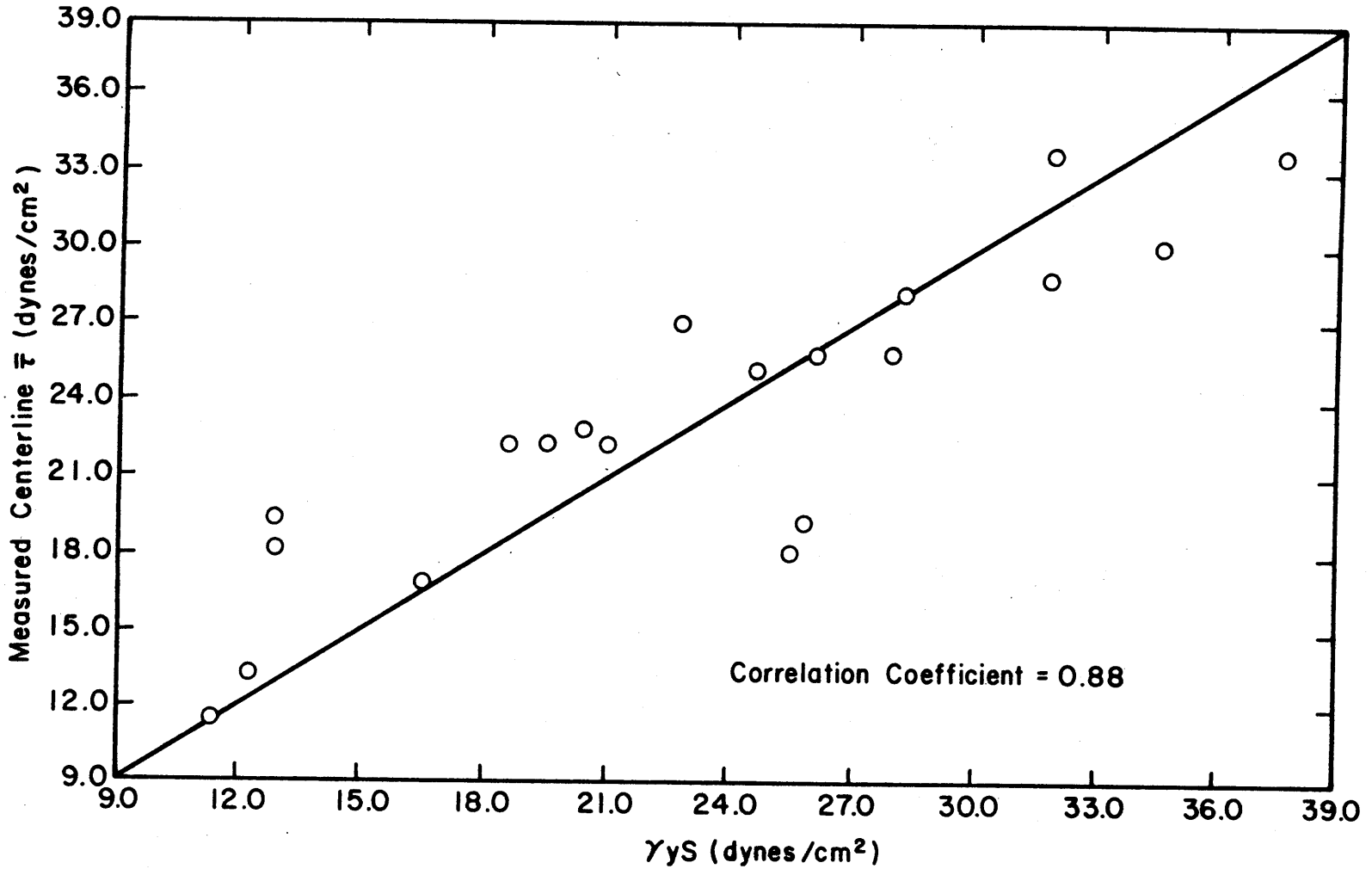

Figure 6-4. Relation of γyS and measured shear stress for bed slope 0.006.

perfect agreement (45° line). Figure 6-2 also shows the theoretical shear stress values (γyS) based on the assumed bed slope of 0.0010.

6.3 Maximum Shear Stress Results

The results of Lane (1) and Olsen and Florey (12) indicated that for trapezoidal channels the ratio of maximum shear stress on the side of the channel to γyS, and the ratio of maximum shear stress on the channel bottom to γyS were 0.75-0.76 and 0.97, respectively. For the 60 experimental conditions studied, with four measuring locations on the side and four on the bottom, the measured data agree closely with these results. The average value of the ratio on the side was 0.67 and the average value for the ratio on the bottom was 0.97. The range of the ratio on the side was 0.44 to 0.93 and the range of the ratio on the bottom was 0.65 to 1.28. The maximum relative shear stress showed no distinct relation to AR as illustrated by Figure 6-5. The maximum relative shear stress did tend to increase with increasing channel side slope. The analytical data of Lane (1) using membrane analogy, finite differences and mathematical techniques is also reproduced on Figure 6-5.

Replogle and Chow (13) reported that the maximum shear stress occurred slightly off center for flow in circular channels. Kartha and Leutheusser (17) also reported the maximum relative shear stress (where the relative shear stress is the value of shear stress at a given point divided by the mean shear stress for the cross section) occurred off the centerline in rectangular channels. For the experimental data of this investigation 70 percent of the observed maximum values occurred off the centerline.

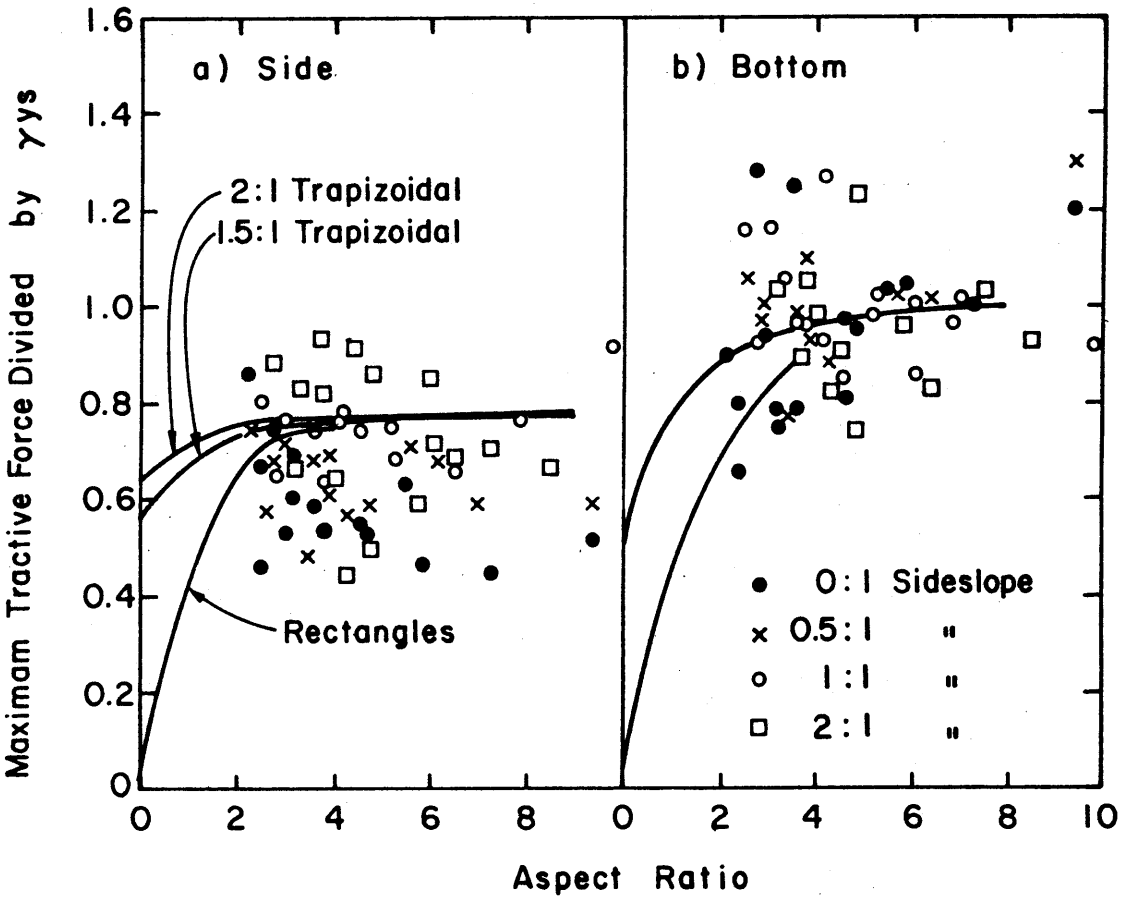

Figure 6-5. Maximum relative shear stress as a function of aspect ratio (solid lines indicate Lane relationship (1)).

The average ratio of maximum shear stress on the side to maximum shear stress on the bottom is given in Table 6-4 for each side slope.

Table 6-4. Average ratio of maximum side shear stress to maximum bottom shear stress.

Side Slope	Ratio
0:1	0.64
0.5:1	0.64
1:1	0.75
2:1	0.76

The overall average for all 60 flow conditions was 0.69.

6.4 Shear Stress Spatial Distribution Results

The spatial distribution of relative shear stress is presented in Figures 6-6 to 6-13. The number for each line refers to the hydraulic flow condition identified in Table 6-2. Similar to the conclusions of Ippen and Drinker (14) the boundary shear stress spatial patterns cannot be predicted quantitatively from mean flow characteristics; however, qualitative statements can be made.

The general trend of relative shear stress on the channel bottom is greater than 1.0 and on the channel side it is less than 1.0. The range of relative shear stress tends to decrease as the side slope increases. Increasing aspect ratio and increasing side slope imply smaller depth of flow and a closer approximation to a hydraulically wide channel. In a wide channel the effects of free surface and secondary current on boundary shear stress distribution are less pronounced relative to the mean flow (13) and the shear stress tends to be more uniform under these conditions (18).

The relative shear stress on the channel side tends to diverge more widely as the water surface is approached. The irregularity of

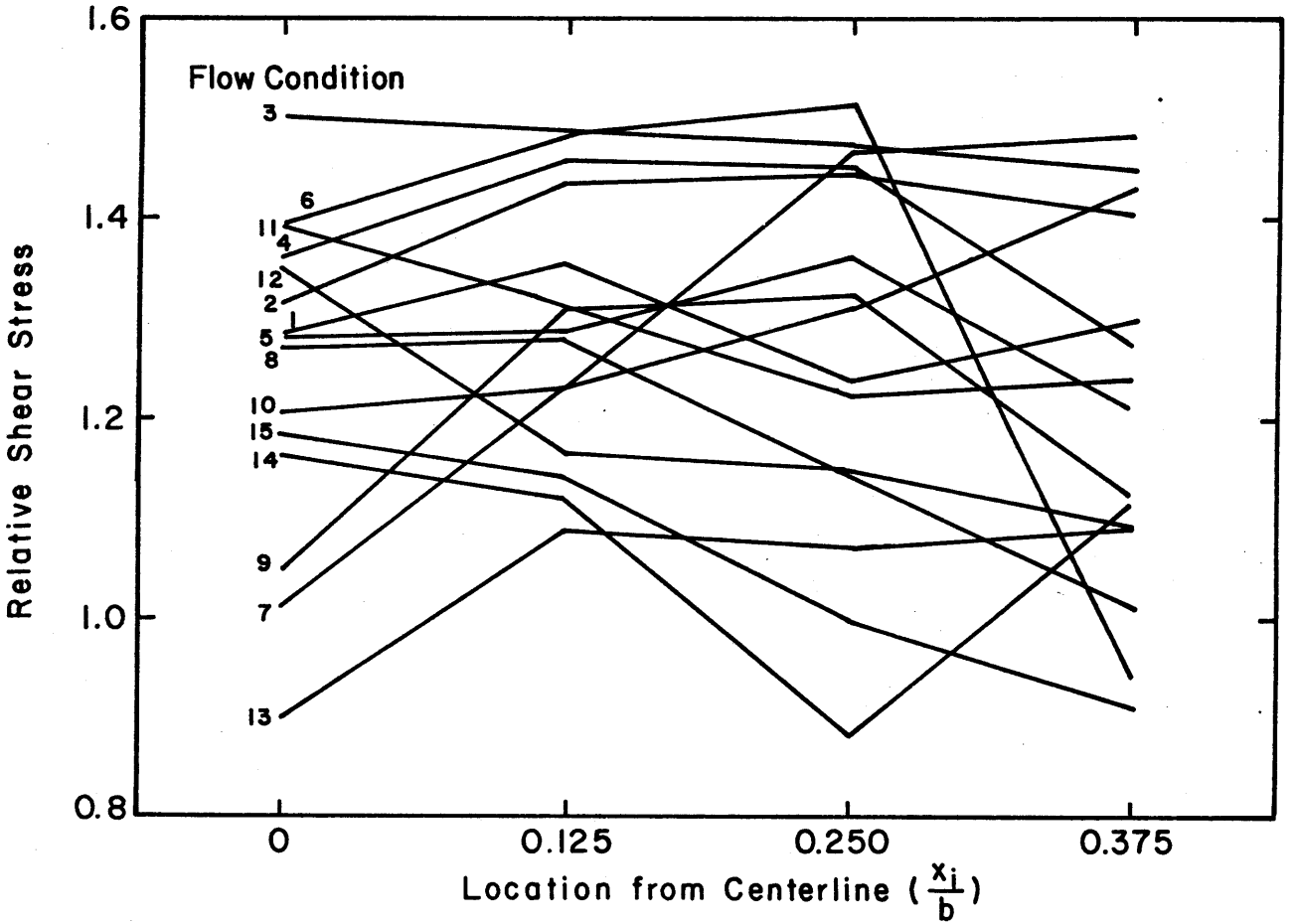

Figure 6-6. Boundary shear stress variation on channel bottom for side slope 0:1

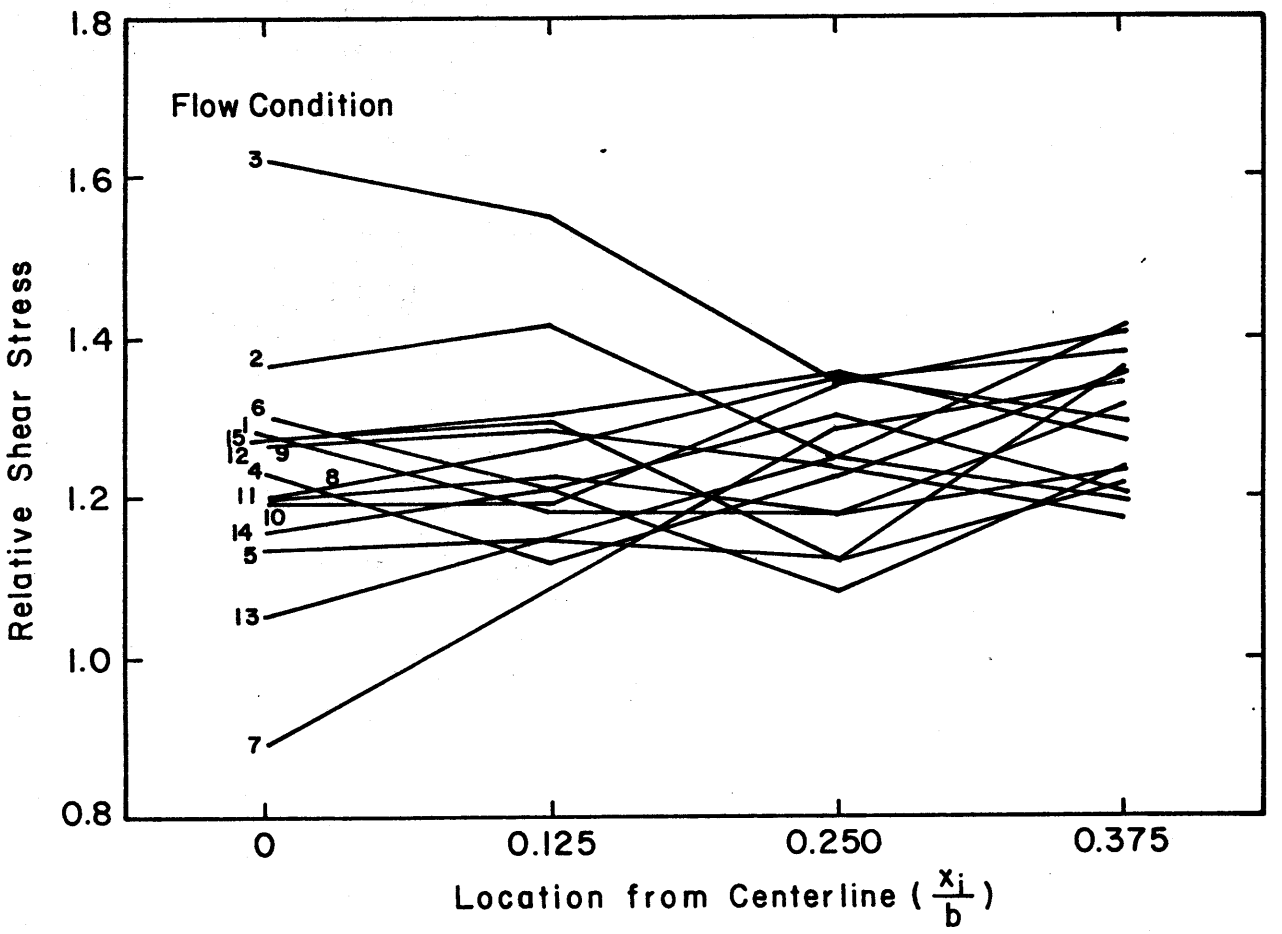

Figure 6-7. Boundary shear stress variation on channel bottom for side slope 0.5:1

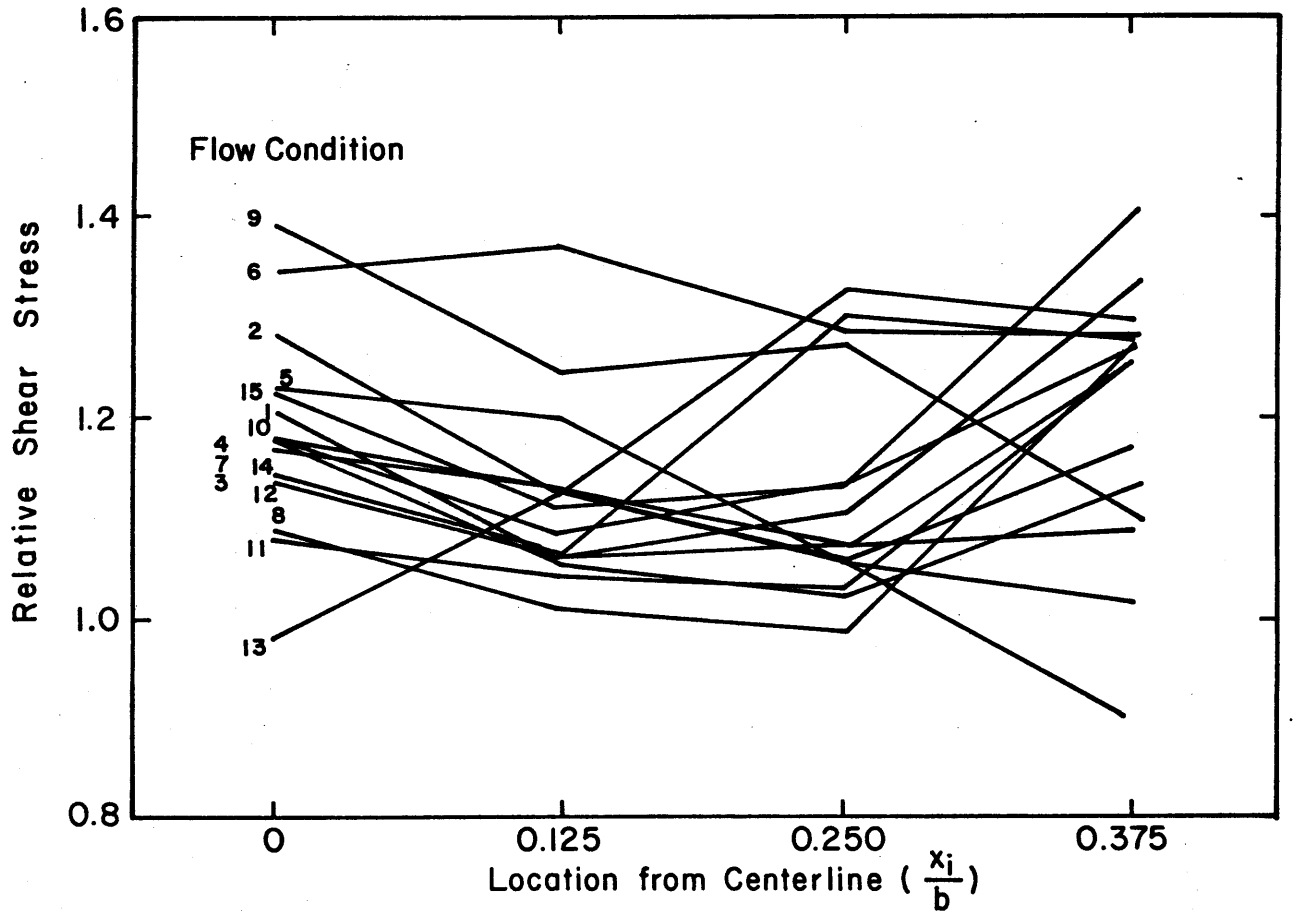

Figure 6-8. Boundary shear stress variation on channel bottom for side slope 1:1

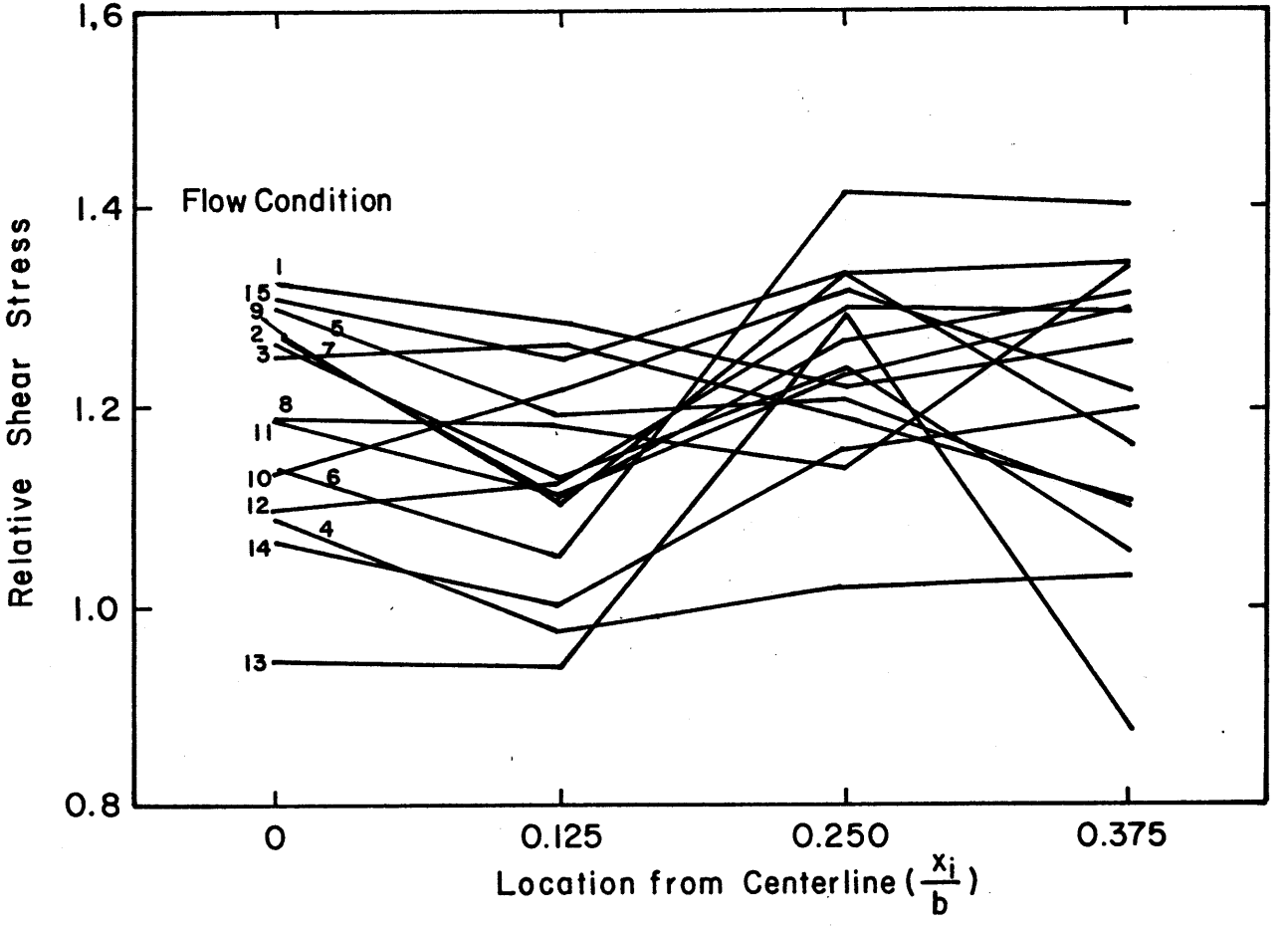

Figure 6-9. Boundary shear stress variation on channel bottom for side slope 2:1

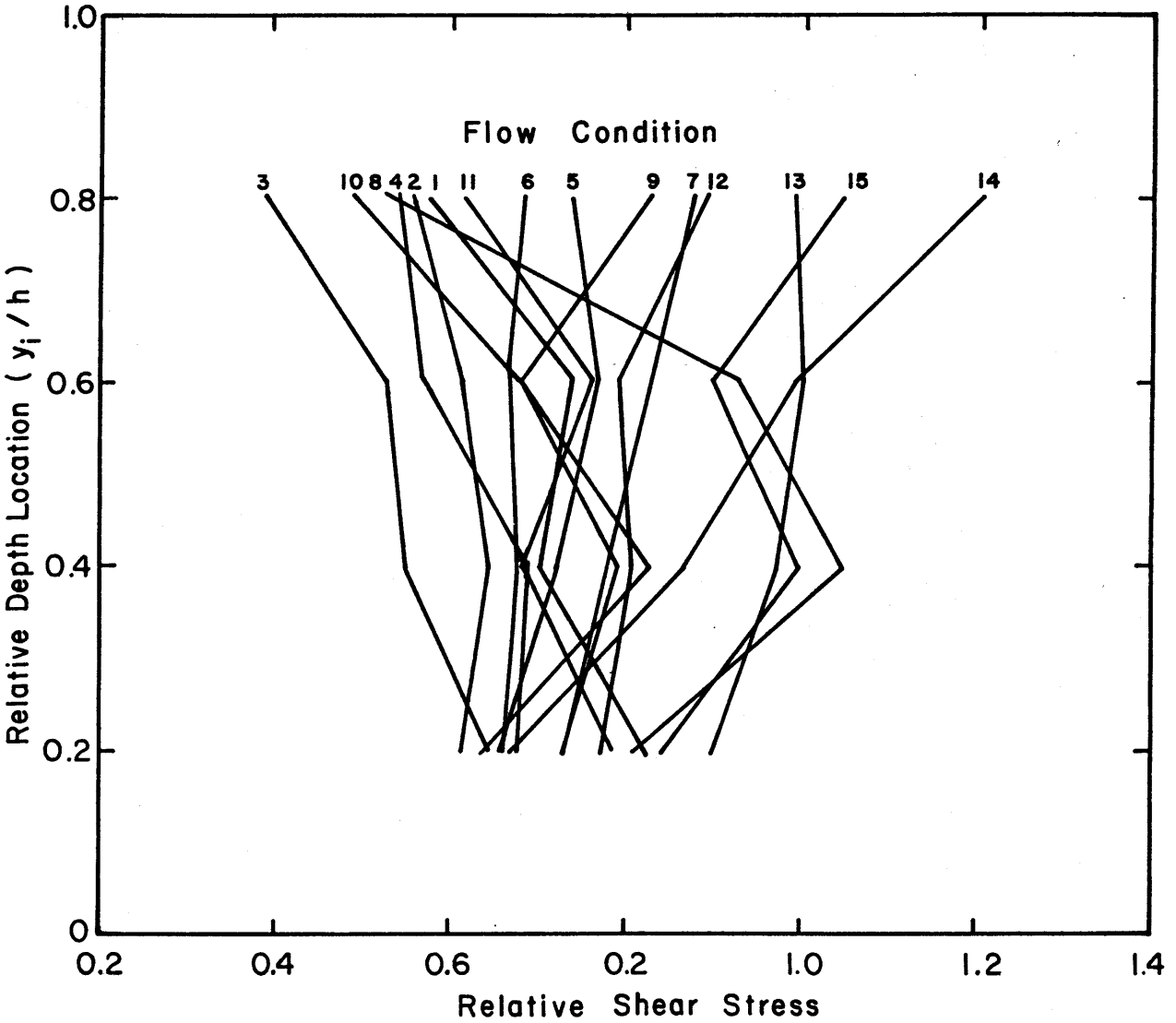

Figure 6-10. Boundary shear stress variation on channel side for side slope 0:1

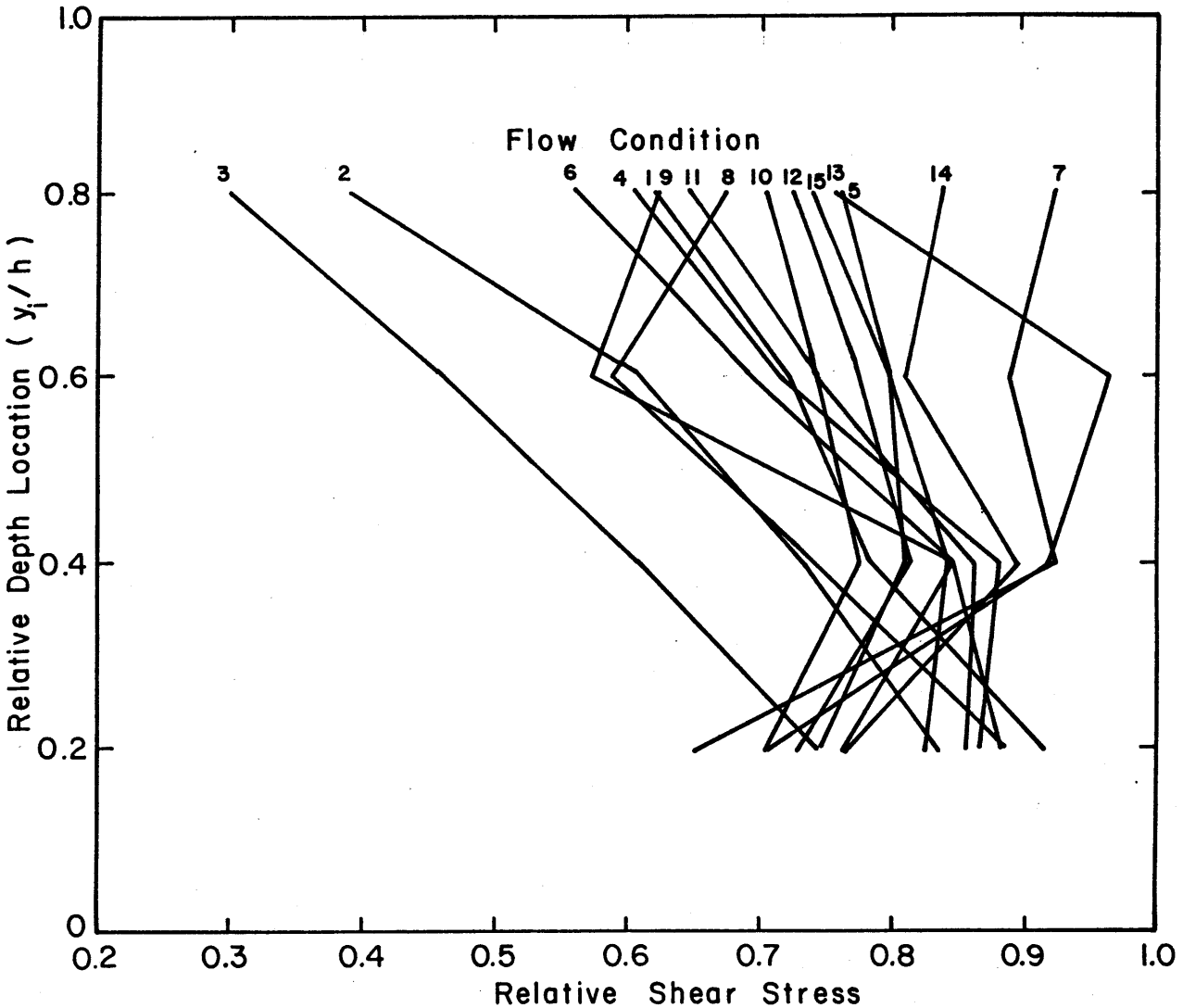

Figure 6-11. Boundary shear stress variation on channel side for side slope 0.5:1

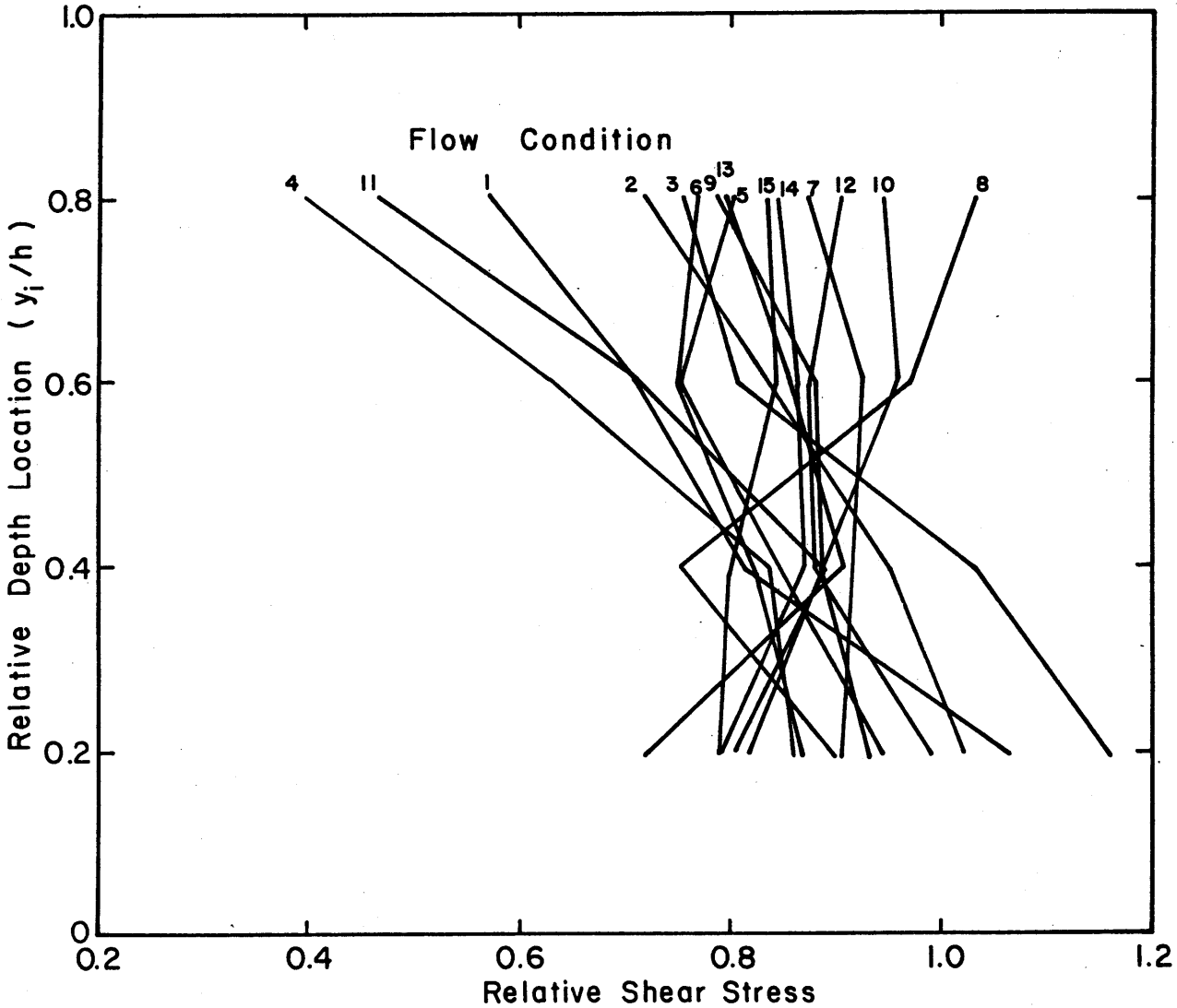

Figure 6-12. Boundary shear stress variation on channel side for side slope 1:1

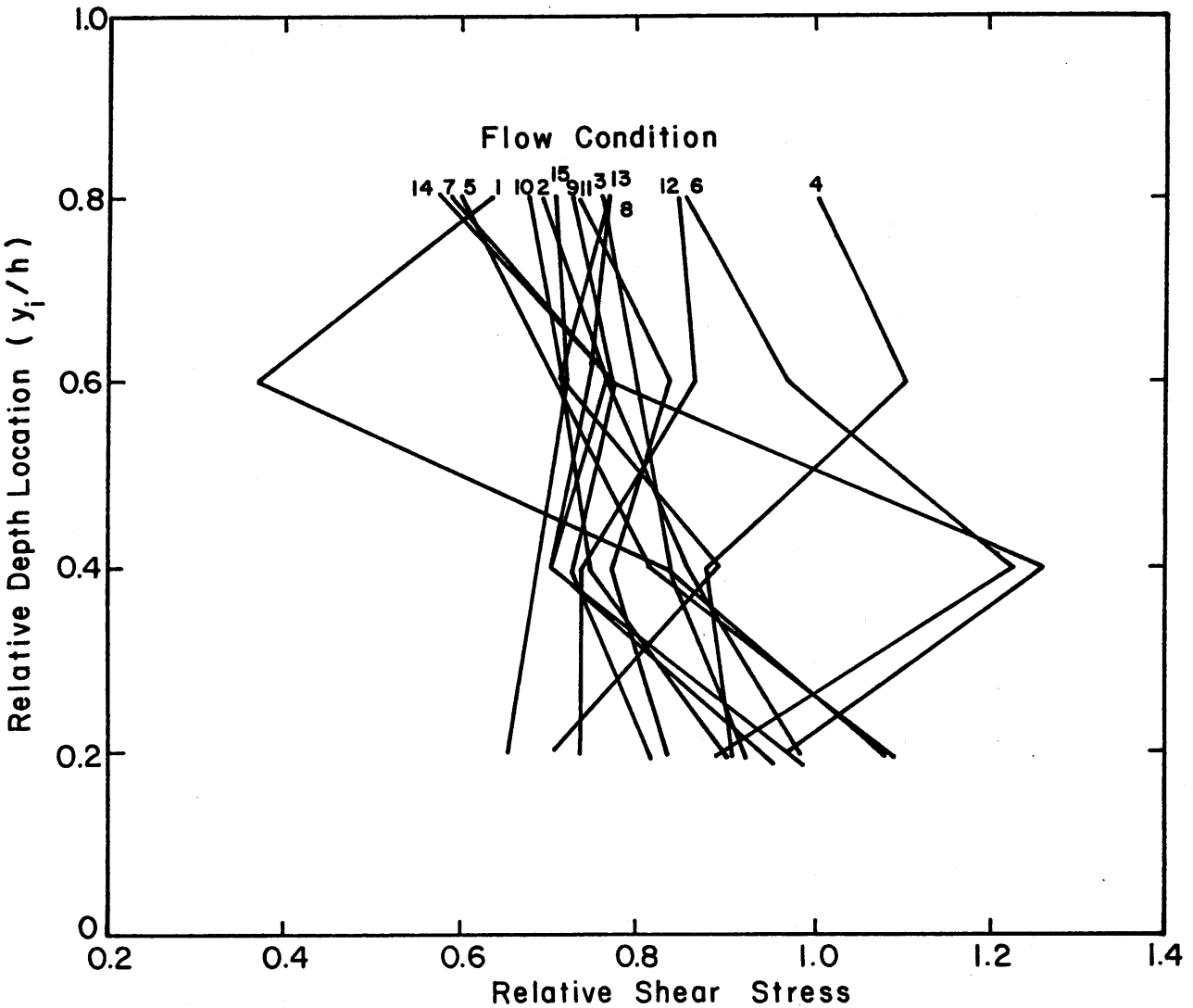

Figure 6-13. Boundary shear stress variation on channel side for side slope 2:1

shear stress near the water surface is probably the result of surface tension and water surface instabilities. Similar to the results of Replogle and Chow (13) the absolute shear stress generally decreased near the water surface but did not go to zero.

6.5 Root-Mean-Square Results

The root-mean-square (RMS) of the shear stress fluctuations were evaluated at each measuring location. For a given flow condition the RMS was relatively constant regardless of location; however, the value of RMS on the bottom was generally higher than the RMS on the side. The ratio of the average RMS value on the side to the average RMS value on the bottom is given in Table 6-5 for each side slope.

Table 6-5. Ratio of average RMS on side to average RMS on bottom.

Side Slope	Aspect Ratio Range	RMS Ratio
0:1	2.1 - 9.4	0.87
0.5:1	2.3 - 9.4	0.81
1:1	2.5 - 9.9	0.93
2:1	2.8 - 10.7	1.10

For higher side slope ratio, which implies generally higher aspect ratios, the RMS ratio increases. For an RMS ratio of 1.0 the turbulent fluctuations on the bottom and side are approximately equal. This is not unlikely in a hydraulically wide channel since the influence of channel sides diminishes with increasing aspect ratio.

The RMS values generally increased with increasing Reynolds number. Figure 6-14 shows the RMS trends and indicates a relationship of increasing RMS with increasing Reynolds number. The power curve fit is also indicated on Figure 6-14.

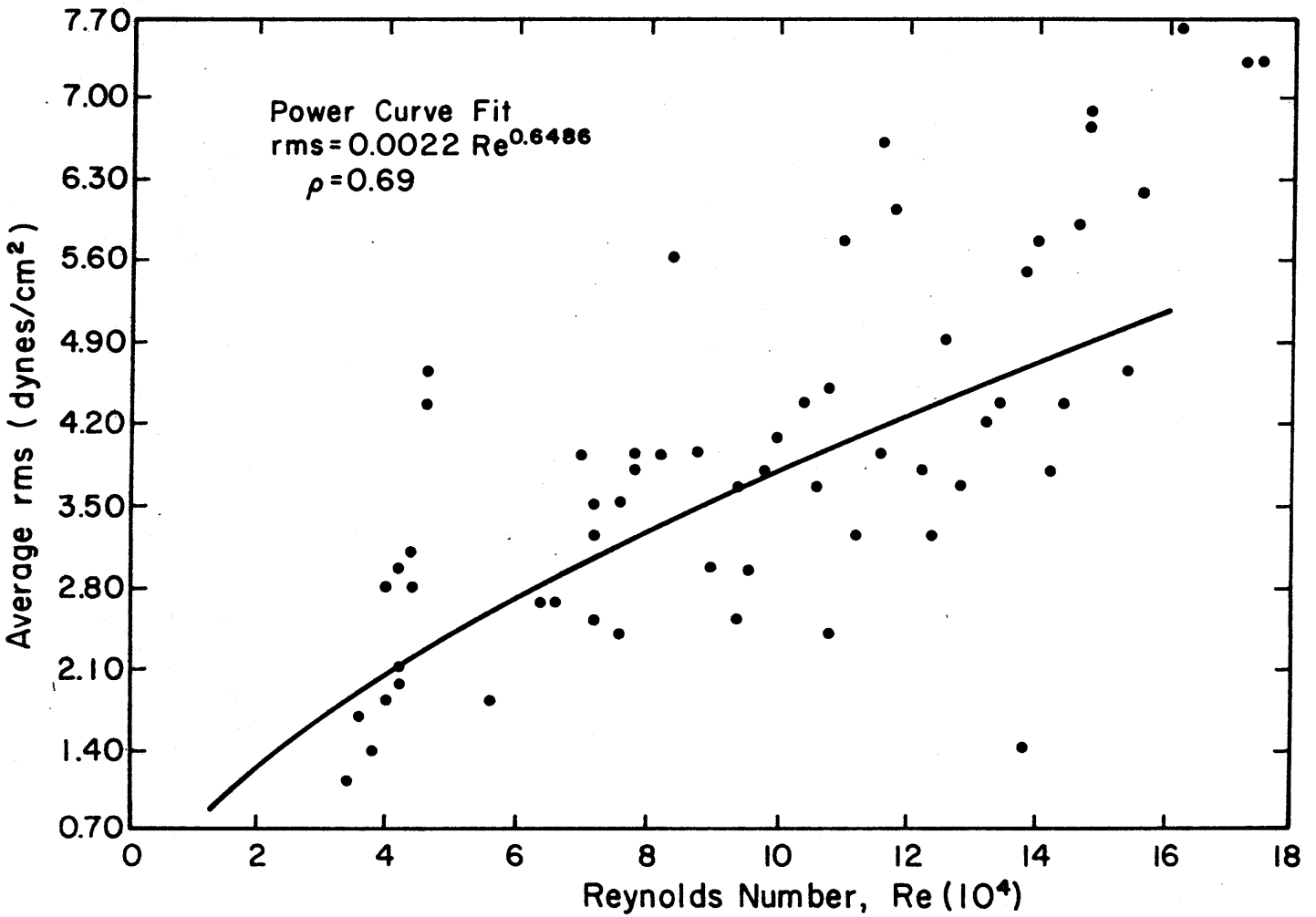

Figure 6-14. RMS trends with Reynolds number.

6.6 Statistical Results

For each measuring location the first four moments and the probability density function (PDF) were computed for the fluctuating component of shear stress. The experimental PDF distributions were tested for goodness of fit to the normal and lognormal theoretical distributions. To evaluate the hypothesis that the experimental distributions were statistically equal to the theoretical distributions, the chi-square and Smirnov-Kolmogorov (S-K) statistics were used.

Visual inspection of the plotted PDF functions and review of the estimates of skewness indicated that all of the distributions were slightly positively skewed. This trend suggests a lognormal type of distribution rather than a gaussian. According to the S-K statistic the experimental distributions were fit to both the normal and lognormal distributions at the 0.05 level of significance with 50 degrees of freedom. Inspection of the chi-square statistic shows that neither theoretical distribution fit (at the 0.05 level of significance) the experimental distributions, although the lognormal chi-square statistic was consistently less than the normal chi-square value. The goodness of fit increased with increasing Reynolds numbers. Figures 6-15 to 6-18 illustrate four typical examples. Figures 6-15 and 6-16 are for the channel bottom at the centerline position in the 1:1 side slope channel for the hydraulic flow conditions identified by numbers 3 and 14, respectively. Figures 6-17 and 6-18 are for the same channel side slope and hydraulic flow condition, but at the 0.6 relative depth on the side.

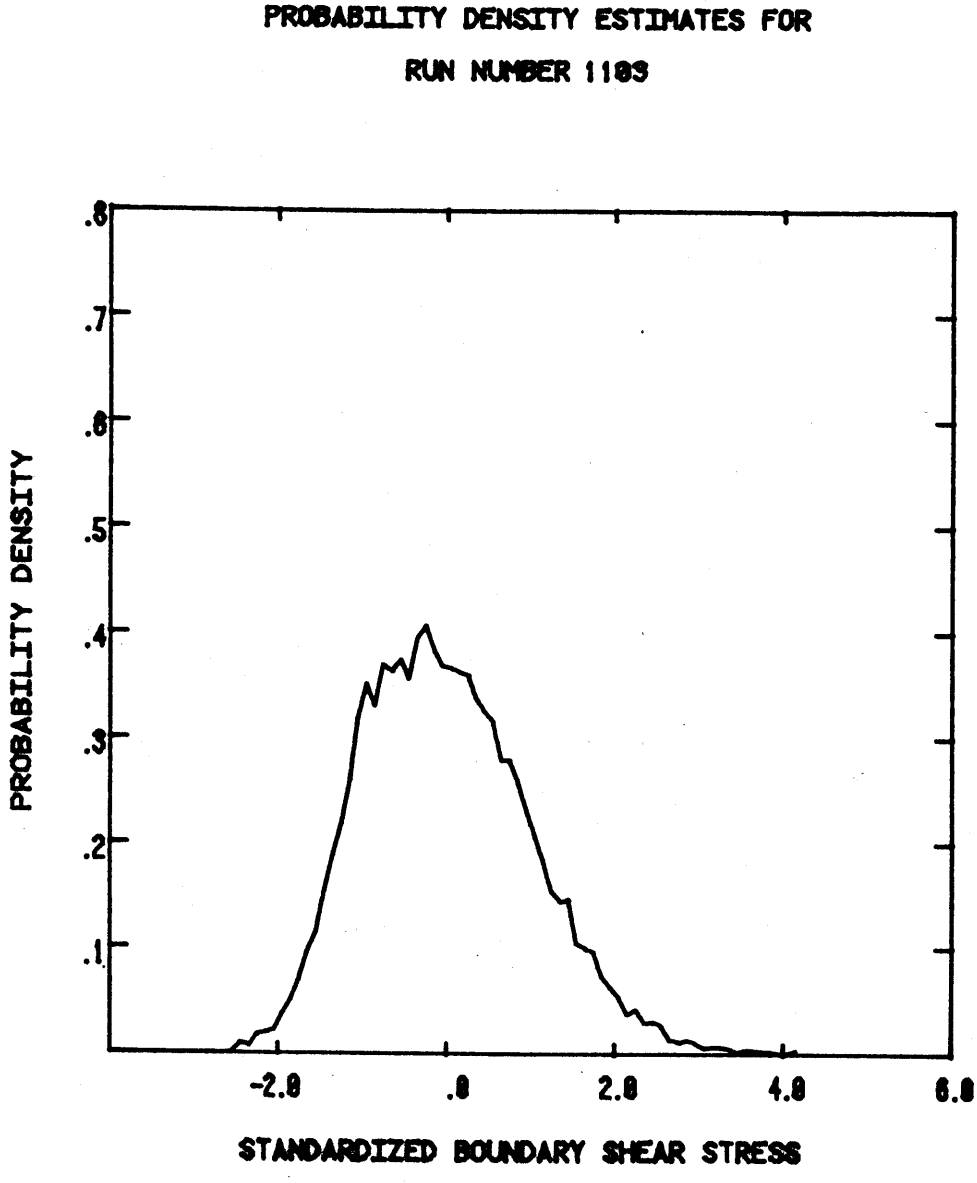

Figure 6-15. PDF estimate at channel centerline for 2832 cm^3/s and 0.006 bed slope.

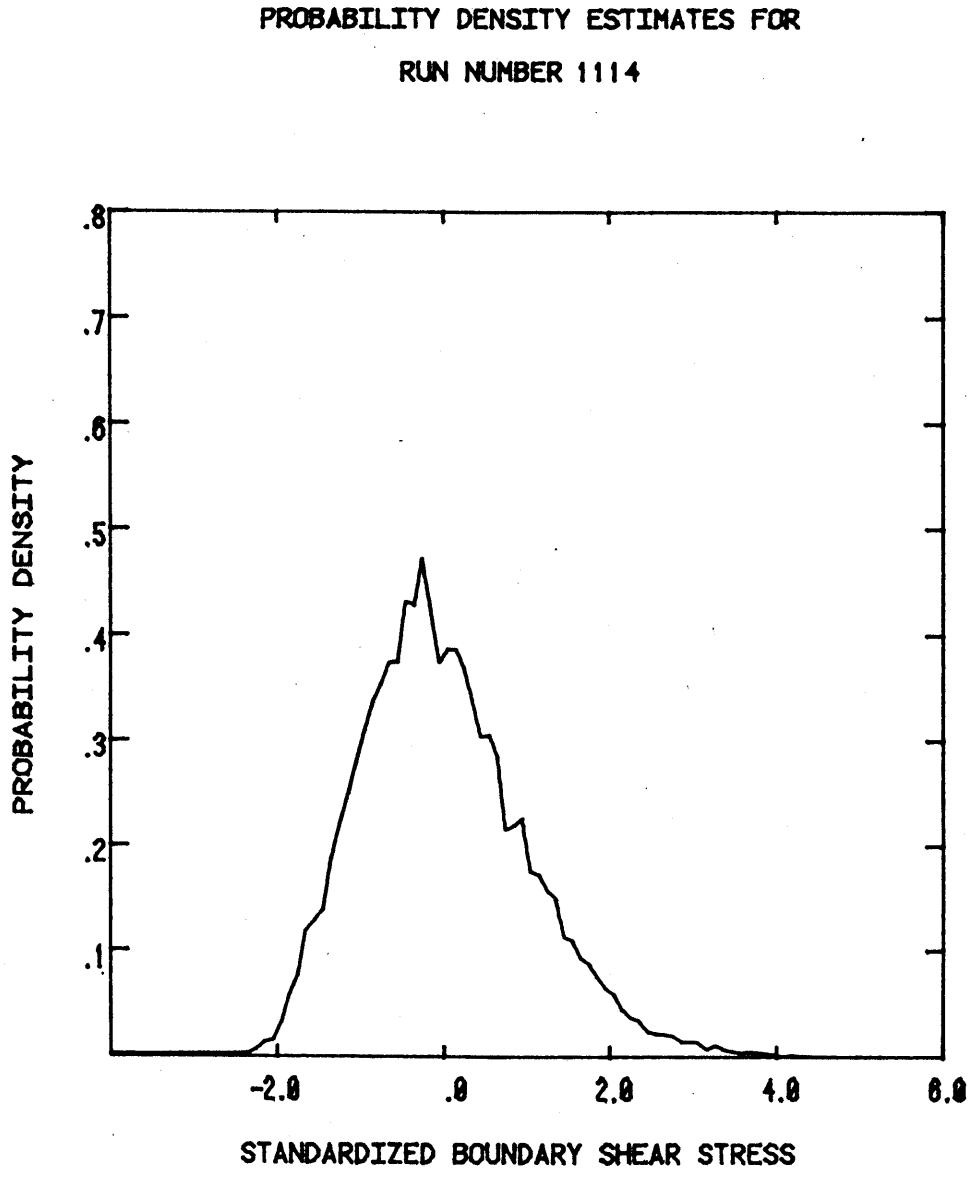

Figure 6-16. PDF estimate at channel centerline for 14158 cm^3/s and 0.003 bed slope.

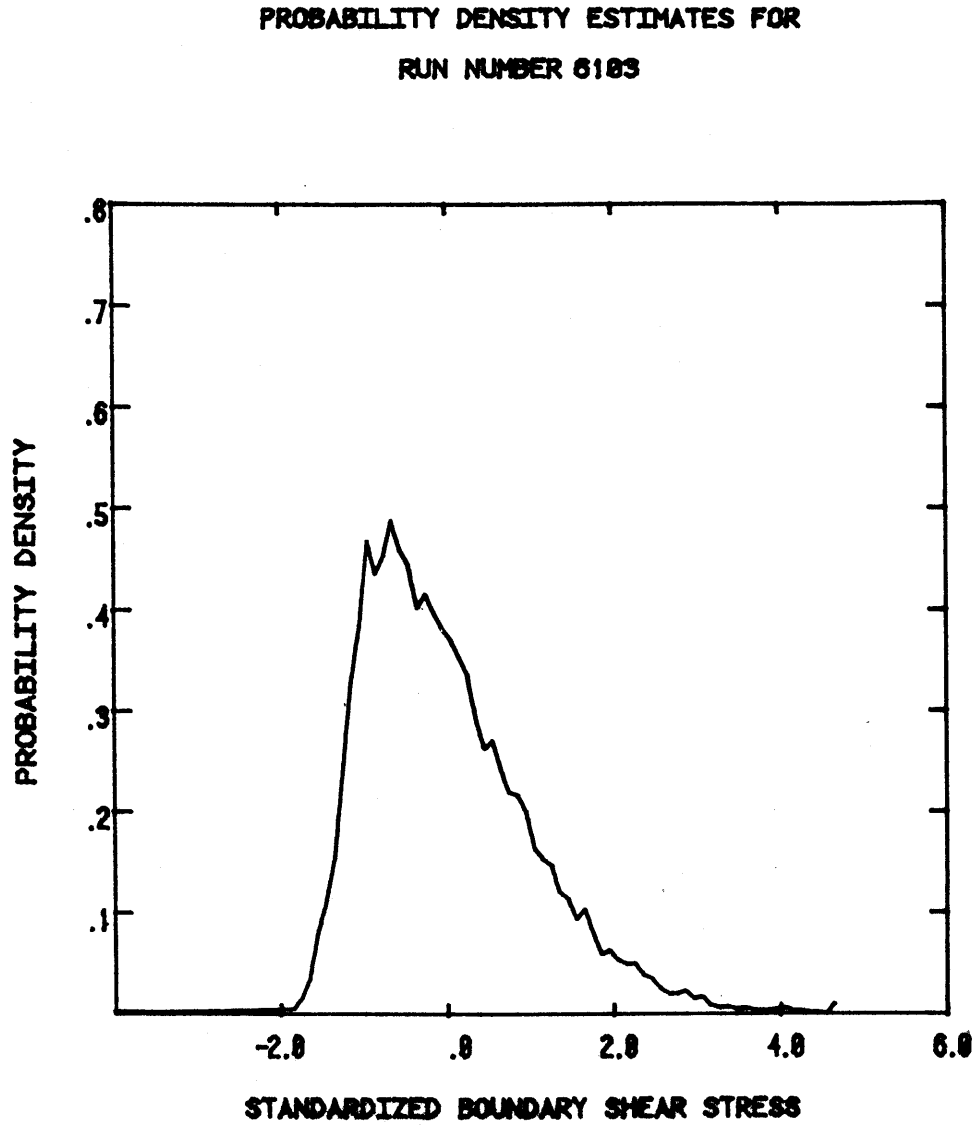

Figure 6-17. PDF estimate at 0.6 (y/h) on channel side for 2832 cm^3/s and 0.006 bed slope.

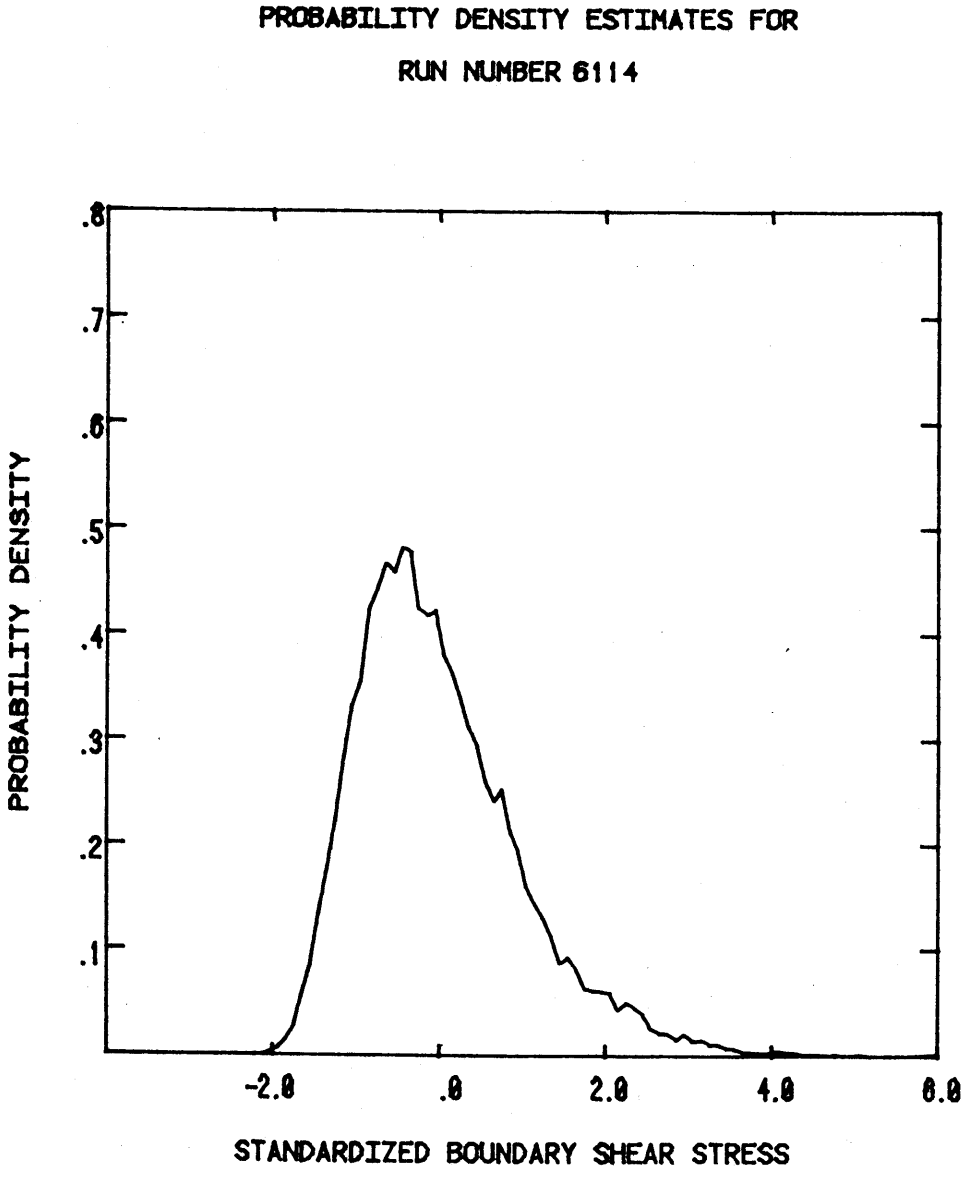

Figure 6-18. PDF estimate at 0.6 (y/h) on channel side for 14158 cm^3/s and 0.003 bed slope.

Similar to the results of Wylie et al. (19) the skewness and kurtosis (third and fourth moments) showed quasi-periodic variations across the channel. The kurtosis defines the "peakedness" of a distribution and is equal to 3 for a normal distribution. The experimental kurtosis data was consistently greater than 3 and the kurtosis on the side was consistently greater than the kurtosis on the bottom.

6.7 Friction Factor Results

The variation of the Darcy friction coefficient f with Reynolds number was investigated based on the experimental data. The shear velocity, u_*, is defined as

$$u_* = \sqrt{\frac{\tau_o}{\rho}} \tag{6-3}$$

where τ_o is the bed shear stress and ρ is the fluid density. From the assumption that $\tau_o = \gamma R S_f$, where R is the hydraulic radius and S_f is the energy slope, then

$$u_* = \sqrt{gRS_f} \quad . \tag{6-4}$$

Combining Equation (6-4) with the Chezy equation

$$u = C\sqrt{RS} \tag{6-5}$$

where C is a dimensionless number yields

$$\frac{U}{u_*} = \frac{c}{\sqrt{g}} = \sqrt{\frac{8}{f}} \quad . \tag{6-6}$$

Solving Equation (6-6) for the friction factor f

$$f = \frac{8\tau_o}{U^2\rho} \quad . \tag{6-7}$$

The theoretical relation for f is

$$f = \frac{0.316}{R_e^{1/4}} \tag{6-8}$$

for Reynolds numbers less than 10^5. Using the value of shear stress from γRS_o and the mean velocity as determined by the continuity law, the experimental friction factors were compared to the theoretical values. Figure 6-19 illustrates the results and indicates that the general trend of the experimental data follows the theoretical curve.

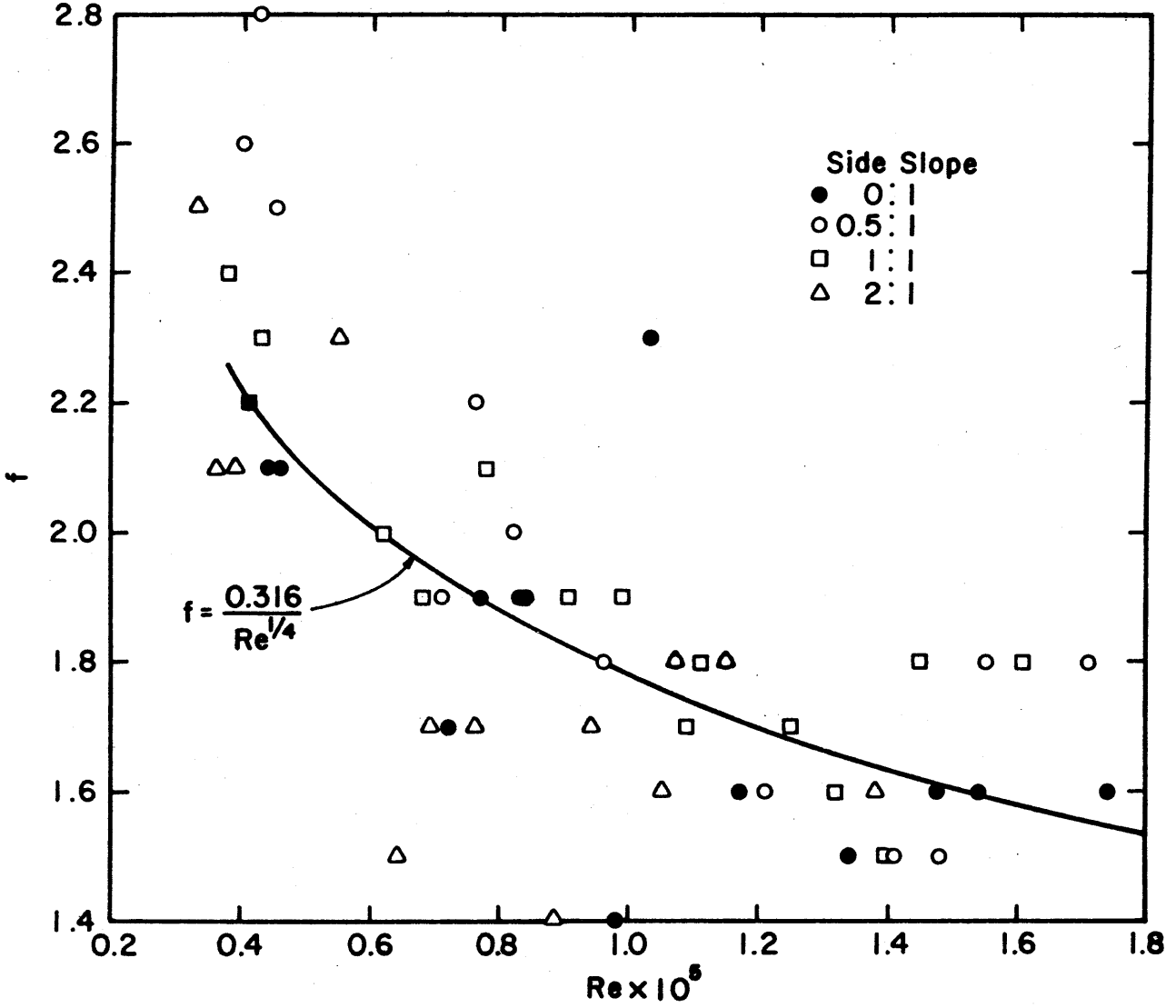

Figure 6-19. Experimental and theoretical friction factor variation with Reynolds number.

VII. BOUNDARY SHEAR STRESS RESULTS FOR NONUNIFORM FLOW

7.1 General

Nonuniform flow is a hydraulic condition where the flow depth, cross-sectional area and mean velocity vary from point to point. The tractive force equation derived in Chapter II (Equation (2-20)) gives the theoretical boundary shear stress when the slope is defined properly. In nonuniform flow the energy slope must be utilized to obtain the true boundary shear stress. To verify this experimentally measurements were taken in the backwater region created by a sharp crested weir. Using standard backwater calculations the shear stress distribution in the streamwise direction was determined. The values measured by hot-film anemometry techniques were found to agree with the calculated values.

7.2 Experimental Conditions

A sharp crested weir made of plexiglas with a height of 2.5 inches was mounted in the 1:1 side slope trapezoidal channel. The weir was located 5 feet from the downstream end of the flume. Boundary shear stress measuring locations were fixed on the centerline of the flume at 3-foot intervals upstream of the weir. In addition, a single measuring location was positioned 0.5 feet upstream of the weir as an initial point for the analytical calculations. A definition sketch of the weir and measuring locations is shown in Figure 7-1.

To avoid projecting the backwater surface into the headbox of the flume the bed slope was maintained supercritical. In this manner the flow was forced through a hydraulic jump several feet downstream of the headbox. Because the Froude number difference upstream and downstream of the jump was not large, the jump appeared only as a wavy unstable

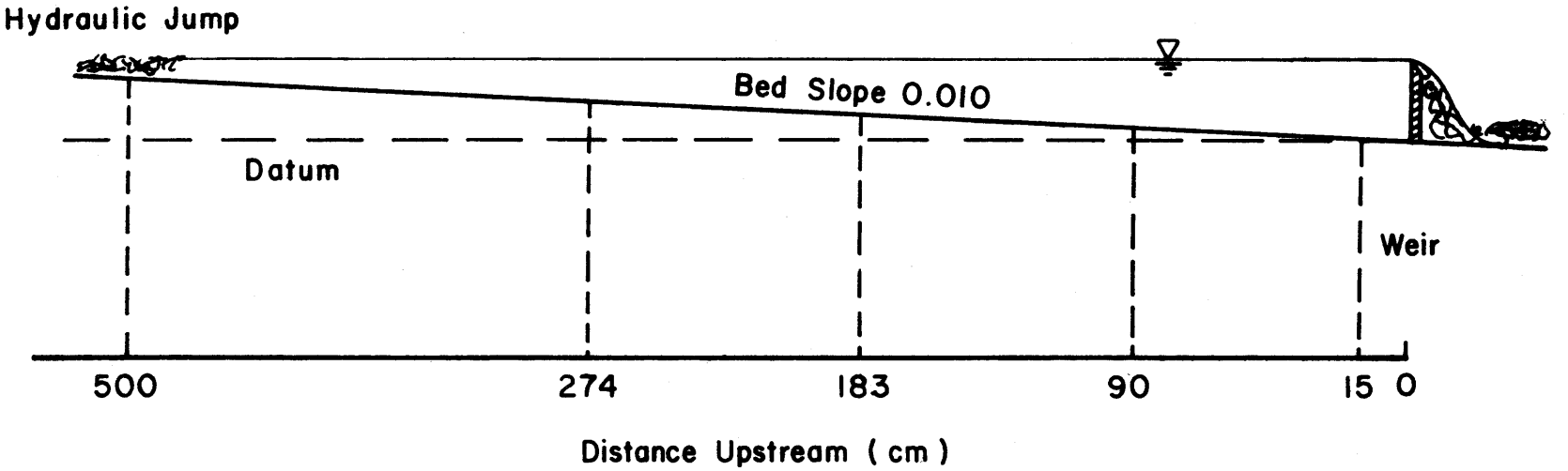

Figure 7-1. Definition sketch of wier and measuring locations.

water surface. The transition region occurred approximately 15 feet upstream of the weir. Table 7-1 summarizes the flow conditions.

Table 7-1. Hydraulic conditions for nonuniform flow experiments.

Q (cm^3/s)	Bed Slope	Critical Depth (cm)	Critical Slope	Slope Classification
3228	0.010	2.81	0.002	Steep
3710	0.010	3.07	0.002	Steep
4163	0.010	3.30	0.002	Steep
4559	0.010	3.50	0.002	Steep
4927	0.010	3.67	0.002	Steep
5267	0.010	3.83	0.002	Steep
5578	0.010	3.97	0.002	Steep
5890	0.010	4.11	0.002	Steep
6173	0.010	4.23	0.002	Steep

7.3 Analytical Computations

The standard step method was used for the backwater calculations. This method was chosen because it allows the use of fixed distances along the channel at which the depth is computed. Integration of the equation of motion (Equation (2-32)) is based on a discrete numerical approximation. Water surface profile determination is a trial and error procedure that involves matching the total heads calculated by 1) consideration of water surface elevation and velocity head at a given station, and 2) consideration of total head at the last station and intervening head loss between stations.

By equating the total energy at the stations on a channel, conservation of energy implies

$$z_{i-1} + \alpha_{i-1} V_{i-1}^2/(2g) = z_i + \alpha_i V_i^2/(2g) + h_f + h_e \qquad (7\text{-}1)$$

where z is the elevation of the water surface, α is the kinetic energy correction factor, V is the average velocity of flow, g is the gravitational acceleration, h_f is the friction loss and h_e is the eddy loss. The subscripts refer to successive stations along the channel where i is downstream of $i-1$. The friction loss, h_f, is

$$h_f = S_f \Delta L = \Delta L \, (S_{f_i} + S_{f_{i-1}})/2 \qquad (7\text{-}2)$$

where S_f is the average of the slopes of the energy grade line at the two sections and ΔL is the length of channel between the two sections. The friction slope in gradually varied flow is

$$S_f = n^2 V^2/[(1.49)^2 R^{4/3}] \qquad (7\text{-}3)$$

For a smooth plexiglas channel the Manning n is 0.008 (24). The value of head loss due to eddy formation is considered negligible in prismatic channels. Since the total energy head H is

$$H = z + \alpha V^2/(2g) \qquad (7\text{-}4)$$

Equation (7-1) can be expressed as

$$H_1 = H_2 + h_f \quad . \qquad (7\text{-}5)$$

The iterative solution involved matching the total energy head from Equation (7-4) and the value from Equation (7-5). A Hewlett-Packard Model 97 desk top calculator was used to perform the calculations with a prewritten program (25). For each location the shear stress was computed using Equation (2-20) with the values of depth and energy slope from the backwater calculation. The depth was used instead of hydraulic radius because point rather than mean values were desired.

7.4 Results

For all flow conditions tested the measured and calculated values of boundary shear stress near the weir showed excellent agreement. However, the measured values further upstream of the weir showed considerable deviation from the calculated values. In general, the deviation became greater with higher discharge. Graphs of Figure 7-2 illustrate the measured and calculated boundary shear stress for each flow condition at four locations. The gradual increasing trend of the measured value over the calculated value is apparent.

One explanation for the higher measured shear stress could be the influence of the hydraulic jump. Near the jump the pressure distribution is not hydrostatic, as assumed by the theory used in calculating backwater profiles. The hydrostatic assumption results from taking the derivative of the Bernoulli equation (Equation 2-30)) in the development of the governing equations for nonuniform flow. This would also explain the greater deviation with increasing discharge since at higher discharge the influence of the hydraulic jump propagated further downstream. Typically, the jump occurred in the range of 450 to 600 cm upstream of the weir. The surface instability associated with the hydraulic jump was still quite apparent at the location 274 cm upstream of the weir. This location was the measuring position farthest from the weir and consistently showed the greatest deviation from the calculated value.

Based on these measurements the use of backwater calculations to evaluate the longitudinal shear stress is acceptable, providing hydrostatic pressure distribution is maintained. The small trapezoidal channel used in this investigation only allowed consideration of relatively short backwater profiles, and the influence of the hydraulic

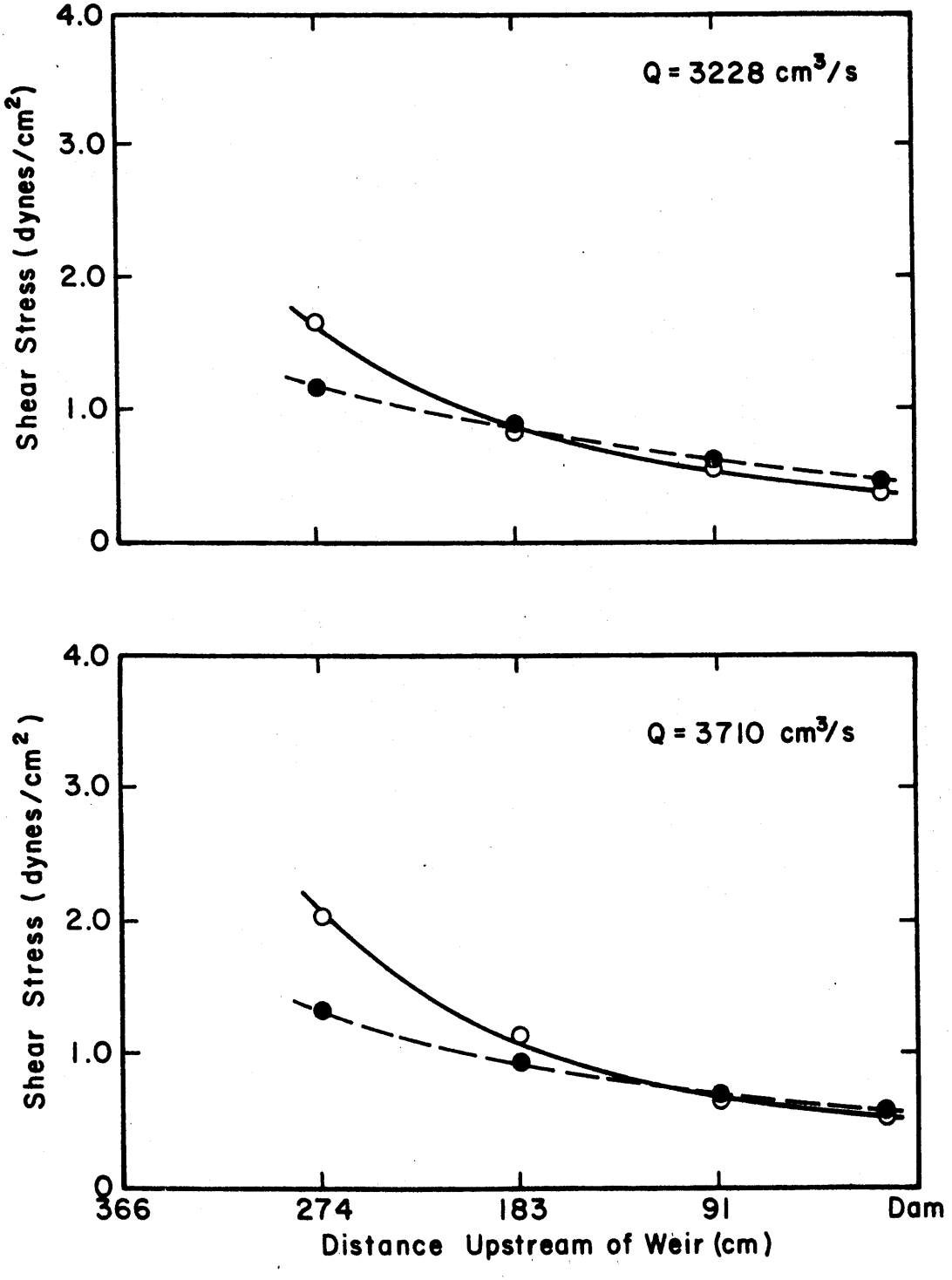

Figure 7-2. Measured shear stress (solid line) and calculated shear stress (dotted line) as a function of location.

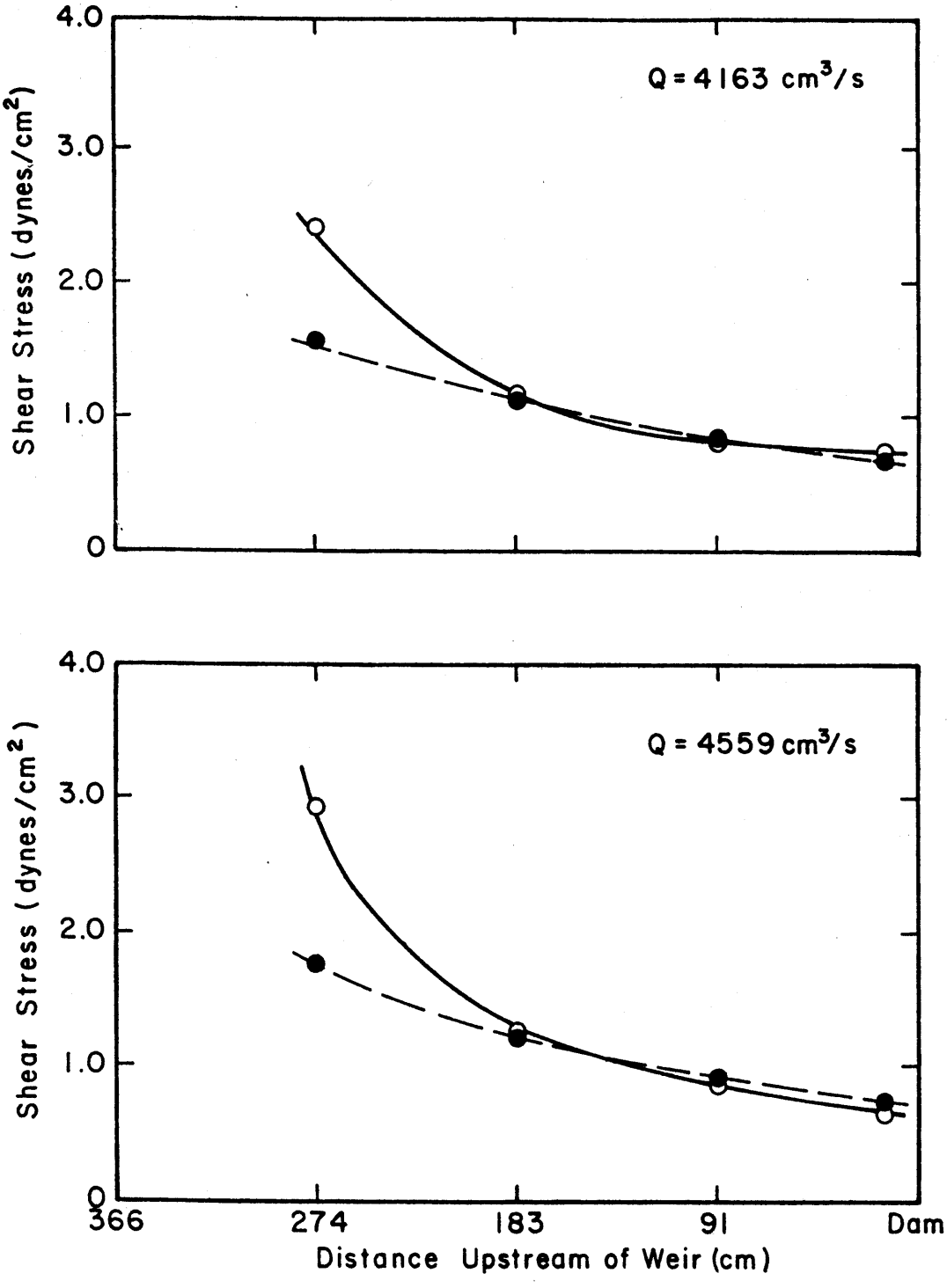

Figure 7-2 (continued)

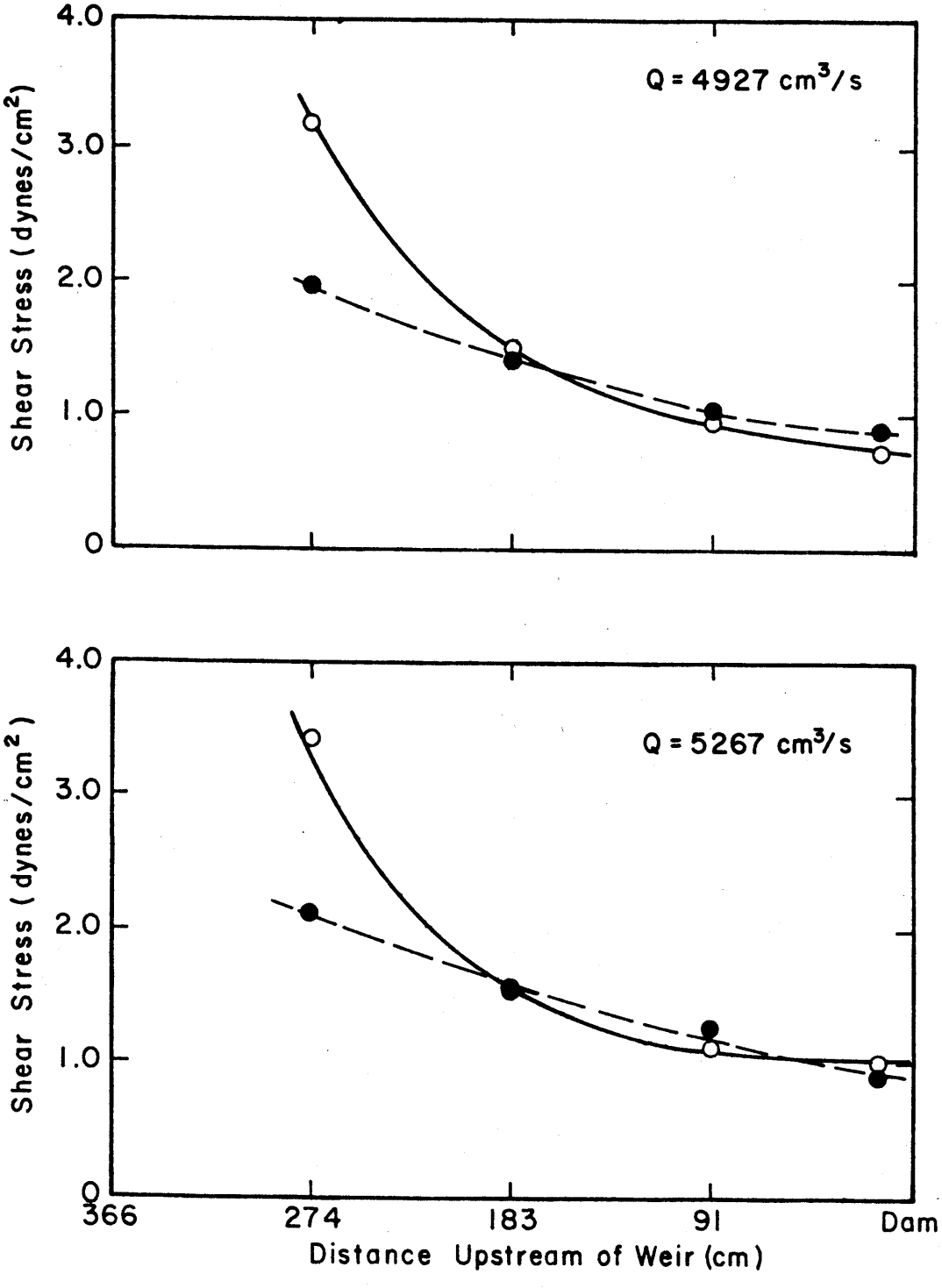

Figure 7-2 (continued)

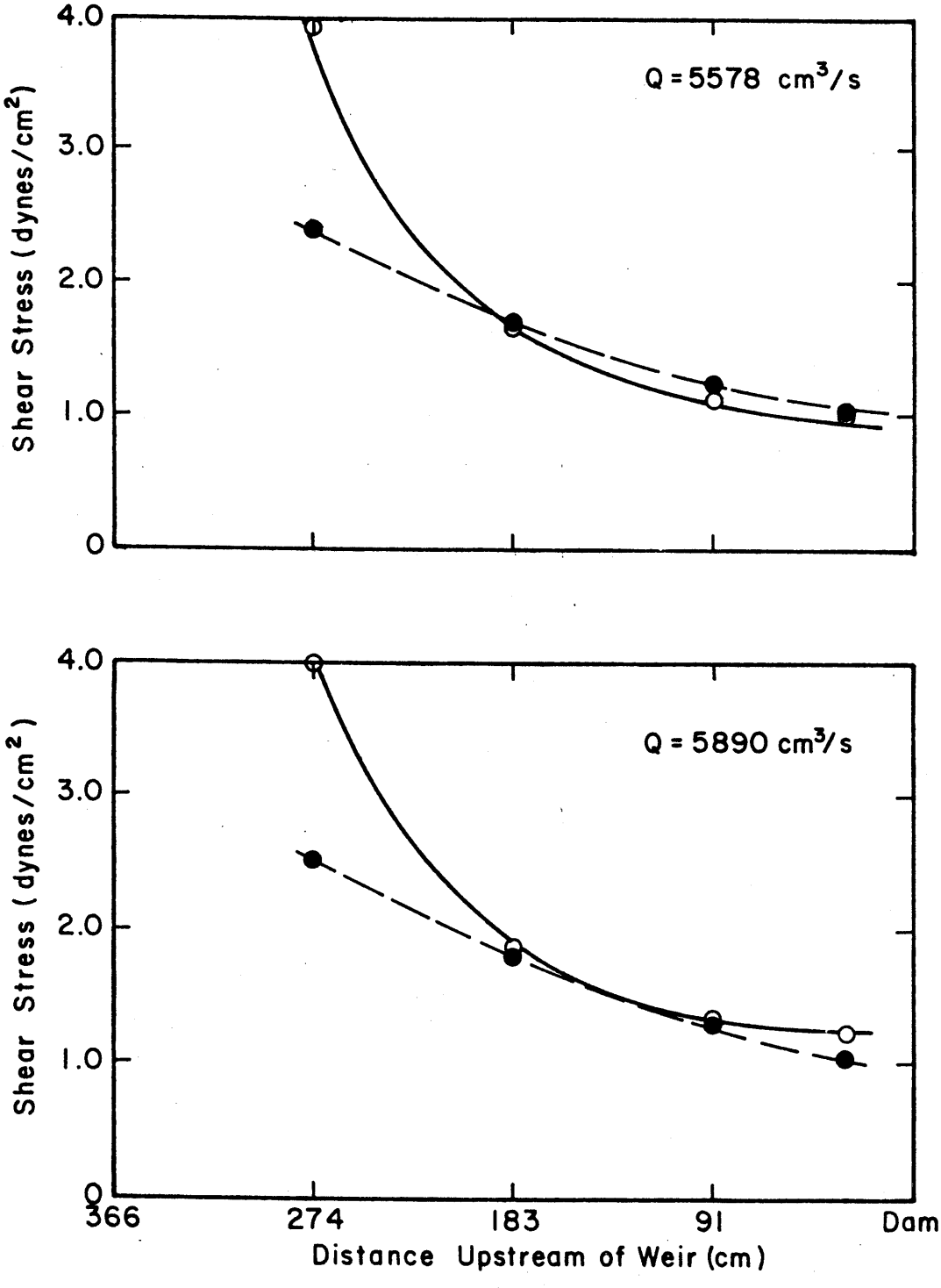

Figure 7-2 (continued)

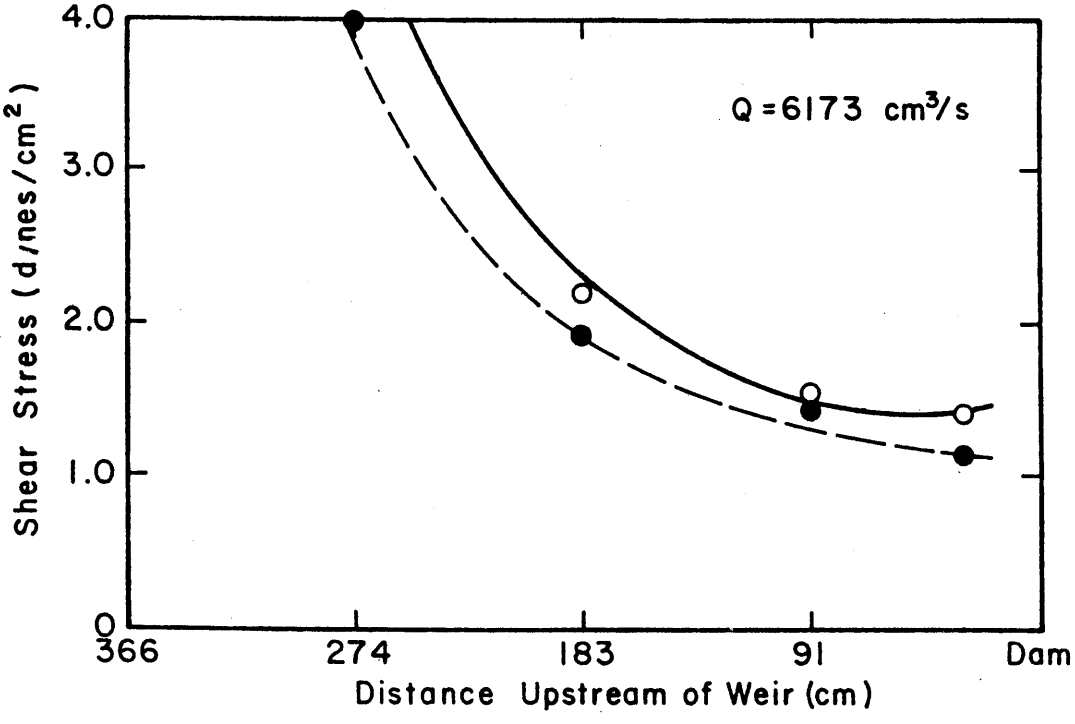

Figure 7-2 (continued)

jump was significant. For larger channels or natural rivers it is anticipated that hydrostatic pressure would be maintained over a greater percentage of the backwater profile length.

VIII. TURBULENT VELOCITY FLUCTUATION CHARACTERISTICS

8.1 General

Knowledge of the characteristics of turbulence is an important factor in many design and research projects in the fields of hydraulic, sanitary and chemical engineering. Turbulence affects the processes of sediment transport, incipient motion and solid particle settlement and is important in the design of hydraulically stable channels. Accurate prediction of diffusion and dispersion of pollutants in sanitary and chemical engineering requires knowledge of the turbulence intensities. It is generally accepted that almost all flows that are of interest to the engineer are turbulent. Previously, turbulence characteristics were obtained postori from empirical regression equation analysis of experimental data. Equations derived in this manner are generally applicable only under a given set of conditions. Clearly, an analytical approach that is not limited in application would be valuable.

Due to the random nature of turbulence, a probabilistic approach to the problem is required. A gaussian distribution is assumed to describe the turbulent fluctuating velocities, and from this basic condition a three parameter model is derived predicting the root-mean-square (RMS) values of turbulence for the vertical and longitudinal directions.

Coefficients in the model were calibrated using a wide range of data from smooth and rough boundary channels. Model prediction of the longitudinal and vertical RMS values were compared to limited experimental data and good agreement existed.

8.2 Formulation of the RMS Model

In addition to the assumption of a gaussian distribution to represent the turbulent fluctuating velocities, further assumptions on the characteristics of flow are necessary to simplify the model:

1. The flow is steady and uniform in the ordinary sense, i.e., over a time period,
2. The fluctuating velocity in the streamwise direction is the result of momentum transfer only in the cross-streamwise (y) direction. The influence in the transverse (z) direction is neglected,
3. The mean flow velocity in the y direction is zero across the entire flow depth, and
4. The expected magnitude of the cross-stream fluctuating velocity is proportional to that of the streamwise fluctuating velocity (26),

i.e., $$E[|V_i|] = cE[|U_i|] \qquad (8\text{-}1)$$

in which $E[\cdot]$ is the expected magnitude of the absolute values of cross-stream and streamwise fluctuating flow velocities, respectively, and c is a constant. This assumption is essentially that used by Prandtl in his well-known mixing length theory. The streamwise and cross-streamwise velocities are defined as $u_i = U_i + \bar{u}_i$ and $v_i = V_i + \bar{v}_i$ in which $\bar{u}_i$ and $\bar{v}_i$ are point mean flow velocities in the streamwise and cross-streamwise direction.

From the basic assumption of a normal distribution for the fluctuating velocities, the probability density function (PDF) of the two random variables, cross-streamwise fluctuating velocity and streamwise fluctuating velocity, are (27)

$$f_{V_{i(v)}} = \frac{1}{\sqrt{2\pi}\, v_i'} \exp\left[-\frac{1}{2}\left(\frac{v}{v_i'}\right)^2\right] I_{(-\infty,\ \infty)}(v) \qquad (8\text{-}2)$$

and

$$f_{U_{i(u)}} = \frac{1}{\sqrt{2\pi}\, u_i'} \exp\left[-\frac{1}{2}\left(\frac{u}{u_i'}\right)^2\right] I_{(-\infty,\ \infty)}(u) \qquad (8\text{-}3)$$

in which $\exp[\cdot] = e^{[\cdot]}$; $f(\cdot)$ is the probability density function; u_i' and v_i' is the root-mean-squares of the streamwise and cross-stream fluctuating velocities, respectively, and $I(\cdot)$ is the indicator function.

From Equations (8-2) and (8-3) the PDF of $|U_i|$ and $|V_i|$ can be obtained and the expected values of the fluctuating components shown to be:

$$E[|V_i|] = \sqrt{\frac{2}{\pi}}\ v_i' \qquad (8\text{-}4)$$

and

$$E[|U_i|] = \sqrt{\frac{2}{\pi}}\ u_i' \quad . \qquad (8\text{-}5)$$

Comparing Equations (8-1), (8-4) and (8-5), the equation

$$v_i' = c\, u_i' \qquad (8\text{-}6)$$

can be derived. The constant c is the first parameter of the model that will allow prediction of v_i' knowing u_i'. McQuivey and Richardson (28) reported that c is approximately 0.5 for a rough boundary and 0.7 for a smooth boundary, based on experimental data.

Determination of u_i' must then be made. By considering the special case of turbulent open channel flow, for which the viscous and dynamic forces have reached a statistically stable state, simplifications are

possible. The time average Navier-Stokes equation of motion for the x-direction gives the covariance of U_i and V_i as

$$E[U_iV_i] = \nu \frac{d\bar{u}_i}{dy_i} - u_*^2 \left(1 - \frac{y_i}{h}\right) \tag{8-7}$$

in which h is flow depth, y_i is the coordinate of vertical position, ν is kinematic viscosity, $\bar{u}_i$ is point mean flow velocity, and u_* is the shear velocity referring to the shear stress at the channel bottom. To correlate the point mean velocity $\bar{u}_i$ with the distance above the channel bed y_i requires a velocity distribution equation. The logarithm velocity profile is frequently used to describe the velocity distribution in turbulent open-channel flows and is adopted in this study. The relation is assumed as follows:

$$\bar{u}_i = \frac{u_*}{\kappa} \left(\ln \frac{y_i}{h} + 1\right) + u_0 \tag{8-8}$$

in which u_0 is the average velocity of flow (the ratio of the unit-width discharge to the total flow depth) and κ is the von Karman universal constant. The value of κ is assumed to be 0.4 for all computations in this paper. From Equations (8-7) and (8-8) the covariance of U_i and V_i can be expressed as

$$E[V_iU_i] = \nu \frac{u_*}{\kappa y_i} - u_*^2 \left(1 - \frac{y_i}{h}\right) \quad . \tag{8-9}$$

By definition, the correlation coefficient ρ of U_i and V_i is

$$\rho = \frac{E[U_iV_i]}{\sqrt{Var[U_i]\ Var[V_i]}} = \frac{E[U_iV_i]}{u_i' v_i'} = \frac{E[U_iV_i]}{cu_i'^2} \tag{8-10}$$

in which $Var[\ ]$ is the variance of the random variable.

Rearranging Equation (8-10) gives

$$u_i' = \sqrt{\frac{E[U_i V_i]}{c\rho}} \tag{8-11}$$

in which $E[U_i V_i]$ is defined in Equation (8-7).

The value of ρ as reported by McQuivey and Richardson (28), Laufer (29) and Rechardt (30) indicate that up to some distance above the bed y_*, ρ is constant. Beyond y_* the correlation value decreases and drops to zero at the free surface. Therefore,

$$\rho = r \text{ for } 0 < \frac{y_i}{h} \leq y_*$$

and

$$\rho = Kr\left[1 - \frac{y_i}{h}\right] \text{ for } y_* < \frac{y_i}{h} \leq 1.0 \tag{8-12}$$

in which $K = \frac{1}{1-y_*}$ and y_* is the reference depth above the bed. McQuivey and Richardson (28) reported values of r equal to -0.7 and -0.4 for flow over rough and smooth boundaries, respectively.

8.3 Verification of the Normal Distribution Assumption for Fluctuating Velocities

Verification of the RMS model required measured data of the longitudinal and vertical components of velocity. Hot-film anemometry techniques are commonly used to obtain turbulence characteristics; however, most of the data currently available is of the longitudinal component only.

To measure the two velocity components a Thermo-Systems, Inc. (TSI) Model 1287W two-dimensional split-film probe was used with a TSI Model 1053B four-channel anemometer. Measurements were taken in the 1:1 side

slope trapezoidal channel. Subcritical and supercritical flow conditions with width-depth ratios less than 10 were measured.

Data collection and probability density analysis was done interactively with the HP-1000 computer. For one flow condition the PDF was computed at 0.1 to 0.9 relative depths. Typical results (relative depth 0.4) are summarized graphically in Figures 8-1 and 8-2. Table 8-1 shows the first four moments and the goodness of fit test results. The longitudinal velocity, longitudinal component and vertical component are indicated by CN, CU and CV, respectively. The first digit of the experiment number indicates the relative depth location. It is apparent that the fluctuating components of velocity follow a normal distribution, although the longitudinal component was consistently skewed slightly to the left.

8.4 Calibration of the RMS Model

A direct search method was used to obtain the best values for the parameters. The Cyber 172 computer at Colorado State University was used for all computations. In order to determine the best combination, an error calculation was necessary.

As an estimate of the error, the absolute value of the difference between the calculated and measured values for each y_i/h was computed, i.e.,

$$D_i = |u'_{ic} - u'_{im}| \tag{8-13}$$

in which u'_{ic} is the calculated turbulent intensity (RMS) and u'_{im} is measured turbulent intensity for the y ith location.

For each flume experiment, the average error over the entire flow depth h was computed as

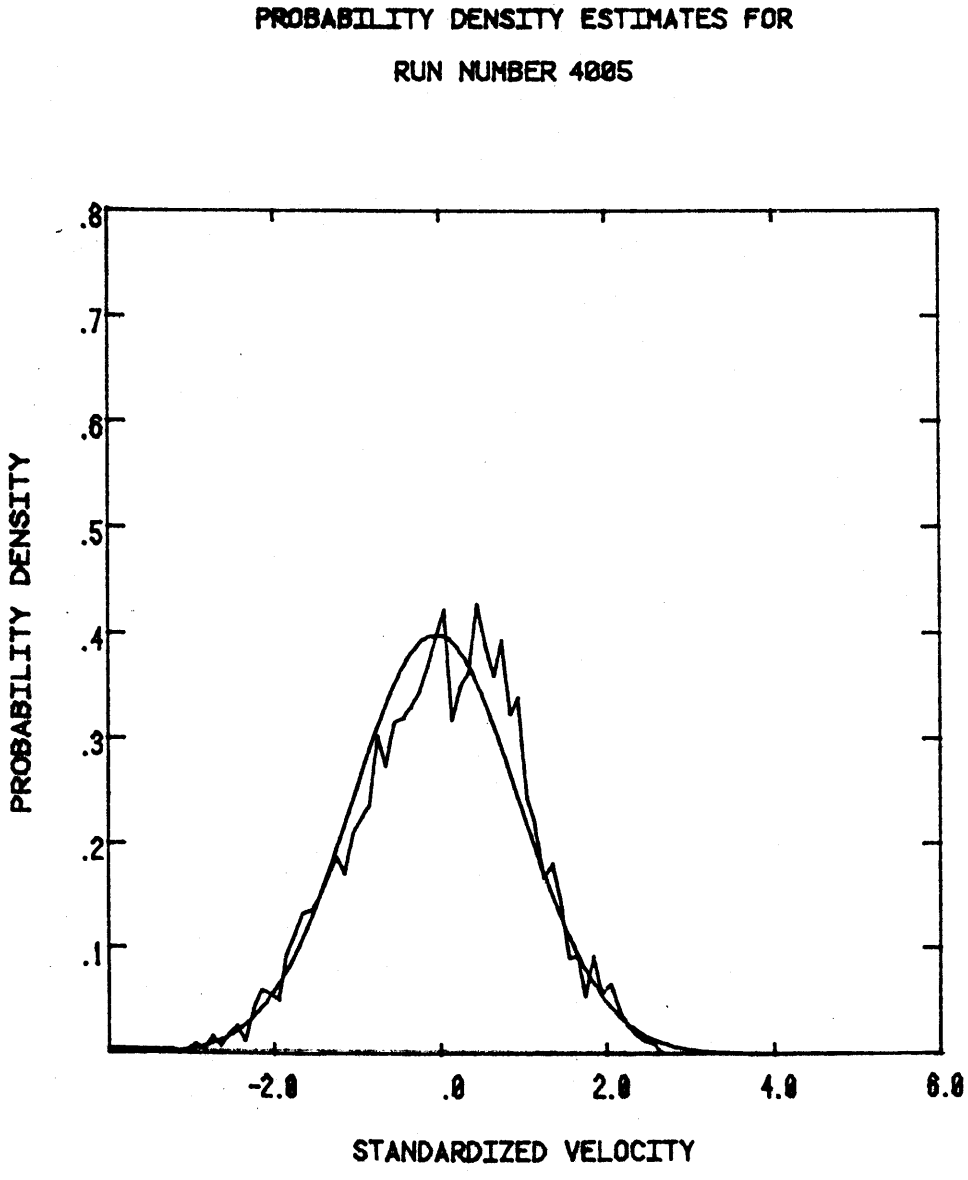

Figure 8-1. PDF estimate for longitudinal component at relative depth 0.4.

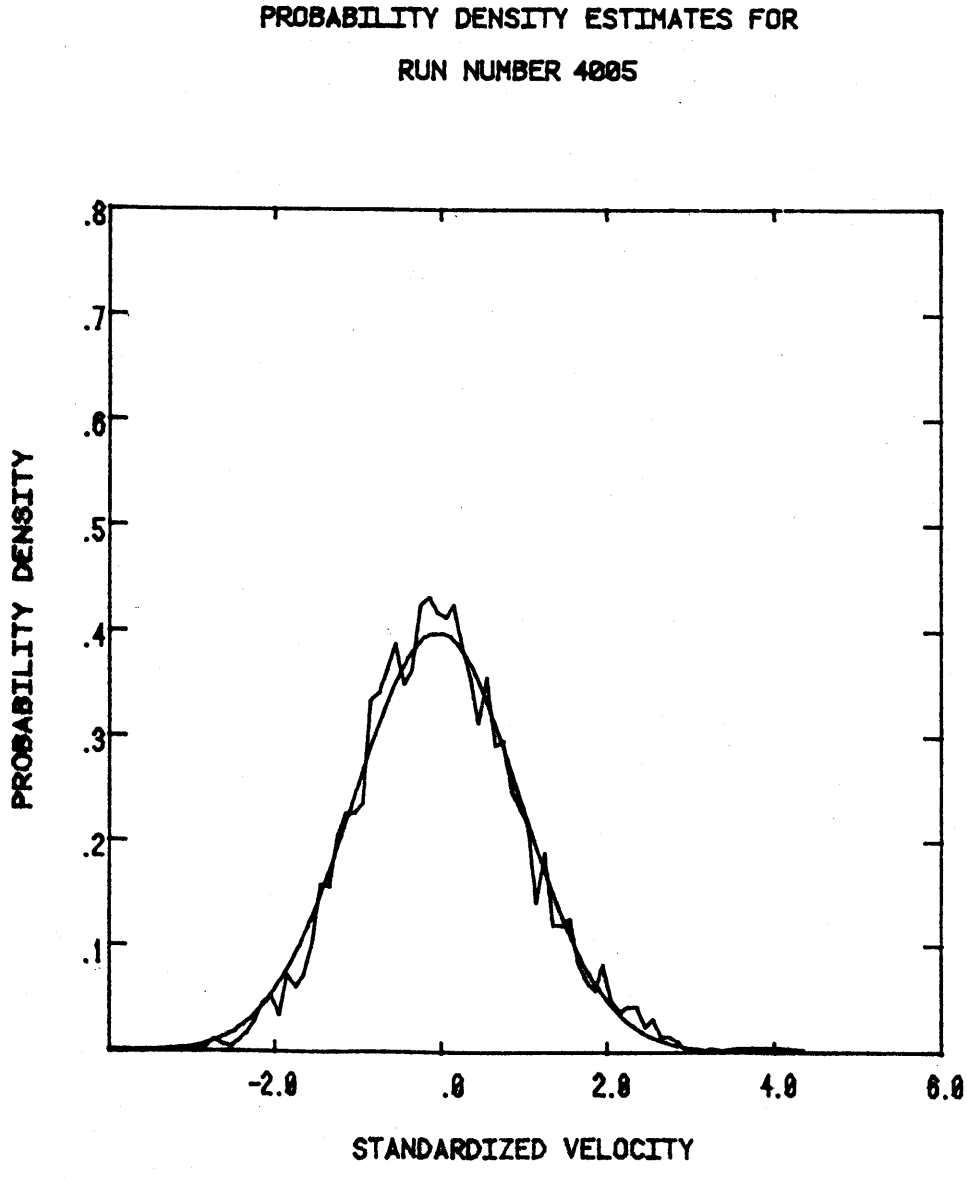

Figure 8-2. PDF estimate for vertical component at relative depth 0.4.

Table 8-1. PDF results for split-film data.

PDF ANALYSIS
Q = 0.2 cfs Slope = 0.003

Experiment Number	MEAN	RMS	SKEW	KUR	Normal CHI	Normal S-K	Log CHI	Log S-K
CN1005	36.77	4.390	-0.0037	2.6311	106	0.0243	157	0.0353
CU1005	36.72	4.402	-.0053	2.6356	106	0.0245	161	0.0358
CV1005	.11	1.800	0.4350	3.9288	159	0.0347	-	-
CN2005	41.70	3.918	-.3830	2.8666	240	0.0459	439	0.0613
CU2005	41.62	3.949	-.3798	2.8335	236	0.0435	448	0.0611
CV2005	1.65	1.840	0.2984	3.3504	95	0.0280	-	-
CN3005	44.45	3.509	-.2180	2.8539	108	0.0322	208	0.0493
CU3005	44.30	3.544	-.2468	2.8825	123	0.0368	209	0.0498
CV3005	3.24	1.761	0.3406	3.9407	91	0.0265	-	-
CN4005	46.96	3.461	-.2012	2.7746	97	0.0273	186	0.0371
CU4005	46.73	3.505	-.2147	2.7516	95	0.0302	176	0.0403
CV4005	4.33	1.697	0.2682	3.3725	84	0.0216	-	-
CN5005	47.60	3.134	-.3296	2.894	187	0.0357	324	0.0428
CU5005	47.35	3.178	-.3512	2.9138	213	0.0364	365	0.0428
CV5005	4.46	1.650	0.3209	3.544	99	0.0238	-	-
CN6005	49.64	2.617	-.1917	2.6828	125	0.0268	162	0.0327
CU6005	49.51	2.642	-.1983	2.7119	113	0.0280	143	0.0283
CV6005	3.25	1.579	0.4122	3.8406	138	0.0375	-	-
CN7005	51.74	2.150	-.4239	3.1427	195	0.0259	293	0.0353
CU7005	51.46	2.173	-.4665	3.2018	245	0.0316	346	0.0392
CV7005	5.19	1.344	0.2385	3.2066	111	0.0171	411	0.0430
CN8005	51.71	2.207	-.1498	3.0005	84	0.0159	106	0.0179
CU8005	51.27	2.202	-.1167	3.0237	70	0.0138	92	0.0211
CV8005	6.60	1.308	0.1770	3.398	74	0.0194	230	0.0460
CN9005	52.82	2.159	-.1810	3.8327	176	0.0251	122	0.0168
CU9005	52.24	2.162	-.1330	2.8148	88	0.0157	108	0.0191
CV9005	7.66	1.308	0.2784	3.2041	80	0.0181	89	0.0219

$$\varepsilon = \Sigma D_i / N \tag{8-14}$$

in which N is the total number of the measurement depths, y_i. This error value was normalized with respect to the average measured RMS for each flume experiment as

$$\varepsilon_N = \frac{\varepsilon}{\frac{\Sigma u'_{im}}{N}} \quad . \tag{8-15}$$

Data selected for testing resulted from experiments using hot-film anemometry techniques at Colorado State University. The data, published in a United States Geological Survey open file report (31), consisted of 40 sets representing several flumes under many different flow conditions. The data were divided into smooth and rough boundary groups.

The hydrodynamically smooth boundaries were constructed of Lucite, stainless steel or fiberglass. The rough boundary in the 20 cm wide flume was constructed entirely of Lucite with a fixed bed of 3/4-inch rocks. The 2-foot wide flume used 1/2-inch high wooden blocks fixed to a floor of 0.25-inch stainless steel. A riverbed was simulated in the 4-foot wide flume with 1 1/2-inch roughness and 4- to 6-inch rocks placed at 6-to 8-inch intervals. There were 27 sets of rough boundary data and 13 sets of smooth boundary data. The two groups were analyzed independently and the total average error for each group was calculated as

$$TE_i = \frac{\Sigma \varepsilon_N}{NR} \tag{8-16}$$

in which NR is the number of records and $i = 1, 2$, representing smooth and rough data groups, respectively. The combination of c, r

and y_* producing the minimum TE were considered the best or most representative values.

For smooth boundary data, the initial calculations revealing $y_* = 0.8$ produced the smallest error for combinations of c and r. This value was then maintained in all further calculations and many more combinations of c and r were assumed. Over the range of $0.5 < c < 0.8$ and $-0.8 \leq r \leq -0.5$, six combinations were found to produce a minimum average total error (TE) of 21.5 percent. These values are presented in Table 8-2.

Table 8-2. Combinations of c and r producing minimum total error.

SMOOTH	c	0.50	0.55	0.60	0.65	0.75	0.80
TE-21.5%	r	-0.80	-0.75	-0.65	-0.60	-0.55	-0.50
ROUGH	c	0.55	0.70	-	-	-	-
TE-15.4%	r	-0.70	-0.55	-	-	-	-

For rough boundary data the optimum value of y_* for rough boundary conditions was found to be 0.6. Again by maintaining this value and considering many more combinations of c and r, only two combinations of c and r were found to produce a minimum average total error (TE) of 15.4 percent. These values are also presented in Table 8-2. The values compare favorably with the conclusion of McQuivey and Richardson (28).

The difference in the y_* value for the smooth and rough boundaries is logical considering what y_* actually represents. A higher magnitude of y_* indicates the turbulence is correlated for a longer distance away from the boundary. Correlation itself refers to the interdependence between two random variables. If the velocity fluctuations were completely random the correlation would be zero. The

importance of the near wall region, particularly the viscous sublayer, for defining the turbulent structure of the entire flow is revealed in the bursting theories that have been developed (32). Considering the effects of roughness in disrupting the viscous sublayer (and thus the entire flow pattern), it is logical to expect smooth boundary turbulence to remain correlated and less random for a longer distance from the wall.

The greater total error for smooth boundaries is explainable if one considers the implications of Assumption 4. This is the same assumption made in the mixing length theory. The mixing length concept was introduced by Prandtl in order to describe velocities in turbulent flows, assuming the fluctuations are confined to a certain limit defined by a mixing length ℓ (24).

Since the mixing length and the concept of proportional fluctuating velocities apply to turbulent flow, it is logical to expect the theory to be more realistic for highly turbulent flows. The flow over a rough boundary is generally more turbulent than flow over a smooth boundary and as Assumption 4 is more rigorously maintained for the rough boundaries, produces better results.

The most surprising result is the possibility of converging c and r into one constant set of parameters for both smooth and rough boundaries with a very negligible effect on total error. By assuming $c = 0.55$ and $r = -0.7$, the value of the total error for smooth boundaries increased only 1.0 percent from 21.5 percent error using optimum parameters. For rough boundaries no change was observed using the appropriate values of y_*. Making this change, the model has essentially become a one parameter (y_*) description of turbulent intensities, with

the single parameter assuming only one of two values, depending on the boundary condition.

8.5 Calculation Procedure

The calculations involved in analytically determining the turbulent intensities by this model are simple and direct. Only three computations are required to predict the streamwise and cross-streamwise RMS values once the boundary condition has been determined. The procedure is as follows:

1. Calculate $E[U_iV_i] = \nu \frac{u_*}{\kappa y_i} - u_*^2 \left(1 - \frac{y_i}{h}\right)$ (Equation (8-9)) for a given y_i/h.
2. Calculate $u_i' = \sqrt{\frac{E[U_iV_i]}{c\rho}}$ (Equation (8-11)) with $c = 0.55$ and ρ as defined by Equation (8-12) with y_* set according to the boundary condition.
3. Calculate $v_i' = cu_i'$ (Equation (8-6)).

8.6 Results

The model prediction of RMS was compared with two sources of experimental data to evaluate its performance. The experimental data of McQuivey (31) in smooth and boundary rectangular channels was used to evaluate the longitudinal RMS prediction. The split-film data taken by the author was used to evaluate both the longitudinal and vertical RMS prediction in a smooth boundary trapezoidal channel. The graphs in Figure 8-3 show the overall results for McQuivey's data (31) and for the split-film data, respectively. Ten percent error bands are drawn to show the accuracy of prediction. It should be stressed that the results shown in Figure 8-3(b) are predicted values that directly utilize the parameters calibrated from McQuivey's data (31).

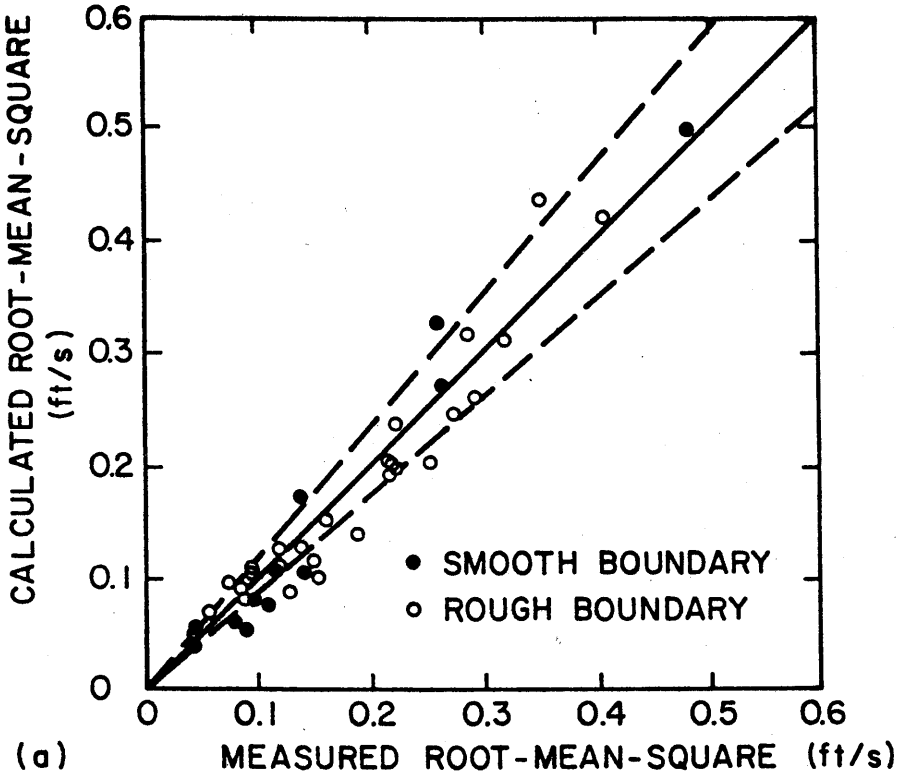

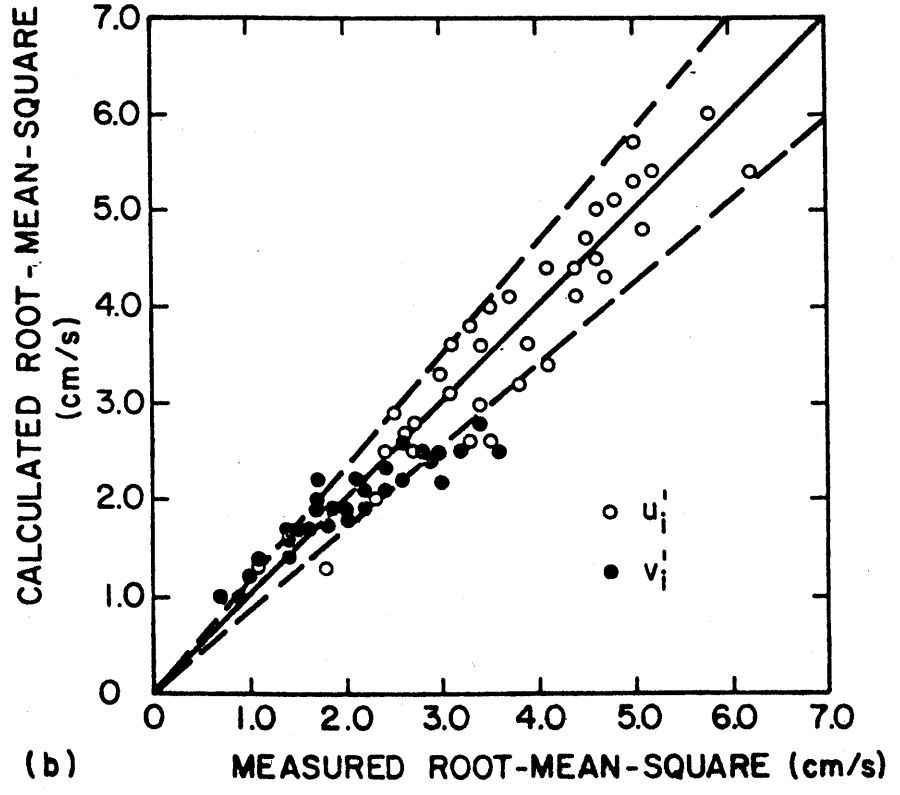

Figure 8-3. Comparison of calculated to measured root-mean-square (a) McQuivey's data, and (b) author's data.

Figure 8-4 shows the relation of measured and calculated turbulent intensity to relative depth. This representative sampling over a range of flumes indicates that the model makes best predictions by y_i/h greater than 0.15. Figure 8-5 shows both the calculated and measured values for both components of RMS against flow depth. Excellent model prediction was obtained over a wide range of flow conditions for smooth or rough boundaries.

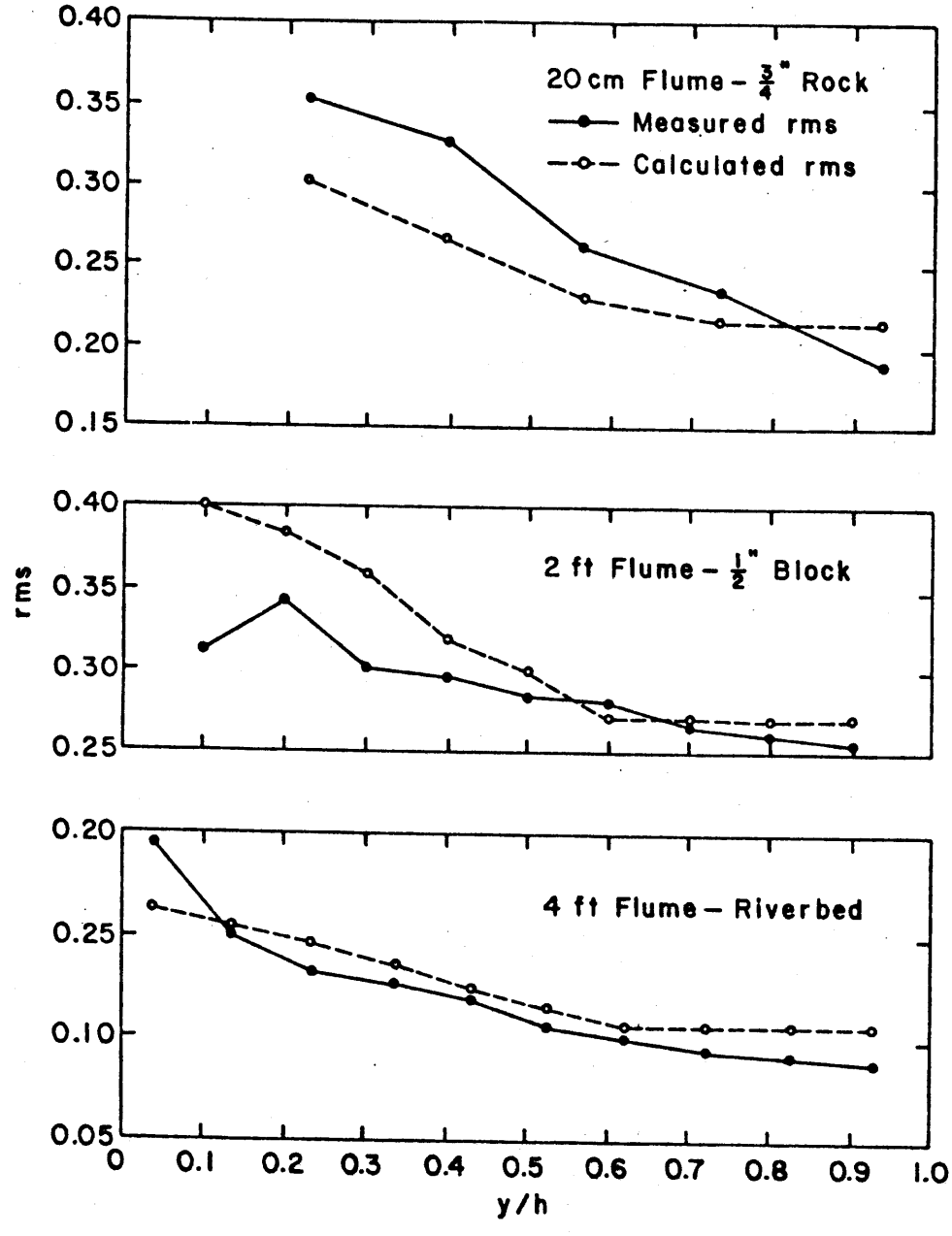

Figure 8-4. Relation of measured and calculated turbulent intensity (RMS) to relative depth.

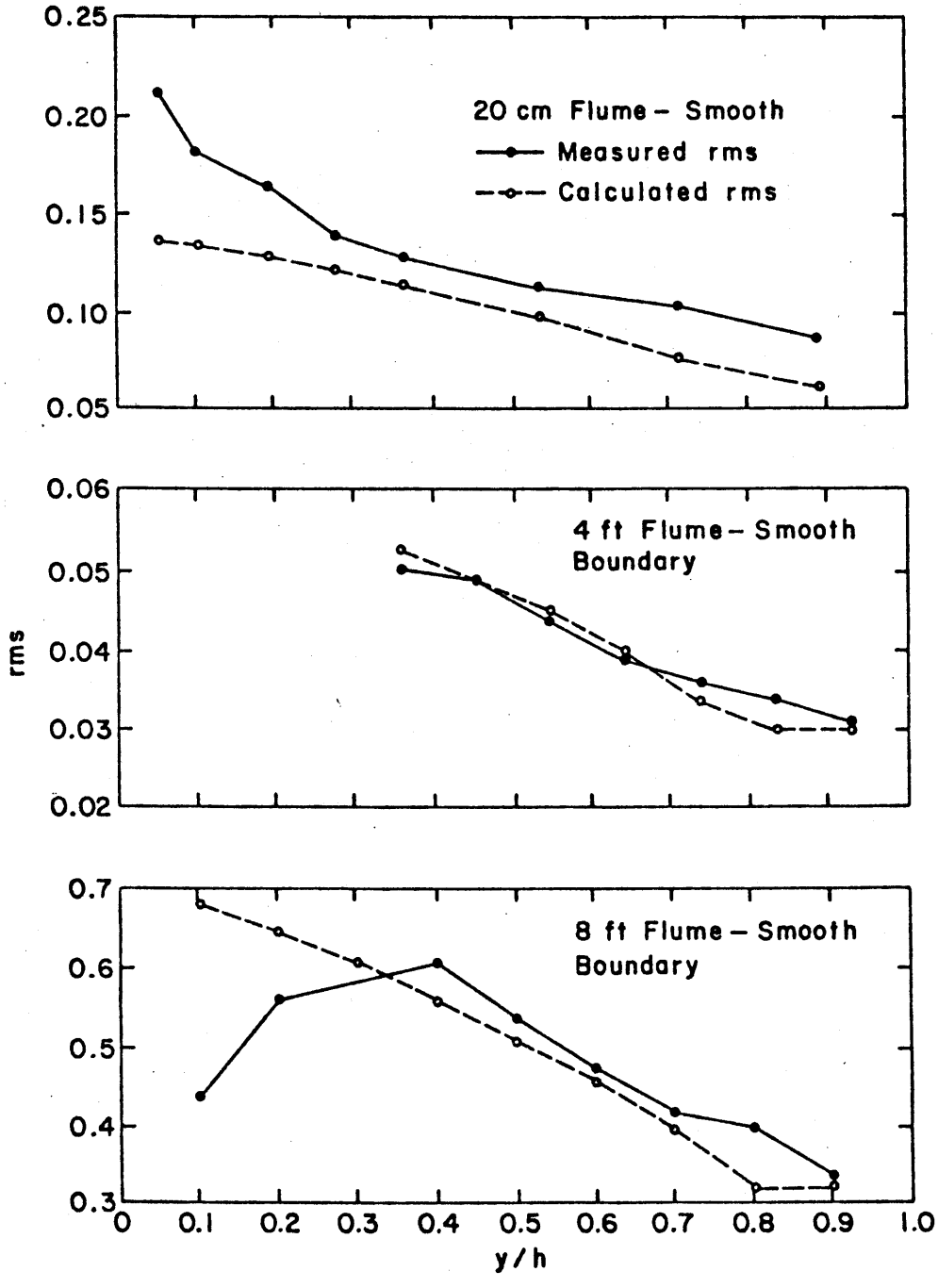

Figure 8-4 (continued)

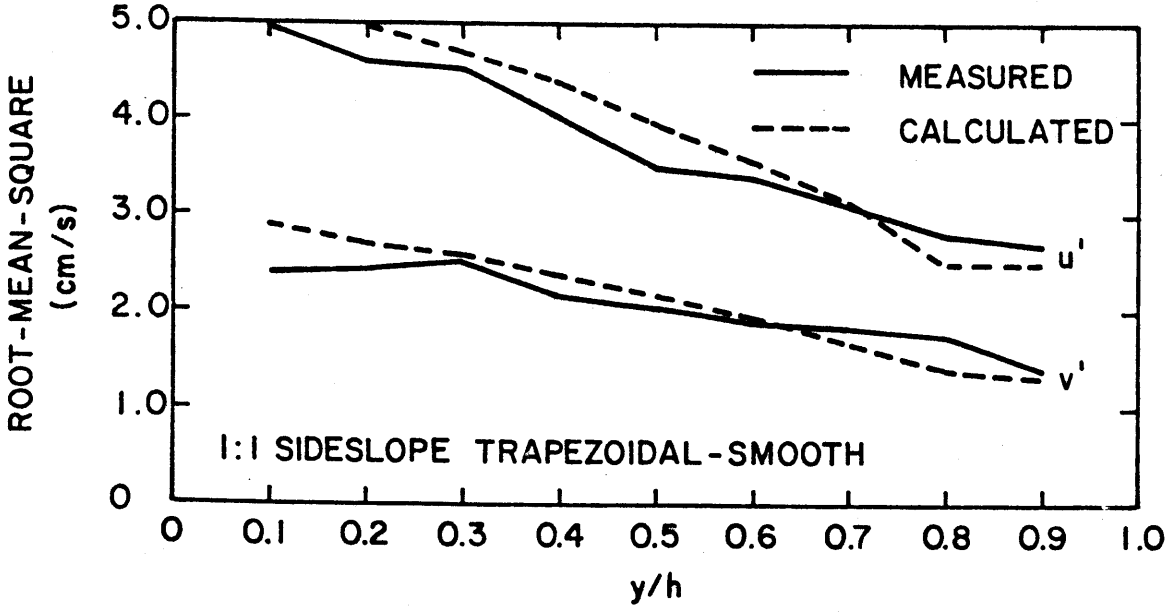

Figure 8-5. Relation of measured and calculated root-mean-square for both components to flow depth.

IX. CORRELATION ANALYSIS BETWEEN VELOCITY AND BOUNDARY SHEAR STRESS

9.1 General

Knowledge of the characteristics of velocity in open channel flow is essential for a complete understanding of turbulent boundary shear stress processes. The influence of turbulent velocity fluctuations on the shear flow structure, and thus on the turbulent wall shear stress, was qualitatively stated by Blinco (3). Additionally, the effect of secondary current circulation has been suggested to be significant in determining the spatial distribution of the boundary shear stress (18). To examine these possible relationships, simultaneous measurement of turbulent velocities and boundary shear stresses were conducted. The correlation of the near wall velocity to the boundary shear stress was evaluated and the influence of secondary current circulation on the boundary shear stress spatial distribution was investigated.

9.2 Experimental Conditions

Detailed measurement of the turbulent velocities near the wall boundaries was conducted using TSI Model 1218-20W boundary layer velocity probes. The small size of this sensor minimizes the effects of probe interference, and the unique design for boundary layer applications allows measurements very near the wall. The probe was calibrated in the facility described in Section 4.3.

Two basic experiments were conducted. The first series involved simultaneous measurement of velocity and boundary shear stress, and the evaluation of correlation coefficients. The capability of real time data acquisition and analysis with the Hewlett-Packard minicomputer (Appendix C) was a definite asset to these measurements. Additionally,

oscilloscope traces of the simultaneous velocity and boundary shear stress were photographed to qualitatively examine similarities in fluctuations. The second series involved evaluation of secondary currents through detailed velocity profile measurements. Compression or expansion of the isovels (lines of constant velocity) were qualitatively related to the existing boundary shear stress distribution.

9.3 Correlation Coefficient Results

Correlation coefficients between point velocity and boundary shear stress were evaluated as a function of relative depth. The correlation coefficient is defined as

$$\rho = \frac{\text{covar}}{(\text{var } U \cdot \text{var } \tau)^{1/2}}$$

where ρ is the correlation coefficient, var U is the variance of the velocity fluctuations and var τ is the variance of the boundary shear stress fluctuations. Nine flow conditions were evaluated for relative depths ranging from 0.01 to 0.8. The hydraulic flow conditions were numbers 1 to 9 identified by Table 6-2. Initial experimental work for nine flow conditions evaluated the correlation coefficient for relative depths 0.1 to 0.8. Based on these results, it was determined that investigation of the correlation of velocity fluctuation and boundary shear stress fluctuation nearer to the wall was necessary. A second set of data for three flow conditions considered the correlation coefficient relationship to relative depths ranging from 0.01 to 0.09. Table 9-1 summarizes the results.

Plates 9-1 and 9-2 illustrate typical oscilloscope traces and indicate a similarity in the occurrence of a fluctuation of boundary shear stress with a fluctuation in velocity. Figures 9-1 and 9-2 show

Table 9-1. Correlation coefficient results of velocity and boundary shear stress for different relative depth.

Run No.	$\overline{\tau}$ (dynes/cm^2)	τ_{RMS} (dynes/cm^2)	$\overline{U}$ (cm/s)	u_{RMS} (cm/s)	Correlation Coefficient
1101	6.718	1.503	25.83	2.790	0.325
2101	6.310	1.349	27.87	2.507	0.237
3101	6.497	1.572	27.68	2.226	0.292
4101	6.256	1.340	31.69	2.218	0.134
5101	6.220	1.319	32.42	2.052	0.201
6101	6.185	1.488	31.28	1.851	0.103
7101	6.329	1.467	34.24	1.439	0.029
8101	6.153	1.462	34.38	1.588	0.045
1102	8.500	2.079	33.38	4.124	0.301
2102	8.664	2.261	36.12	3.939	0.180
3102	8.701	1.925	38.56	3.735	0.289
4102	8.820	2.351	40.09	3.345	0.094
5102	8.655	2.275	42.98	3.395	0.210
6102	8.850	2.069	43.89	3.215	-.008
7102	9.004	2.205	46.75	2.299	0.010
8102	8.951	2.231	48.00	2.292	0.080
1103	12.82	2.596	44.93	4.966	0.298
2103	13.55	2.885	50.22	4.945	0.260
3103	13.25	2.862	52.87	4.586	0.226
4103	13.63	2.780	55.52	4.096	0.046
5103	13.87	2.980	56.90	3.637	0.002
6103	13.13	2.717	58.63	3.503	0.153
7103	13.23	2.720	60.24	3.027	0.038
8103	13.81	2.638	57.32	3.346	0.024
1104	7.399	1.673	30.75	3.728	0.259
2104	7.918	1.577	33.37	3.037	0.102
3104	7.167	1.523	34.15	3.195	0.288
4104	8.267	1.997	38.14	3.059	0.422
5104	7.580	1.704	36.65	2.415	0.241
6104	7.504	1.706	37.78	2.652	0.259
7104	7.011	1.567	38.53	2.386	0.073
8104	8.090	1.851	40.26	2.641	0.189
1105	11.53	2.574	39.04	4.822	0.287
2105	11.27	2.683	45.37	5.252	0.240
3105	11.82	2.632	47.47	4.768	0.216
4105	11.43	2.501	51.68	3.924	0.123
5105	11.94	2.820	52.53	4.109	0.070
6105	11.28	2.669	53.75	3.747	0.031
7105	11.60	2.774	52.85	4.105	0.074
8105	11.94	2.687	55.95	3.269	0.020

Table 9-1 (continued)

Run No.	$\overline{\tau}$ (dynes/cm^2)	τ_{RMS} (dynes/cm^2)	$\overline{U}$ (cm/s)	U_{RMS} (cm/s)	Correlation Coefficient
1106	17.38	3.276	53.53	5.415	0.325
2106	17.00	3.103	55.12	4.752	0.216
3106	17.05	3.414	55.35	3.590	0.171
4106	16.71	3.357	58.99	4.040	0.189
5106	16.76	3.472	61.80	3.499	0.107
6106	17.09	3.497	65.97	4.138	0.158
7106	17.31	3.303	67.98	3.360	0.101
8106	17.45	3.446	74.91	2.736	0.062
1107	7.584	1.669	32.00	3.276	0.305
2107	8.200	1.845	37.15	4.011	0.253
3107	8.714	2.044	36.91	3.477	0.215
4107	8.285	2.009	37.96	3.315	0.227
5107	8.780	1.979	41.80	3.377	0.177
6107	8.273	1.906	41.21	2.897	0.274
7107	7.709	1.847	41.32	2.634	0.180
8107	7.666	2.185	42.41	3.001	0.155
1108	15.23	3.049	54.29	5.639	0.331
2108	15.93	3.161	60.24	5.264	0.232
3108	15.81	3.051	63.03	5.240	0.235
4108	15.66	3.139	62.53	4.710	0.128
5108	15.48	3.056	66.26	4.838	-0.040
6108	15.33	3.158	67.23	4.193	0.198
7108	15.40	3.103	68.14	3.801	-0.003
8108	15.75	3.001	69.59	3.304	-0.090
1109	19.48	3.543	66.58	6.763	0.313
2109	20.00	3.770	74.72	5.845	0.286
3109	19.75	3.569	76.28	5.146	0.240
4109	20.26	3.743	78.45	4.967	0.159
5109	19.53	3.701	76.96	4.045	0.060
6109	19.73	4.014	78.27	4.142	0.054
7109	20.37	3.648	84.09	3.087	0.063
8109	20.12	3.650	81.92	3.357	0.037
1104	11.19	2.013	25.64	4.851	0.532
2104	10.55	1.765	28.55	4.401	0.444
3104	11.04	1.801	30.62	4.404	0.294
4104	10.88	1.950	31.50	4.009	0.321
5104	10.36	1.771	31.62	3.998	0.264
6104	10.26	1.955	32.03	4.259	0.377
7104	10.49	2.037	33.90	4.150	0.374
8104	10.25	1.793	33.98	4.031	0.206
9104	10.06	1.763	35.02	3.900	0.225

Table 9-1 (continued)

Run No.	$\overline{\tau}$ (dynes/cm^2)	τ_{RMS} (dynes/cm^2)	$\overline{U}$ (cm/s)	U_{RMS} (cm/s)	Correlation Coefficient
1104*	12.15	2.096	25.09	4.792	0.542
2104*	11.74	1.894	28.32	4.599	0.378
3104*	10.64	1.811	29.63	4.267	0.388
4104*	10.12	1.681	30.44	3.999	0.240
5104*	10.50	1.784	32.08	3.949	0.251
6104*	10.43	1.912	33.08	4.482	0.244
7104*	10.53	1.802	33.58	4.233	0.274
8104*	10.65	1.783	34.03	4.123	0.187
9104*	10.57	1.832	35.71	4.037	0.150
1107	11.21	2.134	29.78	4.355	0.362
2107	11.74	2.268	32.40	5.452	0.530
3107	11.43	2.123	35.96	4.568	0.484
4107	11.95	2.132	37.36	4.801	0.327
5107	10.75	1.768	35.17	4.231	0.206
6107	11.22	1.858	38.45	4.389	0.309
7107	11.10	2.013	38.47	5.180	0.349
8107	11.68	1.988	38.56	3.883	0.141
9107	10.79	2.022	37.80	4.892	0.280
1107*	13.71	2.154	26.44	4.875	0.509
2107*	13.26	2.076	31.75	4.625	0.426
3107*	12.42	2.055	32.86	4.611	0.298
4107*	12.26	2.027	34.38	4.483	0.277
5107*	12.11	1.971	34.63	4.193	0.355
6107*	12.44	1.987	35.69	4.029	0.181
7107*	11.47	1.956	35.82	4.150	0.289
8107*	11.72	2.292	35.95	4.023	0.233
9107*	11.75	2.140	36.88	4.923	0.339
1111	7.799	1.443	15.55	4.045	0.655
2111	7.777	1.300	17.03	3.274	0.505
3111	7.596	1.385	19.82	3.812	0.434
4111	7.646	1.322	21.23	3.583	0.478
5111	7.497	1.249	22.64	3.798	0.467
6111	7.183	1.261	25.44	3.542	0.347
7111	6.969	1.436	25.59	3.930	0.404
8111	6.880	1.127	26.68	3.403	0.246
9111	7.011	1.307	26.83	3.569	0.297
1111*	9.650	1.828	13.39	4.244	0.722
2111*	9.484	1.563	18.67	3.830	0.549
3111*	8.464	1.574	19.26	3.812	0.581
4111*	8.569	1.329	21.25	3.366	0.381
5111*	8.392	1.379	22.59	3.853	0.338
6111*	7.945	1.414	23.04	2.923	0.311
7111*	7.864	1.488	23.20	3.157	0.283
8111*	8.132	1.552	24.43	3.280	0.390
9111*	7.744	1.611	24.50	3.503	0.319

*off centerline

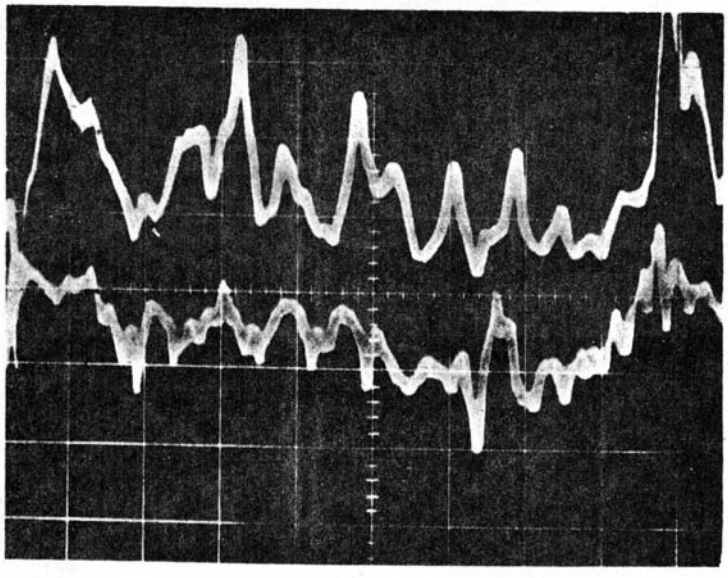

Plate 9-1. Oscilloscope traces of boundary shear stress (upper) and velocity (lower) for 0.01 relative depth.

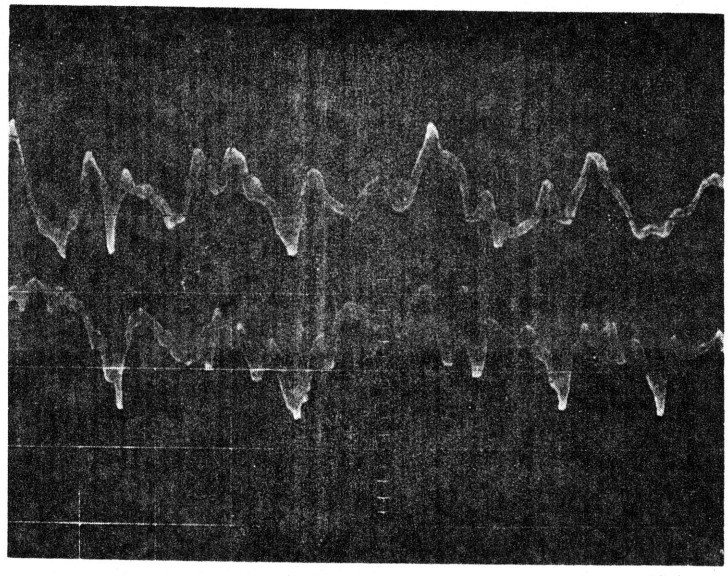

Plate 9-2. Oscilloscope traces of boundary shear stress (upper) and velocity (lower) for 0.1 relative depth.

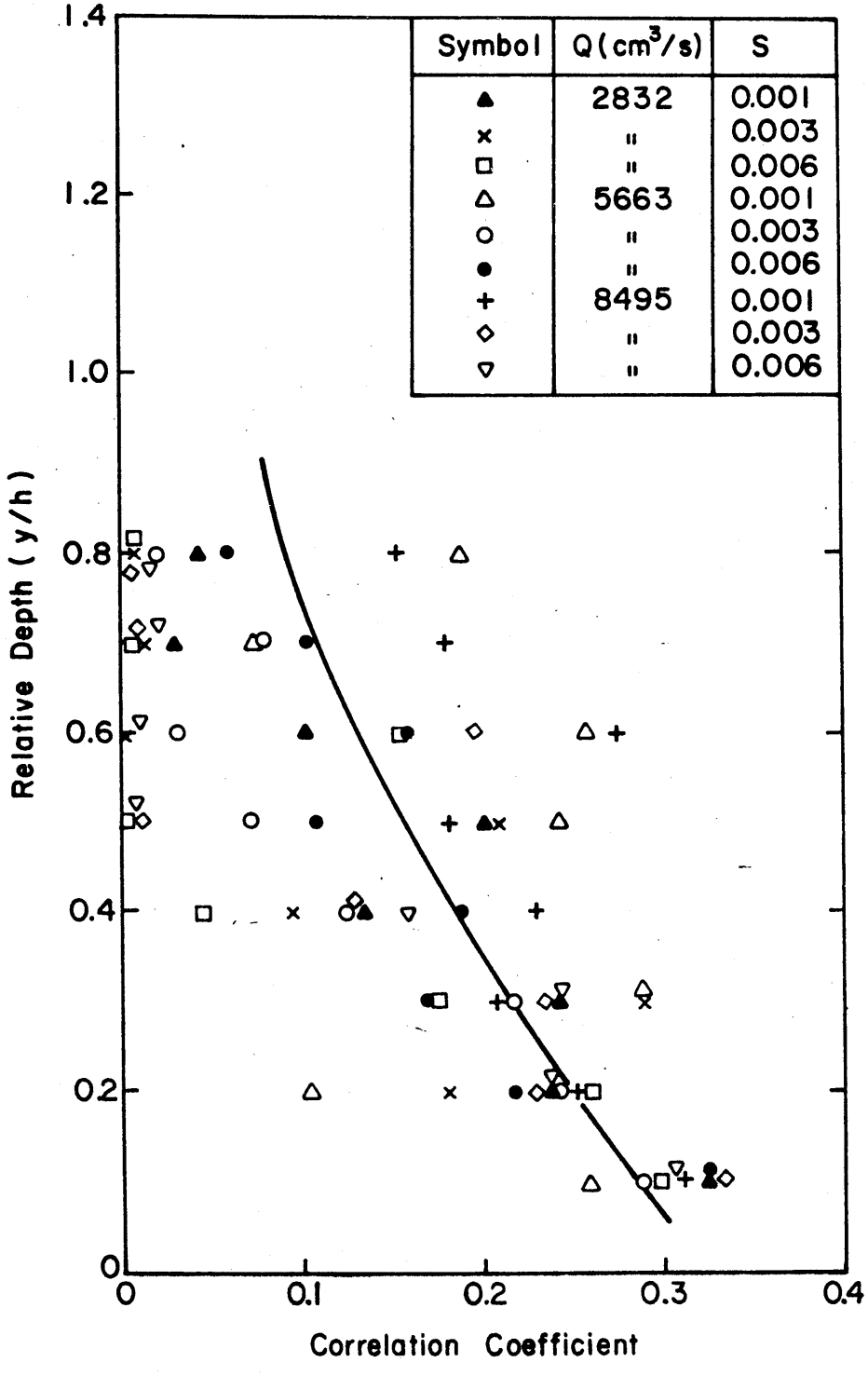

Figure 9-1. Correlation coefficient as a function of relative depth ($0.1 \leq y/h \leq 0.8$).

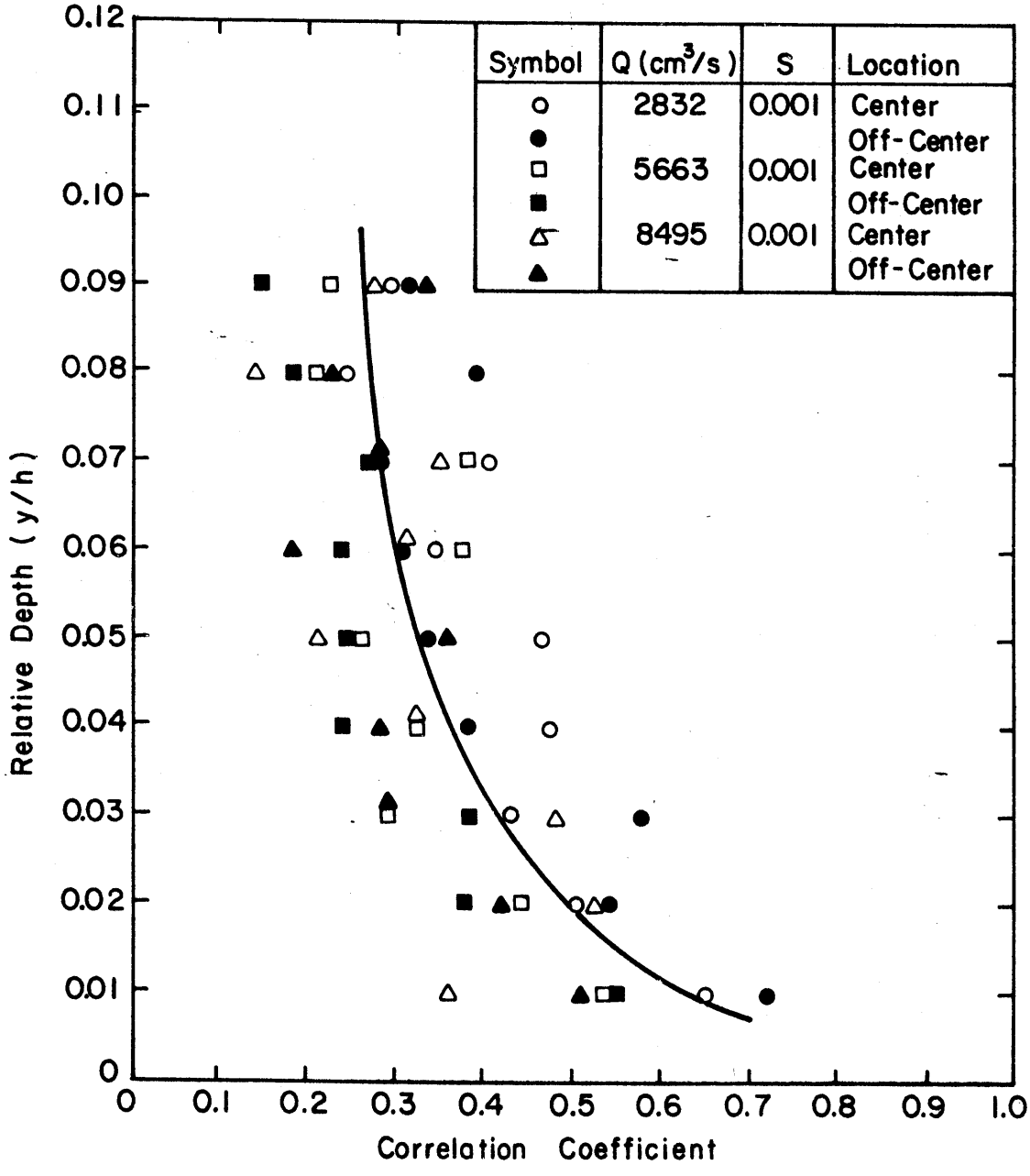

Figure 9-2. Correlation coefficient as a function of relative depth ($0.01 \leq y/h \leq 0.09$).

the correlation coefficient relationship to relative depths. Figure 9-1 is for relative depths of 0.1 to 0.8. Figure 9-2 shows the correlation coefficient relationship to relative depths less than 0.1. The maximum correlation coefficient observed was 0.6 (y/h equal to 0.01) decreasing to approximately zero for y/h of 0.8. The results indicate the correlation between fluctuating velocity and fluctuating boundary shear stress decreases with increasing distance from the wall.

9.4 Secondary Current Results

Examination of velocity isovels can identify regions of strong secondary current through compression or expansion of isovels. Measurement of velocity isovels and boundary shear stress distribution, under the same hydraulic flow conditions, can be used to qualitatively evaluate secondary current effects on the boundary shear stress. Two flow conditions were examined, identified by flow condition numbers 4 and 10 (Table 6-2). Velocity profiles were measured using a TSI Model 1218-20W hot-film velocity probe.

The measured isovels for one-half of the channel are shown in Figures 9-3 and 9-4 for discharges of 5663 cm^3/s and 11327 cm^3/s, respectively. Boundary shear stress values are identified at measuring locations around the perimeter. The most apparent relationship of isovel compression to maximum boundary shear stress occurs in Figure 9-4. Along the channel side the maximum boundary shear stress occurs simultaneously with compression of the isovel lines.

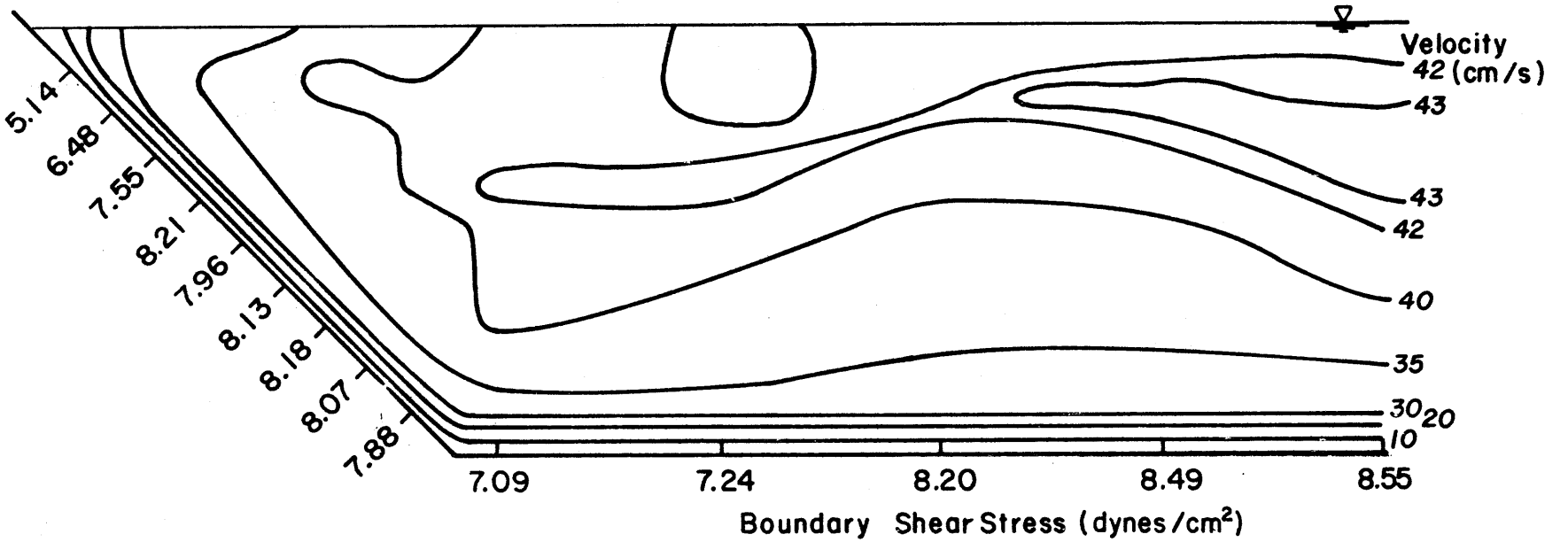

Figure 9-3. Velocity isovels and boundary shear stress measurements for 5663 cm^3/s.

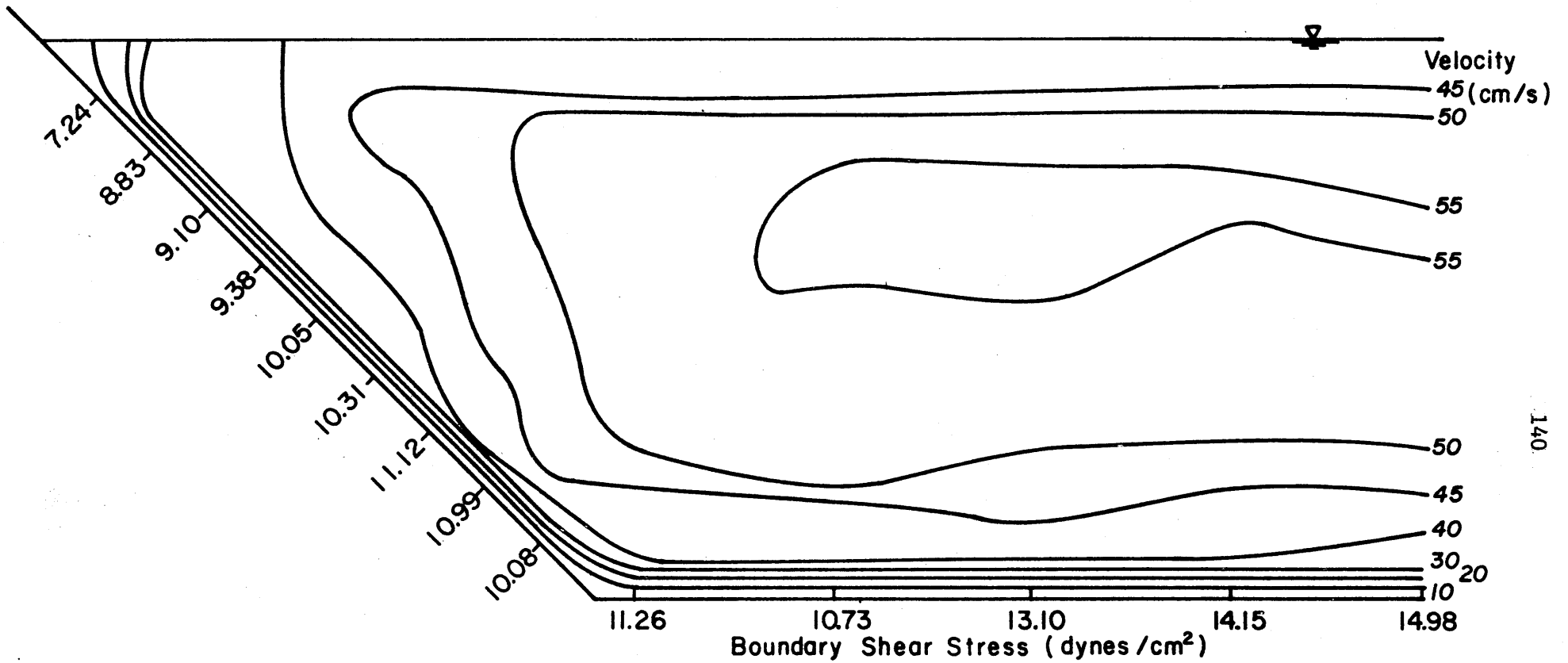

Figure 9-4. Velocity isovels and boundary shear stress measurements for 11327 cm^3/s.

X. CONCLUSIONS AND RECOMMENDATIONS

10.1 Conclusions

The nonuniform spatial distribution of the mean boundary shear stress and the stochastic nature of the instantaneous values creates a complex turbulent structure near the wall boundary. Direct mathematical formulation predicting this turbulent structure is extremely difficult, and only limited experimental data exists. Despite immense interest in boundary shear stress processes, no systematic information was previously available that described the boundary shear stress in terms of its spatial and time distributions. The results of this investigation have provided basic information towards the objective of understanding turbulent boundary shear stress processes.

The research effort in this investigation was oriented to exploring many different aspects relating to boundary shear stress. The design of experimental facilities and proper instrumentation for use in boundary shear stress research was a necessary prerequisite. The development of an efficient data acquisition scheme provided for consistent and accurate data. The large amount of data that resulted could have been analyzed in many different ways; however, only the basic trends for each experiment were sought out. The most important results from this research are summarized in the following paragraph.

Cross-streamwise distribution of boundary shear stress was not predictable using mean flow parameters; however, the maximum shear stress was predictable. In the design of stable channels the maximum shear stress is an important variable. Experimental data agreed closely with the analytical results of Lane (1) for prediction of maximum average shear stress on the sides and bottom of a channel.

Instantaneous boundary shear stress measured in the cross-streamwise direction indicated a similarity to the theoretical lognormal distribution. The measured variation of mean boundary shear stress in the streamwise direction for nonuniform flow compared well with analytical computations. Discrepancies between measured and calculated values occurred when the pressure distribution was not hydrostatic. An analytical model for predicting turbulent velocity fluctuations compared excellently to measured data. The PDF of the measured velocity fluctuations near the wall were approximately normally distributed as compared to the lognormally distributed shear stress fluctuations. A strong correlation exists between the velocity fluctuations in the near wall region and the fluctuations of boundary shear stress. The correlation decreases steadily with increasing distance from the wall. Compression of mean velocity isovels, indicating strong secondary current effects, corresponded to increasing boundary shear stress.

The potential application of the knowledge gained from this research covers a broad range of subjects. An understanding of turbulence is an important factor to many design and research projects in the fields of hydraulics, sanitary and chemical engineering. Specific topics that may benefit from this investigation include:

1) sediment transport processes,
2) stable channel design,
3) incipient motion,
4) riprap design,
5) solid particle settlement, and
6) diffusion and dispersion of pollutants.

A number of research topics can be suggested that concentrate on specific areas investigated during this research effort. The potential for hot-film anemometry as a measurement technique for complete investigation of turbulent boundary shear stress in rigid channel systems is apparent.

10.2 Specific Recommendations

The use of hot-film anemometry in this project to investigate turbulent boundary shear stress has indicated specific areas where knowledge is lacking. Investigation of these topics involving an alluvial boundary would require a different measurement technique. The recommendations for research on these topics are:

1. Two-dimensional investigation of turbulent boundary shear stress so that the direction of the boundary shear stress could be identified,
2. Measurement of boundary shear stress processes and related phenomena in fixed roughness channels,
3. Measurement of boundary shear stress processes and related phenomena in movable bed channels using an alternate technique, such as laser doppler anemometry,
4. Investigation of the two-dimensional turbulent boundary shear stress distributions in channel bends, and
5. Research on the boundary shear stress distribution in the nonuniform flow conditions of a hydraulic jump, or for flow under a sluice gate.

Research in these areas should be accompanied by mathematical modeling based on physical concepts. Empirical curve fitting provides

the solutions to problems only under the specific conditions that the data was taken. Model development using basic physical principles to formulate the model equations and experimental data to calibrate the model constants is a more practical approach. Models derived in this manner are more general and apply to a wider range of conditions.

REFERENCES

1. Lane, E. W., "Design of Stable Channels," Proceedings, ASCE, Vol. 120, Separate No. 280, 1953.

2. Blinco, P. H., "Spatial Structure of the Viscous Sublayer," thesis presented to Colorado State University, Fort Collins, Colorado, in partial fulfillment of the requirements for the Degree of Doctor of Philosophy, 1974.

3. Rouse, H., Advanced Mechanics of Fluids, Robert E. Krieger Publishing Company, New York, 1976.

4. Daily, J. W. and Harleman, D. R. F., Fluid Dynamics, Addison-Wesley, Massachusetts, 2nd edition, 1973.

5. Henderson, F. M., Open Channel Flow, New York: Macmillan, 1966.

6. Olson, R. M., Essentials of Engineering Fluid Mechanics, International Textbook Company, 1973.

7. Einstein, H. A. and El-Samni, E. A., "Hydrodynamic Forces on a Rough Wall," Review of Modern Physics, Vol. 21, No. 3, 1949.

8. Cheng, E. D. H. and Clyde, C. C., "Instantaneous Hydrodynamic Lift and Drag Forces on Large Roughness Elements in Turbulent Open Channel Flow," Sediment Symposium to Honor H. A. Einstein, edited by H. W. Shen, Colorado State University, 1971.

9. Blinco, P. H. and Simons, D. B., "Characteristics of Turbulent Boundary Shear Stress," Journal of the Engineering Mechanics Division, ASCE, Vol. 100, 1974.

10. Leliavsky, S., An Introduction to Fluvial Hydraulics, Dover Publications, New York, 1966.

11. O'Brien, M. P. and Rindlaub, B. D., Discussion of "Sand Mixtures and Sand Movement in Fluvial Models," Transactions, ASCE Paper No. 1909, Vol. 100, 1935.

12. Olsen, O. J. and Florey, Q. L., "Sedimentation Studies in Open Channels - Boundary Shear and Velocity Distribution by Membrane Analogy, Analytical and Finite Difference Methods," Laboratory Report No. SP34, Bureau of Reclamation, 1952.

13. Replogle, J. A. and Chow, V. T., "Tractive Force Distribution in Open Channels," Journal of the Hydraulics Division, ASCE, Vol. 92, No. HY2, 1966.

14. Ippen, A. T. and Drinker, P. A., "Boundary Shear Stresses in Curved Trapezoidal Channels," Journal of the Hydraulics Division, ASCE, Vol. 88, No. HY5, 1962.

15. Davidian, J. and Cahal, D. I., "Distribution of Shear Stress in Rectangular Channels," U.S. Geological Survey Paper No. 475-C, Article 113, 1963.

16. Rajaratnam, N. and Muralidhar, D., "Boundary Shear Stress Distribution in Rectangular Open Channels," LaHouille Blanche, Vol. 24, No. 6, 1969.

17. Kartha, V. C. and Leutheusser, H. J., "Distribution of Tractive Force in Open Channels," Journal of the Hydraulics Division, ASCE, Vol. 96, No. HY7, 1970.

18. Bathurst, J. C., "Distribution of Boundary Shear Stress in Rivers," paper presented to the Tenth Annual Geomorphology Symposium, September, 1977.

19. Wylie, K. F., Alonso, C. V., and Coleman, N. L., "Some Stochastic Properties of Turbulent Tractive Forces in Open-Channel Flows," paper presented to Turbulence in Liquids Conference, Rolla, Missouri, 1977.

20. Tan-Atichat, J., Nagib, H. M., and Pluister, J. W., "On the Interpretation of the Output of Hot-Film Anemometers and a Scheme of Dynamic Compensation for Water Temperature Variation," Proc., Third Symposium on Turbulence in Liquids, September, 1973.

21. Roadman, R. E., "The Flow in the Wake of Flat Plates at Low Reynolds Numbers," thesis presented to Colorado State University, Fort Collins, Colorado, in partial fulfillment of the Degree of Master of Science, 1977.

22. Bendat, J. S. and Piersol, A. G., Random Data: Analysis and Measurement Procedures, Wiley-Interscience, 1971.

23. Otnes, R. K. and Enochson, L., Digital Time Series Analysis, Wiley-Interscience, 1972.

24. Simons, D. B. and Senturk, F., Sediment Transport Technology, Water Resources Publications, Fort Collins, Colorado, 1976.

25. Croley, T. E. II, Hydrologic and Hydraulic Computations on Small Programmable Calculators, Iowa Institute of Research, 1977.

26. Schlichting, H., "Layer Theory," 6th edition, McGraw-Hill Book Co., Inc., New York, New York, 1968, p. 546.

27. Parzen, E., "Stochastic Processes," Holden-Day, Inc., San Francisco, California, 1967, pp. 14-15.

28. McQuivey, R. S. and Richardson, E. V., "Some Turbulence Measurements in Open Channel Flow," Journal of the Hydraulics Division, ASCE, Vol. 95, 1969.

29. Laufer, J., "The Structure of Turbulence in Fully Developed Pipe Flow," National Advisory Committee for Aeronautics Report No. 1174, 1954.

30. Rechardt, H., Messungen Turbulenter Schwankungen, Naturwissenschaften 104, 1938.

31. McQuivey, R. S., "Summary of Turbulence Data from Rivers, Conveyance Channels and Laboratory Flumes," U.S. Department of the Interior, Geological Survey, Water Resources Division, open-file report, Bay St. Louis, Mississippi, 1972.

32. Kline, S. J., Reynolds, W. C., Schraub, F. A., and Runstadler, P. W., "The Structure of Turbulence in Fully Developed Pipe Flow," National Advisory Committee for Aeronautics Report No. 1174, 1967.

33. Sandborn, V. A. and Pyle, W. L., "Evaluation of the Surface Shear Stress Along Rearward Facing Ramps," Colorado State University Research Memorandum No. 25, October, 1975.

34. Li, L. Y., "Data Analysis on Turbulent Velocities and Boundary Shear Stresses," thesis presented to Colorado State University, Fort Collins, Colorado, in partial fulfillment of the requirements for the Degree of Master of Science, 1977.

APPENDIX A - CALIBRATION OF BOUNDARY SHEAR STRESS PROBES IN TURBULENT PIPE FLOW

The commonly accepted calibration facility for one-dimensional flush surface hot-film (FSHF) probes is fully developed pipe flow. Due to the circular geometric shape, the shear stress distribution can be assumed uniform around the perimeter. Applying the momentum equation to a control section yields the theoretical mean boundary shear stress,

$$\bar{\tau} = \frac{\gamma D}{4} \frac{\Delta h}{\Delta x} \tag{A-1}$$

where D is the pipe diameter, γ is the specific weight of fluid, and $\Delta h/\Delta x$ is the piezometric gradient. Therefore, after measuring the piezometric gradient, or pressure drop in the pipe, with a pressure transducer (Appendix B) the shear stress in the pipe can be calculated. A significant drawback to this approach is the inability to match the probe flush to the pipe wall, due to the pipe curvature. As the pipe diameter increases, the significance of this problem diminishes.

Following this procedure, calibration of FSHF probes were attempted in the four-inch return pipe of the flume. There were both advantages and disadvantages to using this pipe. The advantages included calibration of the FSHF probes in the same environment in which they would be used and ease in checking the calibration since the pipe is part of the test facility. The disadvantages were more transparent and not fully realized until the actual testing began.

The length of pipe available was 23 feet with a diameter of 4 inches. Assuming the 40 pipe diameters are required to achieve fully developed turbulent flow, the calibration location needed to be 13.3

feet downstream. This allowed 9.7 feet to the outlet, which is more than adequate to establish the pressure gradient. Assuming 40 diameters to be a sufficient length to establish fully developed turbulent flow is somewhat arbitrary since the actual length depends on many factors, including the flow condition and the type of entrance the flow follows to the pipe. Most estimates of the entrance length assume that the flow enters the pipe through a relatively smooth transition from a large container. This was not the case in the recirculating pipe because the pump for the flume was at the beginning of the 23-foot length. Initially, it was thought that the disturbance from the pump would be dampened out quickly and would not significantly affect the calibration of the FSHF probes. To check this assumption a moody-type diagram was developed using a dimensionless coefficient of resistance and Reynolds number. The dimensionless coefficient resistance is defined as

$$\lambda = \frac{8\tau_o}{\rho U^2} \qquad \text{(A-2)}$$

where τ_o is the shearing stress at the wall, ρ is the fluid density and U is the mean flow velocity. Figure (A-1) shows the graph along with the Blasuis solution for laminar flow in a smooth circular pipe. The data points fit the accepted curve for relative roughness, ε/d, of 0.002 quite well above a Reynolds number of 4×10^4. Below this Reynolds number the data scattered quite a bit and were not very repeatable. This indicated that above a Reynolds number of 4×10^4 a satisfactory flow condition existed for calibration, and below this Reynolds number the influence of the pump and the inlet conditions inhabited fully developed turbulent flow. Using this Reynolds number to define the lowest flow condition several calibrations were performed;

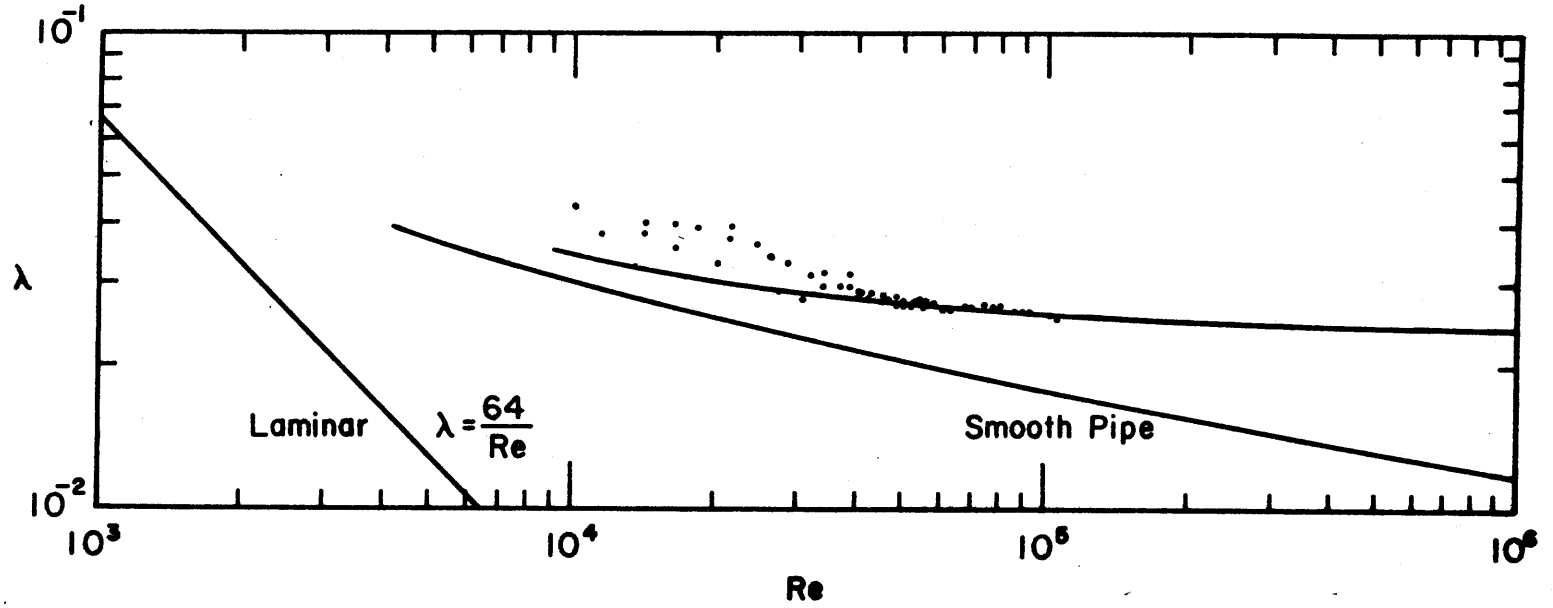

Figure A-1. Coefficient of resistance as a function of Reynolds number.

however, it was quickly realized that repeatability was not possible due to probe positioning problems in the 4-inch pipe. Also, the shear stress occurring in the pipe at a Reynolds number of 4×10^4 was considerably greater than the low values occurring in the open channel situation, requiring excessive extrapolation of the calibration curve. Considering these factors the laminar calibrating facility was designed and utilized for boundary shear stress calibration.

APPENDIX B - PRESSURE TRANSDUCER CALIBRATION

Measurement of differential pressure associated with pressure losses in a moving fluid can be accurately determined using pressure transducers. For the range of pressure of interest in one-dimensional boundary shear stress calibrations, Pace model DP-7 differential pressure transducers with 0.5 and 0.1 psi diagrams were used. These units were found to be extremely stable and reliable over long periods of time. A Pace model CD-25 signal conditioner and an Hewlett-Packard voltmeter comprised the readout device.

Calibration of the transducer was accomplished with a differential micromanometer. The design of the system allowed a quick check of the calibration, or adjustment of zero drift of the transducer, with a minimum amount of difficulty. The entire calibration procedure took only 15 minutes and consisted of applying varying amounts of differential head, Δh, to the transducer and then recording the voltage produced by the deflected diaphragm. A curve fit using the least squares technique on a programmable calculator provided a linear equation relating Δh to voltage in the form:

$$V = A(\Delta h) \tag{B-1}$$

where V is the voltage produced by the deflected diaphragm, Δh is the differential head causing the deflection, and A is the calibration constant.

The micromanometer was built in the Engineering Research Center shop. It consisted of two movable platforms for leveling purposes, positioned on a framework. The upper platform held two micrometers with a range of 0 to 25 millimeters. The lower platform held two Pyrex

funnels which formed the upper ends of a V-type manometer. The bottom of each funnel was attached to either side of the transducer so that a known Δh could be applied to the diaphragm. The enlarged size of the funnels minimized the effects of capillary action in the measuring region. The change of water surface elevation in the funnels, representing Δh, was measured with the micrometers similar to the way a depth-point gage would be used. To minimize surface tension effects between the water and the point of the micrometer, the point was cleaned and lightly coated with a silicon spray before each calibration. This procedure allowed precise measurement of the small differential pressure heads required in calibration. A diagram of the calibration stand, including the transducer and manifold network for connecting the transducer is shown in Figure B-1. Figure B-2 gives a typical calibration curve for the 0.5 psi diaphragm.

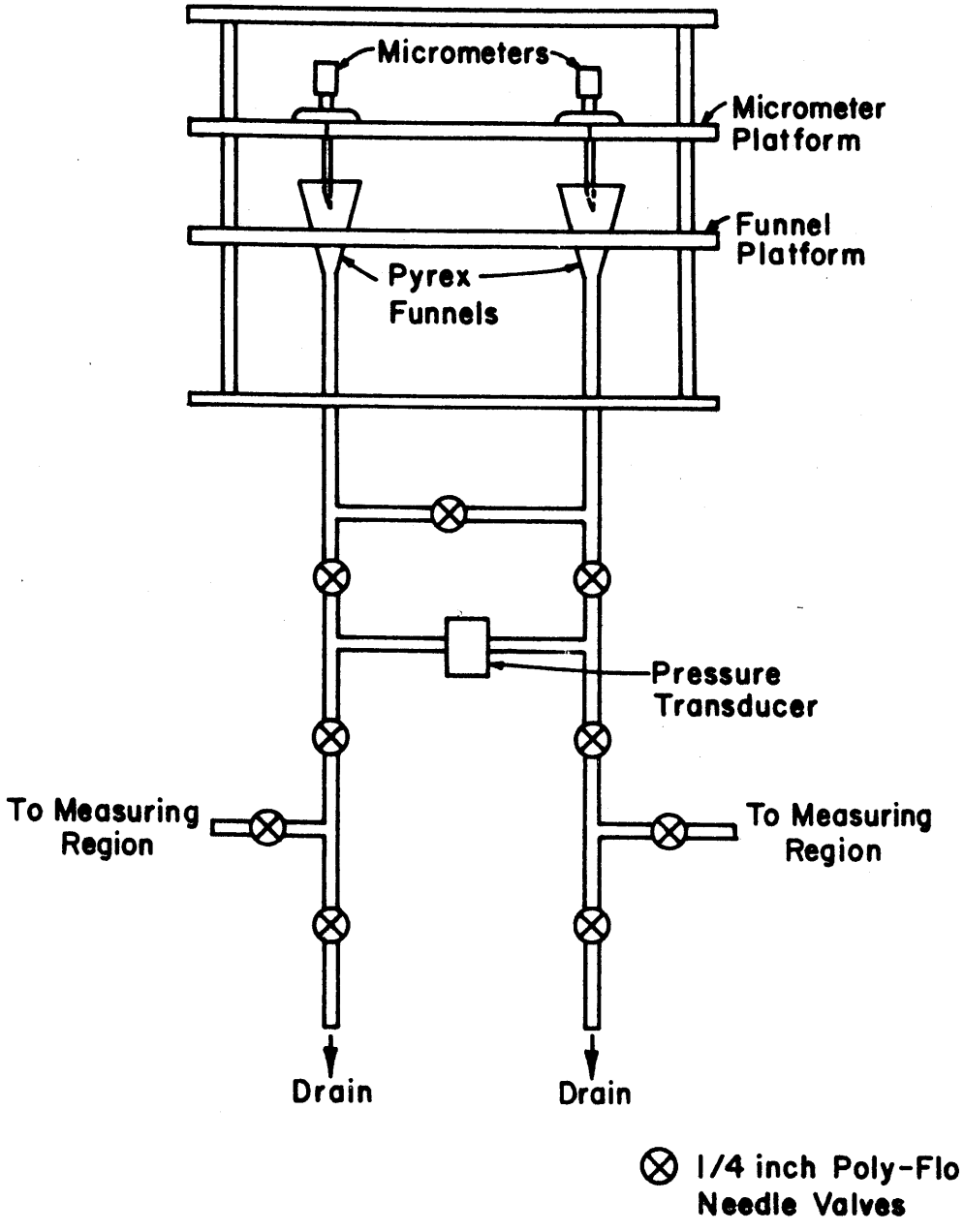

Figure B-1. Pressure transducer calibration facility.

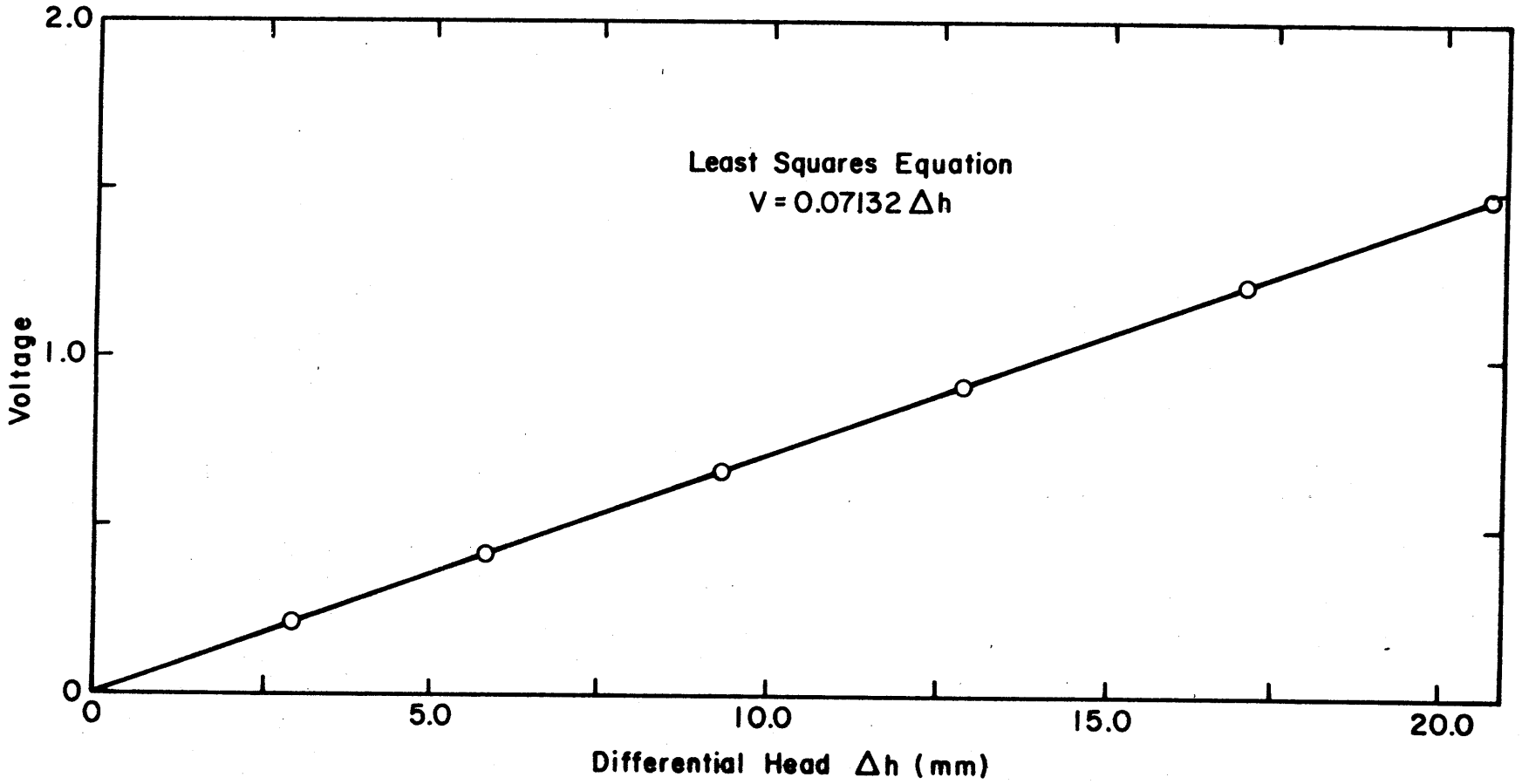

Figure B-2. Typical calibration curve for the pressure transducer.

APPENDIX C - REAL TIME DATA ACQUISITION AND ANALYSIS

Complete statistical analysis of turbulence data requires advanced data acquisition techniques. Before the widespread use of high-speed digital computers, extensive use of analog devices allowed limited statistical analysis in the laboratory. Generally, the analog devices were capable of analyzing the voltage time series only. When dealing with a non-linear transfer function, such as the voltage-velocity relation or voltage-shear stress relation in hot-film anemometry, this was a serious limitation. The analog devices were also highly specialized and expensive, requiring an elaborate instrument for each statistical property considered in the data analysis. A typical statistical analysis required four separate instruments: 1) mean value circuitry, 2) mean square circuitry, 3) probability density circuitry, and 4) frequency analysis circuitry.

When the use of large digital computers became feasible, a common technique used to record the analog voltage was on an FM recorder. Using the analog-to-digital converter that was part of the main computer system, the analog tape could be digitized and stored on digital tape. The digital tape was then read into the computer and the statistical analysis done numerically. The advantages to this procedure included the capability to transform the digitized voltage to physical units before the analysis, and also the fact that no specialized equipment for analysis needed to be purchased. The general disadvantages included the time lag involved from data acquisition to data analysis and results, and that a knowledge of the computer system and computer language was necessary. The time lag problem still exists, while computer knowledge is now taken for granted in any advanced research efforts. This type of data acquisition and analysis is still in widespread use.

At the Engineering Research Center, Colorado State University, a new system of data acquisition and analysis is in use. It is an advanced real time system utilizing the sophisticated technology of micro- and mini-computers. Real time analysis incorporates the advantage of analog devices that produce results in the laboratory, without the time lag disadvantage involved in an analysis using large digital computers. Real time systems are also referred to as interactive systems because the user "interacts" or communicates directly with the computer through teletypes. With this type of system a researcher uses the teletype at the laboratory location to direct the computer through the entire data acquisition, data analysis process. The mini-computer receives the analog voltage signal, digitizes it at the requested sampling rate, completes the user-specified analysis and outputs the results directly back to the teletype in the laboratory. There are neither specialized analog devices involved, nor the time lag associated with large digital computer systems. The system is fast, efficient and can be programmed to do a wide variety of data analysis.

The central element of the system at the Engineering Research Center is a Hewlett-Packard model 1000 mini-computer. The analog-to-digital device is a 15-channel Preston GMAD-4 and the teletype components are Texas Instrument Silent 700 computer terminals. Other peripherals include a 130 character Hewlett-Packard line printer and a Digi-Data Corporation nine track tape drive. The system has simultaneous input capabilities of four Silent 700 terminals and the console terminal located at the computer. Therefore, four researchers may operate independently at four remote locations using a total of 15 data lines to the A/D converter, collecting their data, performing the

analysis and receiving the results at their own Silent 700. Results may be directed to the line printer when the amount of output involved is large and data files can be stored for further analysis on the nine track tape drive. Data can be transferred to the large Cyber computer using the tape drive. This would be advantageous when a large amount of data is involved in the data reduction and analysis process, since large digital computers can operate at higher speed than mini-computers.

A real time data acquisition and analysis system is a powerful tool for investigations in turbulence. It maximizes the efficiency of experimental work, increases the reliability of the data and allows for thorough data analysis. These benefits give the researcher ideal conditions to pursue complex and intriguing topics.

APPENDIX D - NON-LINEAR AVERAGING

D.1 Definition of the Problem

Transformation of the voltage time series resulting from a one-dimensional flush surface hot film (FSHF) sensor into the turbulent shear stress time series is affected by non-linear averaging. The highly non-linear transfer function relating shear stress to voltage causes small voltage fluctuations to generate large shear stress fluctuations. The transfer function for boundary shear stress probes is

$$\tau^{1/3} = AE^2 + B \qquad \text{(D-1)}$$

where τ is the shear stress, E is the anemometer voltage output representing heat loss from the sensor and A and B are the calibration constants. In digital data analysis of boundary shear stress the analog voltage signal is completely transformed into a discrete shear stress time series by digitizing the voltage signal as some sampling rate and then applying the transfer function. In the transformation a non-linear averaging effect can occur causing a biasing of the entire turbulent shear stress time series. For a simple mean-to-mean transformation of data, no problem occurs. However, when the mean transfer function is used to transform the entire turbulent voltage time series to the turbulent shear stress time series, the mean value of shear stress calculated from the transformed time series differs from the mean value of shear transformed directly from the mean value of voltage. This is the non-linear averaging problem.

D.2 Current Methods to Compensate for Non-Linear Averaging

Several attempts have been made to eliminate this biasing of the turbulent shear stress time series. For turbulent velocity time series,

indirect methods such as local linearization methods, can give the correct values of the root-mean-square of a turbulent velocity signal represented by the transfer function

$$V^{1/2} = AE^2 + B \tag{D-2}$$

where V is the velocity, E is the anemometer output voltage representing heat loss from the sensor, and A and B are calibration constants. Local linearization methods are based on the assumption that

$$\frac{dE}{dV} = \frac{\sqrt{\overline{E'^2}}}{\sqrt{\overline{V'^2}}} \tag{D-3}$$

where $\sqrt{\overline{E'^2}}$ and $\sqrt{\overline{V'^2}}$ are the root-mean-square values of voltage E and velocity V, respectively, and the derivative, $\frac{dE}{dV}$, represents the slope of the voltage-velocity relation. It is apparent from Equation (D-3) that only the root-mean-square value of the turbulent signal can be corrected. Other statistical properties such as the skewness, kurtosis and frequency spectrum cannot be corrected by local linearization. Also, local linearization is applicable only to a voltage-velocity transfer function. The voltage-shear stress transfer function (Equation D-1) is too highly nonlinear and the probability distribution is too highly skewed for this procedure to work.

Electronic linearizers have also been developed for use with the voltage-velocity transfer function which transforms the nonlinear transfer function to a linear form. The linear relationship between linearized output and the velocity sensor input removes the nonlinear averaging problem. Again, this technique is applicable only to velocity sensors

and not to shear stress sensors because of the highly nonlinear, highly skewed relationships.

The first direct attempt to correct the calibration curve to eliminate the biasing of the entire turbulent shear time series was made by Sandborn and Pyle (33). An iterative procedure was used to correct the calibration curve so that the first moment of the fluctuations would be zero, as required by turbulence theory. The procedure involved determining the probability density (PDF) of the voltage time series and then using the mean-to-mean calibration relationship to compute the shear stress PDF. From the basic concept of the PDF the moments were calculated as

$$\overline{\tau'^n} = \int_{-\infty}^{\infty} \tau'^n \, p(\tau) d\tau' \quad . \tag{D-4}$$

According to the amount different from 0 this integral was for $n = 1$, the shift in the calibration curve could be calculated. The shift in the calibration curve then produced a different shear stress PDF and therefore a new calculation on the first moment. The process was found to converge normally after two iterations. While the procedure produced the correct calibration relationship, the iterative approach is time consuming and laborious.

In a different approach, Li (34) developed a computer-calculated calibration curve based on minimizing the sum of squares of the differences between the observed mean shear stresses and the mean shear stress calculated from the time series. The minimization was based on the least squares method. The primary difficulty with the procedure is that

it requires the entire digitized voltage series to be input to the computer program, which is elaborate for a calibration procedure.

D.3 Proposed Approach

To avoid the iterative procedures based on probability density analysis and the complexity of analyzing the entire turbulent voltage time series, a different calibration scheme is proposed. It is based on a perturbation analysis of the voltage-shear stress transfer function (Equation (D-1)).

The perturbation analysis involves the basic definitions of instantaneous voltage and shear stress,

$$E = \bar{E} + e \tag{D-5}$$

$$\tau = \bar{\tau} + \tau' \tag{D-6}$$

where E is the instantaneous voltage, $\bar{E}$ is the mean voltage, e is the voltage fluctuation, τ is the instantaneous shear stress, $\bar{\tau}$ is the mean shear stress, and τ' is the shear stress fluctuation. Applying Equations (D-5) and (D-6) to the transfer function gives (Equation (D-1))

$$\bar{\tau} + \tau' = A^3(\bar{E} + e)^6 + 3A^2B(\bar{E} + e)^4 + 3AB^2(\bar{E} + e)^2 + B^3 \quad . \tag{D-7}$$

Expanding Equation (D-7) gives

$$\bar{\tau} + \tau' = A^3[\bar{E}^6 + 6\bar{E}^5e + 15\bar{E}^4e^2 + 20\bar{E}^3e^3 + 15\bar{E}^2e^4 + 6\bar{E}e^5 + e^6]$$

$$+ 3A^2B[\bar{E}^4 + 4\bar{E}^3e + 6\bar{E}^2e^2 + 4\bar{E}e^3 + e^4] + 3AB^2[\bar{E}^2 + 2\bar{E}e + e^2] + B^3 \quad . \tag{D-8}$$

Taking the expected value of Equation (D-8) yields

$$\overline{\tau} + \overline{\tau'} = A^3[\overline{E}^6 + 6\overline{E}^5\overline{e} + 15\overline{E}^4\overline{e^2} + 20\overline{E}^3\overline{e^3} + 15\overline{E}^2\overline{e^4} + 6\overline{E}\overline{e^5} + \overline{e^6}]$$
$$+ 3A^2B[\overline{E}^4 + 4\overline{E}^3\overline{e} + 6\overline{E}^2\overline{e^2} + 4\overline{E}\overline{e^3} + \overline{e^4}]$$
$$+ 3AB^2[\overline{E}^2 + 2\overline{E}\overline{e} + \overline{e^2}] + B^3 \quad . \qquad \text{(D-9)}$$

According to definitions given by Equations (D-5) and (D-6) the average of the fluctuation, $\overline{e}$ and $\overline{\tau'}$, must be zero. Therefore, Equation (D-9) simplifies to

$$\overline{\tau} = A^3(C1) + 3A^2B(C2) + 3AB^2(C3) + B^3 \qquad \text{(D-10)}$$

where $C1 = \overline{E}^6 + 15\overline{E}^4\overline{e^2} + 20\overline{E}^3\overline{e^3} + 15\overline{E}^2\overline{e^4} + 6\overline{E}\overline{e^5} + \overline{e^6}$

$C2 = \overline{E}^4 + 6\overline{E}^2\overline{e^2} + 4\overline{E}\overline{e^3} + \overline{e^4}$

$C3 = \overline{E}^2 + \overline{e^2}$.

In order to obtain correct parameters for the calibration that yields the correct mean boundary shear stress resulting from the transformed time series, the relation shown in Equation (D-10) has to be satisfied for all of the calibration data. A least-square procedure is often employed to accomplish this.

The definition of an objective function, F(A,B), for the least-squares solution involving Equation (D-10) is

$$F(A,B) = \sum_{i=1}^{n} (\overline{\tau}_i - C4_i)^2 \qquad \text{(D-11)}$$

where $C4_i = A^3(C1_i) + 3A^2B(C2_i) + 3AB^2(C3_i) + B^3$

in which n is the number of data set for pair measurement of voltage and boundary shear stress, and i is the subscript indicating the ith data set. The least-square principle requires that the partial derivatives with respect to the parameters are equal to zero. Taking partial

derivatives with respect to A and B in Equation (D-11) and setting equal to zero yields

$$\frac{\partial F}{\partial A} = \sum_{i=1}^{n} 3A^2(C1_i) + 6AB(C2_i) + 3AB^2(C3_i)2(F_i - C4_i) = 0 \qquad \text{(D-12)}$$

and

$$\frac{\partial F}{\partial B} = \sum_{i=1}^{n} 3A^2(C2_i) + 6AB(C3_i) + 3B^2\, 2(\overline{\tau}_i - C4_i) = 0 \qquad \text{(D-13)}$$

Solving Equations (D-12) and (D-13) for A and B yields the true calibration constants. The values of the higher moments of the fluctuations are not usually known in an experimental calibration process; however, the value of $\overline{e^2}$ is often available by using a true root-mean-square (RMS) voltmeter. Therefore, it is desirable to estimate the significance and the sensitivity of the moments of the fluctuations greater than $\overline{e^2}$. If the calibration relationship can be shown sensitive only to $\overline{E}$ and $\overline{e^2}$, without the higher moments, then the procedure becomes a practical technique for estimating the true calibration constants. Only the mean voltage, $\overline{E}$, and the root-mean-square (RMS) voltage, $\sqrt{\overline{e^2}}$, and the mean boundary shear stress would need to be measured to solve the calibration equations.

To determine the significance of the higher order moments of the fluctuations, a computer program was written to do a sensitivity analysis. A boundary shear stress time series was constructed by assuming a mean boundary shear stress and superimposing a sine wave. The sine wave had an amplitude based on a percentage of the mean value. Using assumed values for the calibration constants A and B, the voltage time series was generated from the assumed boundary shear stress time series. The mean voltage and higher moments could then be calculated from the generated voltage time series. This procedure was repeated for a sequence of assumed mean boundary shear stresses separated by a known increment.

This generation of data provided a known environment to determine the sensitivity of the computed calibration constants to the higher order moments of the voltage fluctuation. The data was input to a computer routine that solved the calibration Equations (D-12) and (D-13) for A and B. The first solution included all the terms, and each proceeding solution eliminated the highest order term until the final solution was based only on the mean voltage, $\overline{E}$.

The results indicate that the calibration constants A and B are nearly constant as higher order terms are eliminated until only the mean value is left. In all cases there was a sudden change in A and B as the root-mean-square term was eliminated, leaving only the mean value. This is illustrated in Figure D-1 for coefficient A. The error in A and B increased as the percent amplification increased, indicating that the greater the turbulence or fluctuation, the more severe the error in using only the mean voltage values to determine the calibration constants. The order of magnitude of the error decreases by one with the addition of the RMS to the calibration processes.

Using this calibration scheme, the shear stress from a mean-to-mean transformation was compared to the time series estimated shear stress. With the corrected coefficients A and B the error due to nonlinear averaging was relatively stable at 3 percent. However, using the uncorrected coefficients from the mean-to-mean calibration to transform the entire time series resulted in a higher error. Figure D-2 illustrates this and indicates the greatest error occurred at the low shear stress values. The improvement in accuracy by using the corrected coefficients is apparent.

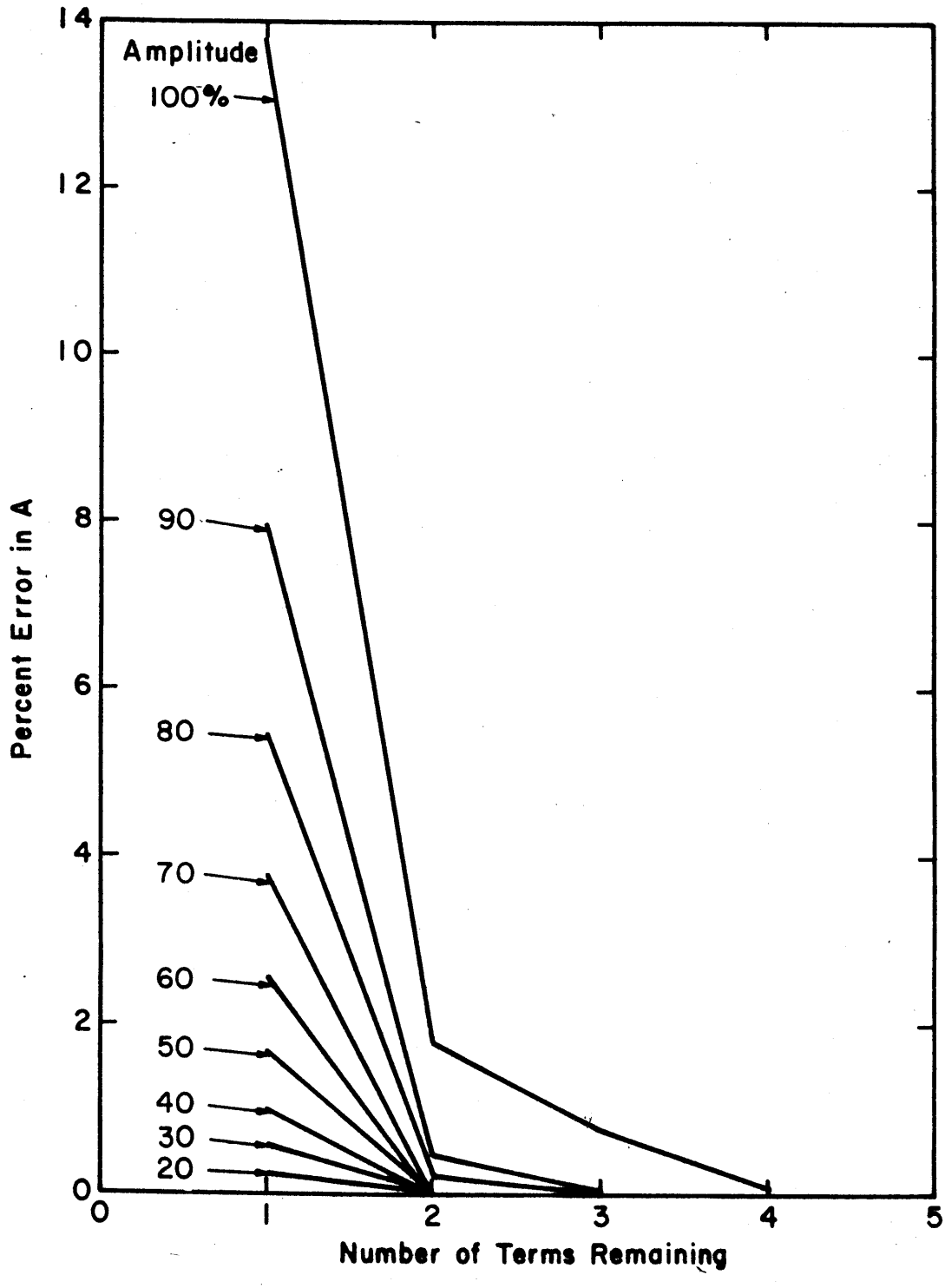

Figure D-1. Percent error in A as a function of the number of terms remaining in the expansion.

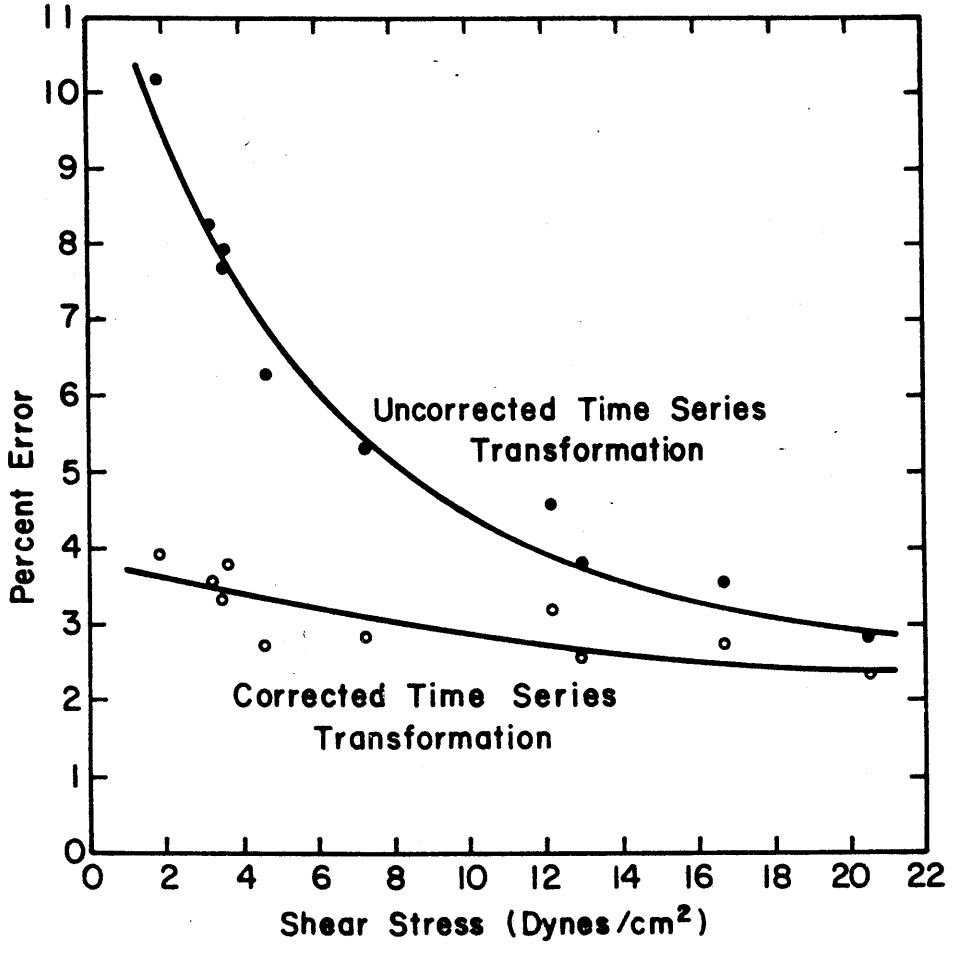

Figure D-2. Errors in computing mean shear stress from entire time series analysis.

APPENDIX E - SPLIT-FILM HOT-FILM CALIBRATION

E.1 General

The split-film hot-film (SFHF) sensor is a modification of a conventional cylindrical sensor. Two electrically independent films on a single quartz fiber provide two-dimensional velocity measurement capabilities. The principal of operation of the SFHF sensor is based on nonuniform heat transfer distribution around a constant temperature cylinder in a cross flow as shown in Figure E-1. It is assumed that the heat transfer distribution changes instantaneously with a change in velocity field and that heat transfer along the cylinder's axis is negligible compared to radial heat transfer. For modest length to diameter ratios the latter assumption is maintained. In addition, it is assumed that the turbulence scale has a negligible effect on the heat transfer characteristics. This is valid for moderate ratios of turbulent microscale to sensor diameter (2). Under these assumptions, calibration and operation of the SFHF sensor has been shown to be a valuable tool for turbulence measurements (2). The small size and unique design of SFHF sensors provides improved spatial resolution over other two-dimensional velocity probes. Measurements very close to a wall boundary are possible with digital time series analysis of both vertical and longitudinal components of velocity.

E.2 Development of Calibration Equations

Two calibration relationships are required for SFHF sensors. Considering the velocity field shown in Figure E-1, the effective instantaneous cooling velocity vector, q, is given by

$$q = \{(\overline{U} + u)^2 + v^2 + w^2\}^{1/2} \qquad \text{(E-1)}$$

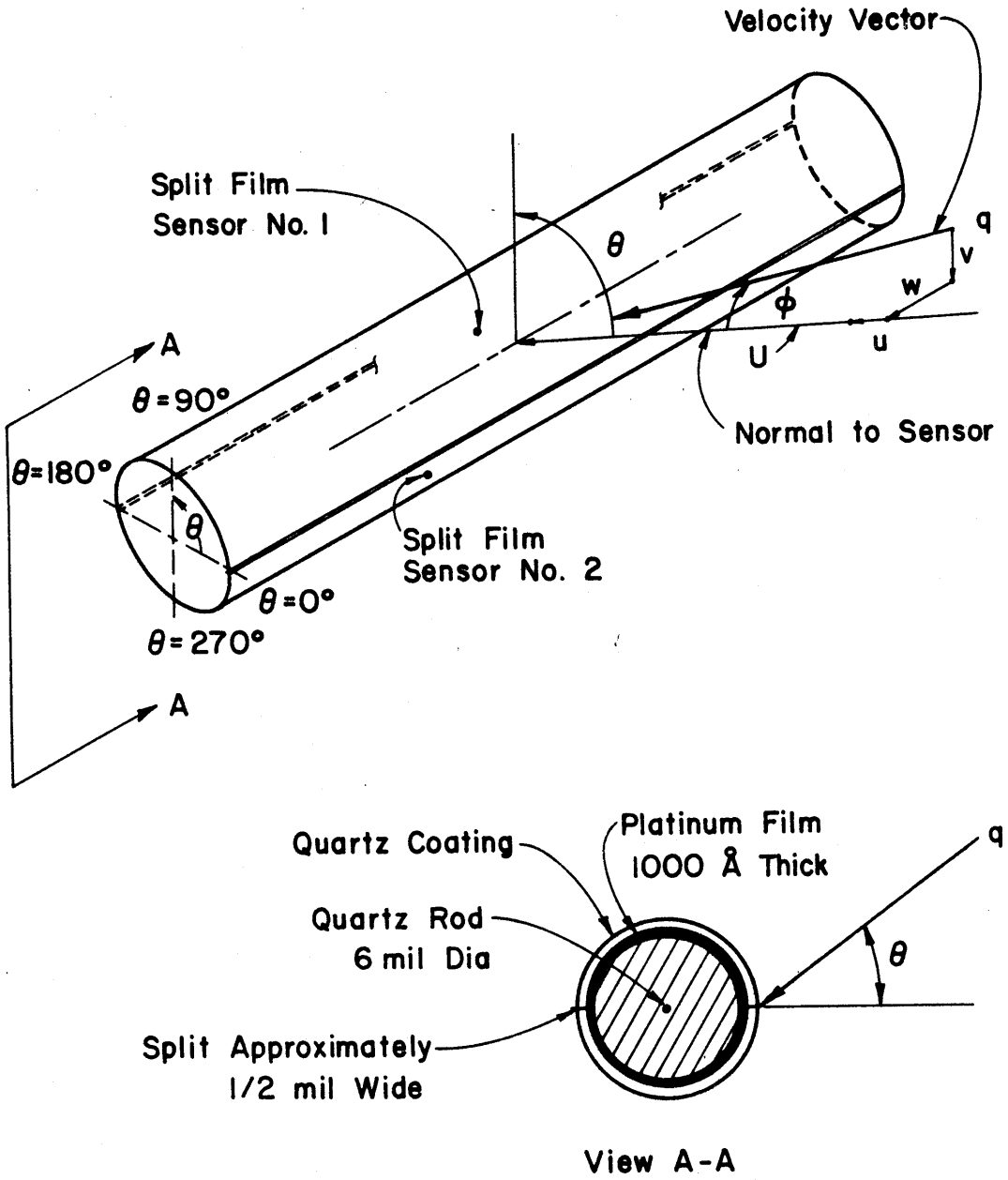

Figure E-1. Definition sketch of SFHF sensor.

where $\overline{U}$ is the temporal mean value of longitudinal velocity and u, v and w are the fluctuating velocity components in the longitudinal, vertical and traverse directions, respectively. The mean velocity is assumed to be a function of the vertical coordinate, y alone.

The sum of the heat transfer from the coaxially split sensors, E_s, is related to the magnitude of the effective cooling velocity q, in the form

$$E_s = (A_s + B_s q^n)\ F(\theta) \tag{E-2}$$

where

$$E_s = s_1 E_1^{\,2} + s_2 E_2^{\,2} \tag{E-2}$$

and

$$s_i = \frac{R_{c_i}\,\alpha_i}{R_{h_i}\,(R_{h_i} - R_{c_i})}\quad i = 1.2\quad . \tag{E-4}$$

E_i $(i = 1,2)$ is the individual split-film voltage output, α_i is the coefficient of thermal resistance, R_{h_i} and R_{c_i} are the electrical resistances at operating and ambient temperature, respectively, and $F(\theta)$ is some function of the azimuthal angle θ. The coefficients A_s, B_s and n are determined by calibration. For the SFHF sensors used in this study, E_s was a function of q alone, independent of $F(\theta)$ as Figure E-2 indicates. The final form of the first calibration relation is

$$E_s^{\,2} = A_s + B_s q^n\quad . \tag{E-5}$$

Two relations are possible for the second calibration equation. Previous studies have used some form of a difference equation

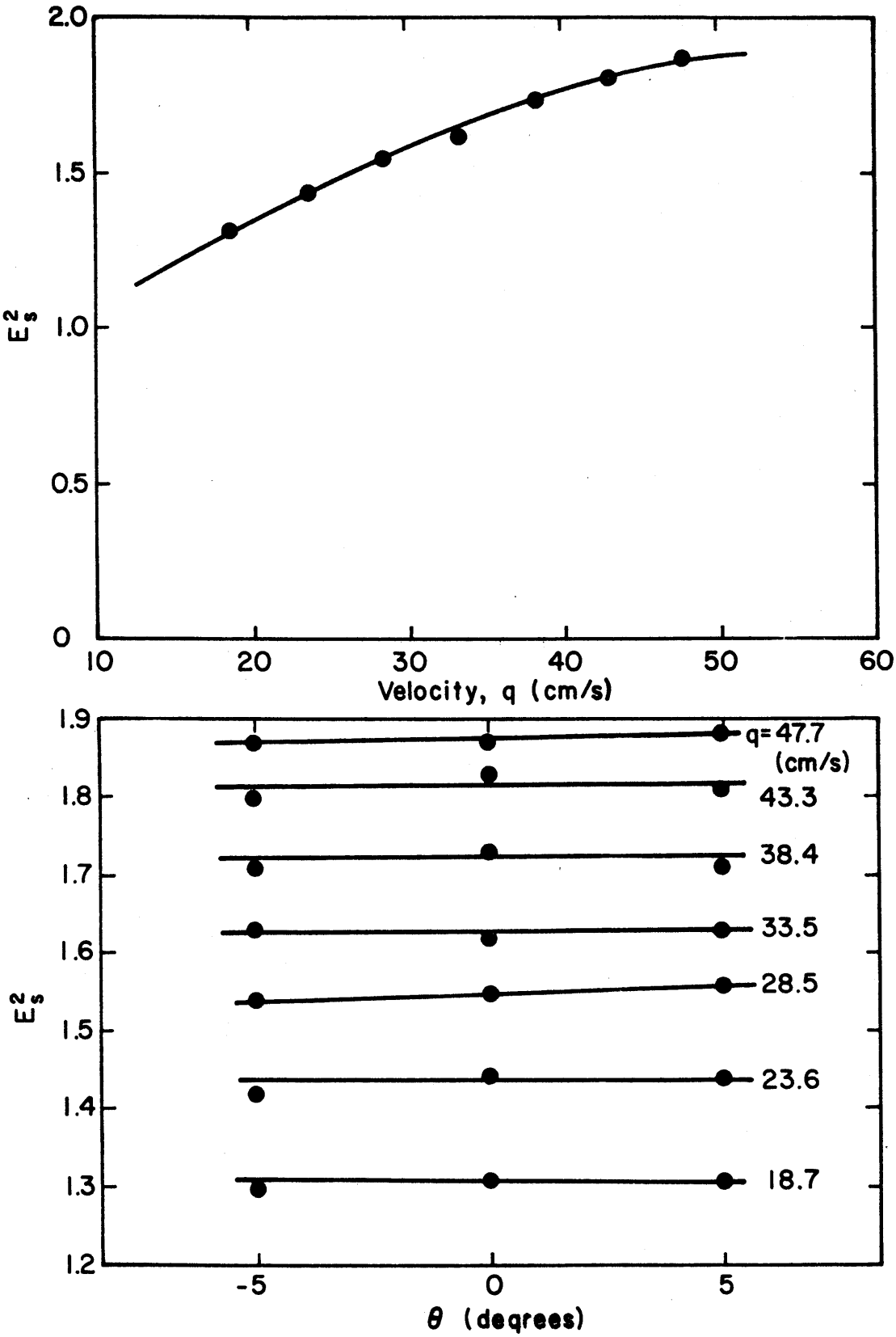

Figure E-2. E_s^2 relation to velocity and angle.

$$E_d^2 = (A_d + B_d\theta)\ F(q) \tag{E-6}$$

where

$$E_d^2 = s_1E_1^2 - s_zE_z^2 \quad . \tag{E-7}$$

A ratio equation of the form

$$E_R^2 = (A_R + B_R\theta^n)\ F(q) \tag{E-8}$$

where

$$E_R^2 = \frac{s_1E_1^2}{s_zE_z^2} \tag{E-9}$$

has also been employed (2).

After evaluating the difference relation in a number of calibration attempts it was concluded that the ratio relation would be more feasible. The primary difficulty with the difference relation was a sensitivity problem in subtracting two very small numbers to get a very small number. The E_d^2 values were found to be erratic and difficult to repeat. Based on the graphs of Figure E-3 it was concluded that the ratio, E_R^2, was primarily a linear function of theta, independent of the velocity q. This assumption is not entirely correct, but was considered realistic in terms of the other errors and problems when using hot films in water. The final form of the second calibration relation is

$$E_d^2 = A_d + B_d\theta \quad . \tag{E-10}$$

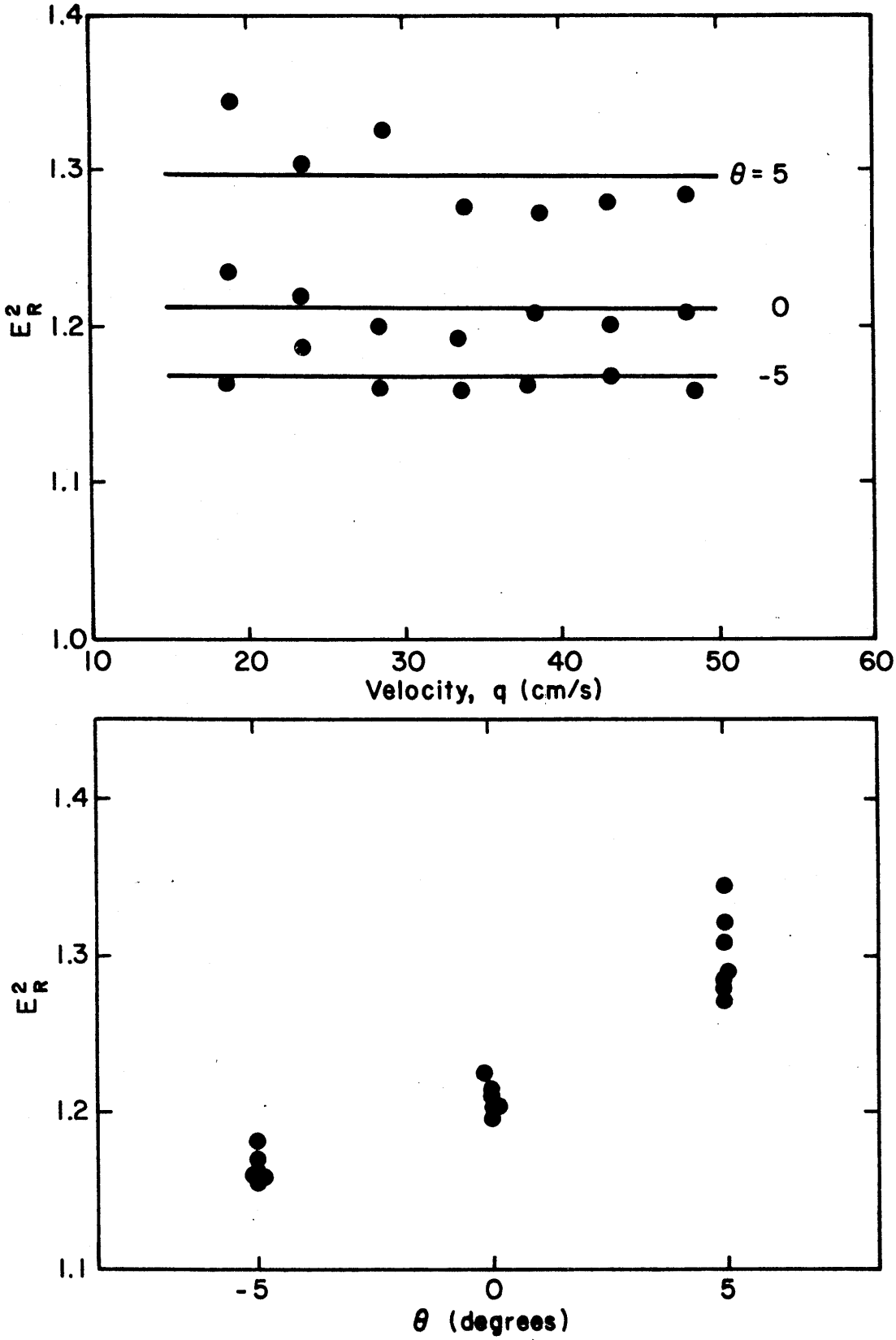

Figure E-3. E_R^2 relation to velocity and angle.

E.3 Operation of SFHF Sensor

Using Equations (E-5) and (E-10) calibration of the SFHF sensor was performed in the velocity calibration system previously discussed. The procedure consisted of maintaining a constant velocity and recording the mean voltage outputs for various rotation angles, θ. Velocity was then changed and the procedure repeated. An iterative least squares fit was performed to determine the coefficients A_s, B_s and n and a simple least squares fit was used to evaluate A_R and B_R.

The time series of the instantaneous velocity components was constructed from the inverse relationships

$$q(t) = \left(\frac{E_s(t)^2 - A_s}{B_s} \right)^{1/n} \tag{E-11}$$

and

$$\theta(t) = \frac{E_d(t) - A_R}{B_R} \quad .$$

Once $q(t)$ and $\theta(t)$ are calculated the time series components are constructed from

$$v(t) = q(t) \sin\theta\ (t) \tag{E-12}$$

and

$$u(t) = \sqrt{q(t)^2 - v(t)^2} \quad . \tag{E-13}$$

With this calibration scheme the statistical characteristics of the fluctuating velocity components could be investigated. The advantages of a real-time data acquisition system (Appendix C) made the split-film sensor a powerful and efficient means to study turbulent velocity fluctuations.

APPENDIX F - BOUNDARY SHEAR STRESS DATA

The variation of boundary shear stress in the cross-streamwise direction was investigated in four trapezoidal channel cross sections. Side slope ratios of 2:1, 1:1, 0.5:1 and 0:1 (where x:y refers to horizontal:vertical) were used in the variable geometry flume previously discussed. Fifteen hydraulic flow conditions consisting of five discharges and three slopes were studied for each trapezoidal cross section, resulting in a total of 60 experimental conditions. For each experiment eight locations of boundary shear stress were measured using TSI Model 1237W FSHF sensors. Measurements were taken on one-half of the channel bottom at four evenly spaced locations and also on the channel side at the 0.2, 0.4, 0.6 and 0.8 relative depths (y_i/h).

Different hydraulic and geometric flow conditions are identified by a four digit experiment number. The first digit identifies the measuring location. Locations 1, 3, 5, and 7 were on the channel bottom with location 1 on the centerline. Locations 2, 4, 6, and 8 refer to relative depths, y/h, of 0.2, 0.4, 0.6, and 0.8. A definition sketch of measuring locations was given in Figure 6-1. The second digit identifies the geometric side slope of the trapezoidal channels. The values 0, 5, 1 and 2 refer to side slope ratios of 0:1, 0.5:1, 1:1 and 2:1. The final two digits of the experiment number identify the hydraulic flow condition according to Table 6-2.

Measurements taken of the first four moments of boundary shear stress (mean, r.m.s., skewness and kurtosis) are reported in the following pages. In addition, the results of the goodness-of-fit testing to the normal and lognormal distributions by the Chi-square (χ^2) and Smirnov-Kolmogorov (S-K) statistics are provided.

Run No.	depth (cm)	$\bar{\tau}$ (dynes/cm^2)	r.m.s. (dynes/cm^2)	skewness	kurtosis	χ^2 normal	S-K	χ^2 log normal	S-K
1001	3.72	5.687	1.904	0.8839	4.1130	4629	0.0626	277	0.0135
3001	3.72	5.996	2.011	0.9280	4.4058	5325	0.0635	235	0.0113
5001	3.72	5.483	1.873	0.7768	3.6082	2912	0.0631	341	0.0165
7001	3.72	5.743	1.946	0.8762	3.8313	4023	0.0638	384	0.0192
2001	3.72	3.660	1.371	1.0254	4.9215	13939	0.0613	293	0.0128
4001	3.72	3.119	1.430	1.1463	4.8394	11503	0.0833	262	0.0175
6001	3.72	3.272	1.318	1.1103	4.8541	14078	0.0725	252	0.0145
8001	3.72	2.539	1.202	1.3000	5.1299	12745	0.0988	496	0.0347
1002	2.80	8.487	2.782	0.8610	3.9709	3683	0.0641	157	0.0120
3002	2.80	9.233	2.678	0.8148	3.8683	5797	0.0527	230	0.0164
5002	2.80	9.285	2.878	0.7821	3.5989	3041	0.0561	256	0.0149
7002	2.80	9.035	2.810	0.8368	3.7699	4060	0.0657	261	0.0155
2002	2.80	3.960	1.656	1.2303	5.4595	22395	0.0820	133	0.0091
4002	2.80	4.168	1.939	1.0145	4.4410	6146	0.0694	388	0.0250
6002	2.80	3.952	1.914	1.0866	4.6244	9190	0.0720	471	0.0252
8002	2.80	3.584	1.820	1.2428	5.4185	20982	0.0707	382	0.0289
1003	2.19	17.766	4.803	0.7185	3.5745	2532	0.0514	169	0.0107
3003	2.19	17.550	4.744	0.8465	4.1013	3748	0.0596	104	0.0075
5003	2.19	17.400	4.640	0.6949	3.5663	2240	0.0494	138	0.0111
7003	2.19	17.081	4.424	0.6365	3.3996	1708	0.0427	158	0.0126
2003	2.19	7.640	2.805	0.9318	4.4214	6227	0.0587	209	0.0162
4003	2.19	6.505	2.745	1.0276	4.5503	7787	0.0712	189	0.0125
6003	2.19	6.234	2.723	1.0832	4.8345	6104	0.0749	206	0.0115
8003	2.19	4.590	1.921	1.3307	6.1599	45299	0.0823	174	0.0091
1004	5.64	10.330	3.225	0.7573	3.9821	2571	0.0479	367	0.0204
3004	5.64	11.061	3.224	0.7262	3.8807	2217	0.0470	162	0.0125
5004	5.64	10.996	3.270	0.8605	4.2376	2872	0.0542	208	0.0090
7004	5.64	9.656	3.007	0.8914	3.9949	4818	0.0728	286	0.0113
2004	5.64	5.137	2.029	1.1005	4.8731	9079	0.0725	171	0.0106
4004	5.64	5.241	2.006	1.1831	5.7248	8881	0.0700	149	0.0135
6004	5.64	4.332	1.621	1.2344	5.7171	73280	0.0693	247	0.0097
8004	5.64	4.102	1.513	0.9960	4.6647	11447	0.0635	229	0.0145
1005	4.45	13.447	3.883	0.8253	4.0599	3501	0.0487	176	0.0093
3005	4.45	13.511	3.877	0.6409	3.4267	1919	0.0498	185	0.0158
5005	4.45	14.254	3.983	0.5919	3.3443	1573	0.0412	379	0.0188
7005	4.45	12.664	3.530	0.7209	3.4108	2254	0.0627	234	0.0141
2005	4.45	6.905	2.819	1.0821	5.1091	14401	0.0596	207	0.0198
4005	4.45	7.582	2.854	1.1565	5.3969	22019	0.0739	120	0.0082
6005	4.45	8.052	2.814	1.0380	4.5759	5560	0.0661	194	0.0175
8005	4.45	7.716	2.625	1.1334	5.2281	15004	0.0719	126	0.0111
1006	3.47	22.577	5.904	0.6620	3.5748	2187	0.0461	124	0.0104
3006	3.47	23.969	6.110	0.6846	3.5918	2297	0.0489	95	0.0089
5006	3.47	24.447	6.016	0.5953	3.5047	1610	0.0399	160	0.0096
7006	3.47	15.243	4.590	0.6908	3.4600	2163	0.0479	159	0.0151
2006	3.47	10.720	4.163	1.0991	5.0680	13017	0.0685	145	0.0074
4006	3.47	10.978	4.331	1.2026	5.1819	17123	0.0796	113	0.0129
6006	3.47	10.780	3.779	0.9404	4.3242	5545	0.0650	91	0.0058
8006	3.47	11.003	4.077	1.9890	4.8770	11236	0.0735	150	0.0129
1007	7.25	10.379	3.482	0.9102	4.3323	9407	0.0614	121	0.0095
3007	7.25	12.608	3.682	0.6581	3.5686	1886	0.0477	210	0.0126
5007	7.25	13.370	3.845	0.8369	3.9683	3436	0.0564	91	0.0060
7007	7.25	14.614	4.352	0.7576	3.8362	3078	0.0544	165	0.0106
2007	7.25	7.498	3.044	1.1423	5.0066	7234	0.0775	108	0.0102
4007	7.25	8.104	2.876	0.9786	4.6054	5099	0.0616	121	0.0080
6007	7.25	6.972	3.100	1.3211	5.4188	44211	0.0906	178	0.0136
8007	7.25	8.481	3.447	0.9318	4.0806	5576	0.0701	236	0.0149
1008	6.49	15.790	4.724	0.7084	3.7484	2120	0.0484	169	0.0136
3008	6.49	15.863	4.567	0.7216	3.7455	2399	0.0491	135	0.0124
5008	6.49	14.159	4.160	0.7074	3.6669	2117	0.0524	220	0.0139
7008	6.49	12.555	3.750	0.7617	3.7309	2712	0.0541	165	0.0117
2008	6.49	10.029	4.027	1.2543	5.3623	15732	0.0803	124	0.0066
4008	6.49	12.983	5.294	0.9984	4.1253	4920	0.0774	239	0.0112
6008	6.49	11.510	4.661	1.1912	5.3313	20832	0.0757	238	0.0139
8008	6.49	6.570	2.341	1.2648	5.4633	24092	0.0792	220	0.0137
1009	4.39	19.015	5.674	0.6028	3.3383	1526	0.0449	255	0.0222
3009	4.39	23.726	6.182	0.6518	3.6257	1859	0.0412	69	0.0110
5009	4.39	23.940	6.347	0.7360	3.8386	2187	0.0496	78	0.0061
7009	4.39	20.354	5.613	0.6735	3.5265	1966	0.0496	134	0.0113

Run No.	depth (cm)	$\bar{\tau}$ (dynes/cm^2)	r.m.s. (dynes/cm^2)	skewness	kurtosis	normal χ^2	normal S-K	log normal χ^2	log normal S-K
2009	4.39	13.295	5.138	1.1302	5.0770	13143	0.0740	77	0.0073
4009	4.39	14.143	5.016	0.9999	4.5808	9094	0.0636	69	0.0064
6009	4.39	15.014	5.282	1.0866	4.8587	7436	0.0709	95	0.0103
8009	4.39	15.878	5.388	1.0295	4.8071	9323	0.0643	78	0.0050
1010	8.44	8.926	3.031	0.8294	4.0073	3875	0.0574	205	0.0154
3010	8.44	9.114	3.112	0.8361	3.8747	3796	0.0564	170	0.0134
5010	8.44	10.837	3.393	0.8897	4.2349	3510	0.0635	120	0.0074
7010	8.44	10.943	3.465	0.9448	4.4182	9759	0.0595	118	0.0144
2010	8.44	4.715	2.541	1.3697	5.0216	20257	0.0994	183	0.0114
4010	8.44	6.135	2.548	1.1531	5.0923	9417	0.0778	124	0.0085
6010	8.44	5.020	2.976	1.1448	4.8305	17956	0.0720	1099	0.0505
8010	8.44	3.617	1.546	1.2462	5.2896	15050	0.0911	145	0.0116
1011	6.89	21.451	4.712	0.7415	3.9248	2408	0.0478	131	0.0103
3011	6.89	20.202	4.439	0.7244	3.6870	2524	0.0559	146	0.0135
5011	6.89	18.825	4.266	0.8155	3.8477	3679	0.0545	119	0.0071
7011	6.89	19.053	4.151	0.7709	3.7025	2622	0.0567	190	0.0091
2011	6.89	12.132	5.742	0.6523	3.1436	2444	0.0533	1183	0.0479
4011	6.89	10.545	4.898	1.2875	5.2724	19647	0.0913	207	0.0124
6011	6.89	11.721	6.276	1.2864	4.8617	12594	0.1099	256	0.0159
8011	6.89	9.423	3.998	1.2369	5.3603	22406	0.0843	143	0.0072
1012	5.39	28.625	6.924	0.6078	3.5862	1780	0.0377	110	0.0116
3012	5.39	24.672	7.401	0.6207	3.4662	1663	0.0455	270	0.0207
5012	5.39	24.357	6.262	0.7014	3.7103	2239	0.0519	93	0.0072
7012	5.39	23.066	6.138	0.7017	3.5356	2402	0.0467	130	0.0121
2012	5.39	16.367	6.254	0.8693	4.1496	4682	0.0561	302	0.0206
4012	5.39	17.104	5.447	0.9918	4.9423	7356	0.0557	76	0.0064
6012	5.39	16.767	5.374	0.9921	5.3740	7695	0.0645	68	0.0036
8012	5.39	18.865	6.884	0.9189	4.0724	6731	0.0638	143	0.0119
1013	9.60	11.683	3.883	0.8913	4.1281	5587	0.0592	166	0.0113
3013	9.60	14.101	5.212	0.7760	3.6472	2943	0.0544	262	0.0180
5013	9.60	13.902	4.241	0.8153	4.1080	3150	0.0544	115	0.0075
7013	9.60	14.093	4.202	0.6975	3.5679	2915	0.0546	188	0.0121
2013	9.60	11.672	4.720	0.9527	4.2678	4258	0.0665	246	0.0142
4013	9.60	12.610	4.239	0.7127	3.5152	2127	0.0520	214	0.0161
6013	9.60	12.981	2.771	1.1200	5.0326	15000	0.0713	106	0.0100
8013	9.60	12.862	5.866	1.1681	4.7164	7246	0.0964	334	0.0220
1014	8.35	17.970	4.872	0.7672	3.8984	4453	0.0515	92	0.0077
3014	8.35	17.285	4.530	0.6373	3.5616	2108	0.0438	140	0.0107
5014	8.35	13.654	4.109	0.8266	3.8866	2919	0.0614	192	0.0117
7014	8.35	17.181	4.777	0.8786	4.2403	3771	0.0581	176	0.0117
2014	8.35	10.331	5.299	1.1716	4.6319	12447	0.0880	228	0.0136
4014	8.35	13.393	6.165	1.5170	5.0589	26976	0.1144	483	0.0342
6014	8.35	15.358	6.587	1.0660	4.1790	6171	0.0893	231	0.0120
8014	8.35	18.613	7.418	0.7647	3.3335	2963	0.0746	388	0.0210
1015	6.34	33.653	7.913	0.5437	3.2463	1271	0.0405	122	0.0078
3015	6.34	32.415	7.658	0.5913	3.3679	1548	0.0421	117	0.0133
5015	6.34	28.326	7.246	0.6258	3.4445	1886	0.0480	114	0.0091
7015	6.34	25.822	6.519	0.6636	3.7402	1747	0.0450	127	0.0061
2015	6.34	23.917	8.570	0.8159	3.5288	4307	0.0644	63	0.0094
4015	6.34	28.314	10.301	0.5947	2.6202	3626	0.0683	175	0.0210
6015	6.34	25.607	8.535	0.8245	3.5181	4514	0.0677	63	0.0062
8015	6.34	29.718	10.147	0.4406	2.4130	2487	0.0578	300	0.0340
1501	3.63	5.735	2.055	0.8213	4.1797	3616	0.0524	518	0.0273
3501	3.63	5.303	1.785	0.8156	3.9506	3346	0.0557	281	0.0199
5501	3.63	5.295	1.700	0.8200	3.9446	4505	0.0553	243	0.0147
7501	3.63	5.909	1.828	0.8090	3.5201	3727	0.0732	488	0.0216
2501	3.63	4.095	1.481	1.1048	5.4393	15428	0.0574	152	0.0137
4501	3.63	3.512	1.429	1.2194	5.5421	27731	0.0723	522	0.0081
6501	3.63	3.231	1.390	1.0123	4.0295	5533	0.0813	285	0.0164
8501	3.63	2.775	1.067	1.3556	5.6377	18236	0.0832	625	0.0324
1502	2.93	9.312	2.898	0.8342	3.8400	3771	0.0553	155	0.0126
3502	2.93	9.657	3.042	0.8801	4.1870	4400	0.0631	185	0.0089
5502	2.93	8.543	2.753	0.8858	3.9929	4500	0.0630	193	0.0119
7502	2.93	9.683	2.871	0.9087	4.3252	7092	0.0524	179	0.0084
2502	2.93	5.692	2.046	1.0335	4.8914	13453	0.0707	202	0.0065
4502	2.93	4.997	2.165	1.2149	4.9147	9265	0.0903	221	0.0124
6502	2.93	4.151	1.775	1.1828	5.4032	38695	0.0739	196	0.0149
8502	2.93	2.657	1.412	1.1613	4.7226	8554	0.0947	426	0.0203

Run No.	depth (cm)	$\bar{\tau}$ (dynes/cm^2)	r.m.s. (dynes/cm^2)	skewness	kurtosis	χ^2 normal	S-K	χ^2 log normal	S-K
1503	2.19	19.047	4.391	0.0903	2.1188	1910	0.0536	514	0.0406
3503	2.19	18.240	4.447	0.1407	2.1158	1518	0.0412	325	0.0319
5503	2.19	15.817	4.216	0.5106	2.7514	1918	0.0528	112	0.0142
7503	2.19	16.308	4.119	0.4155	2.6200	1471	0.0439	123	0.0143
2503	2.19	8.738	2.828	0.9405	4.4455	7052	0.0610	97	0.0048
4503	2.19	7.165	2.960	1.1954	5.2540	30708	0.0793	156	0.0078
6503	2.19	5.423	2.581	1.3088	5.5739	16055	0.0856	203	0.0142
8503	2.19	3.512	1.627	1.5072	6.6674	121872	0.0897	153	0.0110
1504	5.24	7.972	2.614	0.7911	3.7804	2991	0.0573	268	0.0102
3504	5.24	7.259	2.261	0.7096	3.4662	2411	0.0578	288	0.0176
5504	5.24	7.954	2.556	0.8988	4.2686	5089	0.0618	295	0.0095
7504	5.24	8.805	2.653	0.7022	3.4701	2196	0.0538	224	0.0117
2504	5.24	5.618	2.200	1.2889	5.6868	39627	0.0851	187	0.0150
4504	5.24	5.703	2.199	1.2136	5.1727	12450	0.0868	185	0.0152
6504	5.24	4.631	1.792	1.3157	5.8554	24213	0.0830	220	0.0170
8504	5.24	3.911	1.696	1.1549	5.3037	24106	0.0710	263	0.0145
1505	4.27	11.307	3.401	0.8334	3.9708	5171	0.0595	81	0.0060
3505	4.27	11.432	3.415	0.7939	3.8023	3337	0.0613	126	0.0081
5505	4.27	11.220	3.263	0.7069	3.3732	2462	0.0620	225	0.0132
7505	4.27	13.602	3.944	0.6823	3.3203	2974	0.0525	150	0.0118
2505	4.27	8.211	3.076	1.1671	4.9953	19796	0.0755	155	0.0144
4505	4.27	8.379	2.925	1.0694	4.5609	7706	0.0728	181	0.0121
6505	4.27	7.952	2.936	1.1049	4.7510	21249	0.0771	188	0.0170
8505	4.27	7.552	2.930	1.1084	4.6510	9606	0.0731	159	0.0144
1506	3.29	22.482	3.794	-.7628	2.4769	4733	0.1637	4500	0.1491
3506	3.29	20.851	4.172	-.3113	2.0409	2322	0.0928	1502	0.0779
5506	3.29	22.461	3.770	-.7623	2.5813	4591	0.1629	1278	0.0981
7506	3.29	20.878	4.222	-.2880	2.0298	2800	0.1020	1722	0.0860
2506	3.29	15.202	4.408	0.2585	2.2026	2069	0.0477	243	0.0247
4506	3.29	14.591	4.442	0.4339	2.4751	2801	0.0539	178	0.0207
6506	3.29	11.935	4.218	0.8406	3.3490	5366	0.0724	175	0.0109
8506	3.29	9.653	3.582	1.0434	4.2384	7443	0.0772	156	0.0084
1507	6.80	7.339	2.553	0.7897	3.8803	3727	0.0598	292	0.0169
3507	6.80	8.958	2.900	0.8178	3.9189	4530	0.0571	150	0.0119
5507	6.80	10.576	3.223	0.8557	4.0306	5764	0.0585	239	0.0131
7507	6.80	11.078	3.338	0.7764	3.5041	2848	0.0633	254	0.0146
2507	6.80	5.358	2.270	1.2472	5.6365	22526	0.0764	180	0.0071
4507	6.80	7.595	2.773	1.0183	4.5030	5729	0.0684	185	0.0116
6507	6.80	7.304	2.742	1.1661	5.3643	17029	0.0629	777	0.0207
8507	6.80	7.566	2.892	1.2900	5.7816	29666	0.0821	121	0.0094
1508	5.24	14.342	4.352	0.5616	3.0341	2077	0.0439	189	0.0181
3508	5.24	15.124	4.377	0.5236	2.7964	1994	0.0515	164	0.0161
5508	5.24	16.091	4.559	0.8446	2.4791	1603	0.0430	278	0.0204
7508	5.24	15.457	4.689	0.4470	3.5710	2034	0.0481	186	0.0183
2508	5.24	10.577	4.059	0.9067	3.7096	6181	0.0729	73	0.0058
4508	5.24	8.836	3.252	1.0863	4.5939	8846	0.0781	79	0.0073
6508	5.24	7.024	3.316	1.1786	5.0810	22246	0.0797	340	0.0231
8508	5.24	8.008	3.383	0.9924	4.3444	12025	0.0639	193	0.0171
1509	4.18	25.048	6.375	0.5842	3.3483	1420	0.0463	132	0.0083
3509	4.18	25.873	6.918	0.5918	3.3167	1443	0.0471	154	0.0131
5509	4.18	26.891	6.701	0.5949	3.5398	1405	0.0396	129	0.0129
7509	4.18	25.245	6.595	0.6657	3.4909	2120	0.0463	105	0.0112
2509	4.18	15.142	5.082	1.0323	4.8129	6455	0.0614	83	0.0058
4509	4.18	16.799	6.683	0.9756	4.0479	5103	0.0772	222	0.0142
6509	4.18	11.352	4.599	1.4738	6.4054	87898	0.0968	274	0.0197
8509	4.18	12.312	4.583	0.9917	4.4123	6381	0.0715	143	0.0110
1510	7.80	10.996	3.585	0.9929	4.6876	6547	0.0651	115	0.0059
3510	7.80	11.009	3.555	0.8318	3.9177	4929	0.0587	191	0.0129
5510	7.80	12.341	3.745	0.7724	3.9938	3556	0.0503	275	0.0136
7510	7.80	12.986	3.979	0.6694	3.6093	2890	0.0450	243	0.0193
2510	7.80	6.499	2.546	1.2305	5.7653	29355	0.0703	124	0.0065
4510	7.80	7.136	2.724	1.0750	4.6006	7511	0.0751	95	0.0097
6510	7.80	6.846	2.684	1.2411	5.6828	31206	0.0743	70	0.0030
8510	7.80	5.946	2.485	1.1411	5.0010	8300	0.0779	83	0.0095
1511	5.70	17.965	5.359	0.7514	3.8616	2790	0.0541	139	0.0126
3511	5.70	18.400	5.263	0.6743	3.6190	2188	0.0482	156	0.0104
5511	5.70	17.697	5.389	0.7188	3.5784	2396	0.0566	111	0.0082
7511	5.70	18.476	5.560	0.6032	3.0858	1794	0.0518	282	0.0193

Run No.	depth (cm)	$\bar{\tau}$ (dynes/cm^2)	r.m.s. (dynes/cm^2)	skewness	kurtosis	χ^2 normal	S-K	χ^2 log normal	S-K
2511	5.70	12.839	4.902	1.1255	4.9556	9339	0.0783	89	0.0074
4511	5.70	12.925	4.801	1.1099	5.0389	13650	0.0688	102	0.0067
6511	5.70	11.131	3.900	1.1533	5.4202	11043	0.0701	114	0.0047
8511	5.70	10.508	3.842	1.0606	4.6964	7477	0.0755	168	0.0135
1512	4.75	28.243	6.859	0.4501	3.2512	788	0.0294	397	0.0199
3512	4.75	28.663	6.835	0.5512	3.4065	1441	0.0378	181	0.0120
5512	4.75	27.628	6.771	0.4912	3.2040	983	0.0352	207	0.0166
7512	4.75	26.250	6.882	0.6049	3.5197	1641	0.0432	185	0.0126
2512	4.75	16.267	5.604	1.0275	4.7274	6518	0.0675	75	0.0040
4512	4.75	18.171	6.396	1.1037	4.8853	14176	0.0693	89	0.0068
6512	4.75	17.278	5.495	0.9190	4.5959	4061	0.0554	87	0.0098
8512	4.75	16.145	5.537	1.1150	4.9622	10487	0.0740	129	0.0127
1513	8.96	11.541	3.874	0.8218	3.9410	3152	0.0591	173	0.0116
3513	8.96	12.608	3.694	0.8319	4.1660	2856	0.0522	211	0.0118
5513	8.96	13.683	4.057	0.6501	3.4373	1744	0.0446	254	0.0179
7513	8.96	13.103	3.709	0.7043	3.6327	2444	0.0462	175	0.0138
2513	8.96	7.718	3.054	1.0844	4.6986	10380	0.0696	184	0.0156
4513	8.96	10.031	3.583	1.2709	5.6130	24939	0.0842	192	0.0166
6513	8.96	10.531	3.716	1.0146	4.7847	14882	0.0596	153	0.0114
8513	8.96	8.246	3.070	1.1483	5.0338	14335	0.0730	200	0.0126
1514	7.35	21.365	6.686	0.4751	3.2281	1053	0.0260	690	0.0382
3514	7.35	22.317	5.566	0.5382	3.4667	1486	0.0357	208	0.0155
5514	7.35	20.051	6.357	0.6079	3.3286	1534	0.0438	415	0.0209
7514	7.35	22.837	6.052	0.6756	3.6959	1921	0.0449	126	0.0093
2514	7.35	14.168	4.875	1.0922	4.8677	13846	0.0721	130	0.0064
4514	7.35	16.505	6.544	0.7720	3.8965	3884	0.0508	636	0.0283
6514	7.35	14.928	6.106	1.1097	4.2728	7324	0.0948	478	0.0316
8514	7.35	15.431	4.899	1.1019	5.0949	21339	0.0693	138	0.0120
1515	5.85	30.126	7.158	0.4636	3.1155	871	0.0375	220	0.0113
3515	5.85	30.739	7.002	0.5817	3.4225	1342	0.0397	74	0.0068
5515	5.85	26.640	7.740	0.5489	3.3098	1204	0.0413	313	0.0200
7515	5.85	28.863	7.028	0.4886	3.2222	937	0.0363	215	0.0146
2515	5.85	17.683	6.750	1.0362	4.5990	12364	0.0708	77	0.0072
4515	5.85	19.158	6.811	1.0238	4.5000	7295	0.0726	91	0.0050
6515	5.85	18.848	7.496	1.1379	4.7822	15099	0.0741	68	0.0032
8515	5.85	17.486	6.310	1.0437	4.9278	11069	0.0655	90	0.0091
1101	3.38	4.291	1.485	0.8524	3.9855	3419	0.0543	313	0.0203
3101	3.38	3.774	1.275	0.9206	4.4125	6875	0.0677	397	0.0107
5101	3.38	4.621	1.522	0.6795	3.4070	2169	0.0476	420	0.0256
7101	3.38	4.540	1.500	0.8345	4.0595	4838	0.0532	320	0.0190
2101	3.38	3.776	1.486	1.0696	4.5435	6934	0.0694	257	0.0112
4101	3.38	2.884	1.165	1.0415	4.8024	9503	0.0757	261	0.0175
6101	3.38	2.525	1.056	0.9296	3.9267	5086	0.0724	436	0.0211
8101	3.38	2.020	1.040	1.0081	4.6774	5396	0.0697	660	0.0255
1102	2.59	8.207	2.347	0.5824	3.1901	1584	0.0522	297	0.0220
3102	2.59	7.201	2.032	0.6663	3.5396	2021	0.0499	200	0.0145
5102	2.59	6.756	2.018	0.6753	3.7022	2757	0.0407	413	0.0193
7102	2.59	6.514	2.105	0.8164	3.7920	3356	0.0542	248	0.0164
2102	2.59	6.552	2.430	1.0876	4.8088	5977	0.0825	319	0.0188
4102	2.59	6.073	2.392	0.9685	4.5403	8473	0.0609	255	0.0178
6102	2.59	5.333	2.271	1.1801	5.1352	24134	0.0807	221	0.0066
8102	2.59	4.578	1.964	1.1458	5.1270	16652	0.0738	531	0.0228
1103	2.07	12.954	3.141	0.4481	3.1592	916	0.0339	345	0.0200
3103	2.07	12.536	3.163	0.5152	3.1703	1187	0.0370	212	0.0206
5103	2.07	11.705	3.101	0.5979	3.1946	1535	0.0487	201	0.0118
7103	2.07	10.007	2.714	0.6681	3.5116	2074	0.0503	149	0.0150
2103	2.07	12.840	3.793	0.7030	3.1782	3404	0.0624	140	0.0124
4103	2.07	11.428	3.885	0.8978	3.5983	4753	0.0786	219	0.0135
6103	2.07	8.917	3.124	1.0182	4.2969	9252	0.0726	319	0.0237
8103	2.07	8.338	2.513	0.8131	4.0178	3639	0.0560	165	0.0128
1104	4.91	8.283	2.697	0.9335	4.3198	6250	0.0651	170	0.0129
3104	4.91	7.608	2.542	0.9066	4.2611	5379	0.0592	176	0.0130
5104	4.91	7.948	2.447	0.9607	4.8011	6506	0.0563	161	0.0094
7104	4.91	9.844	2.940	0.6674	3.4594	1943	0.0485	333	0.0197
2104	4.91	6.064	2.207	1.1353	5.4017	116280	0.0694	191	0.0068
4104	4.91	5.764	2.175	0.9780	4.7565	7392	0.0563	349	0.0196
6104	4.91	5.238	1.885	0.9927	4.4178	9498	0.0720	185	0.0110
8104	4.91	5.364	1.850	0.9645	4.4021	6098	0.0641	189	0.0102

Run No.	depth (cm)	$\bar{\tau}$ (dynes/cm^2)	r.m.s. (dynes/cm^2)	skewness	kurtosis	χ^2 normal	S-K	χ^2 log normal	S-K
1105	3.93	12.783	3.608	0.5533	3.2188	1481	0.0367	336	0.0235
3105	3.93	12.467	3.675	0.5595	3.1927	1777	0.0343	476	0.0297
5105	3.93	10.987	3.365	0.5719	2.9956	1730	0.0489	433	0.0215
7105	3.93	12.163	3.535	0.6055	3.2259	1733	0.0473	271	0.0171
2105	3.93	9.818	3.436	0.9057	4.0841	6085	0.0669	104	0.0090
4105	3.93	8.796	3.317	1.0903	4.7163	21199	0.0747	97	0.0080
6105	3.93	7.815	2.950	0.9179	4.0622	5448	0.0633	232	0.0143
8105	3.93	8.313	2.842	0.9028	4.1705	5891	0.0630	134	0.0104
1106	3.14	22.053	3.777	-.5824	2.2020	3302	0.1280	2839	0.1152
3106	3.14	22.435	3.689	-.7438	2.3932	3834	0.1473	4099	0.1359
5106	3.14	21.081	4.089	-.3014	2.0354	2676	0.0985	1659	0.0847
7106	3.14	21.030	4.108	-.3780	2.1954	2059	0.0880	1614	0.0749
2106	3.14	14.056	4.513	0.4147	2.3874	2455	0.0566	144	0.0198
4106	3.14	13.685	4.259	0.5935	2.7516	3027	0.0624	129	0.0168
6106	3.14	10.294	3.859	0.6893	3.2055	2602	0.0616	393	0.0252
8106	3.14	6.489	2.482	1.1466	5.4190	7024	0.0654	254	0.0089
1107	6.25	10.417	3.170	0.7003	3.7689	2265	0.0438	312	0.0200
3107	6.25	9.333	2.918	0.7511	3.6887	3255	0.0542	266	0.0153
5107	6.25	9.053	2.905	0.8662	3.9201	3988	0.0582	164	0.0126
7107	6.25	9.996	2.975	0.6179	3.2692	1782	0.0486	384	0.0178
2107	6.25	7.992	2.826	1.1899	4.7962	6883	0.0768	364	0.0296
4107	6.25	8.113	2.874	1.2467	5.4288	24652	0.0768	305	0.0372
6107	6.25	8.174	2.840	1.2208	5.2432	32837	0.0701	230	0.0227
8107	6.25	7.683	2.718	1.1181	4.5617	3271	0.0711	739	0.0473
1108	4.97	13.188	4.077	0.6893	3.5910	1984	0.0474	244	0.0144
3108	4.97	12.255	3.920	0.7684	3.9616	3659	0.0432	262	0.0215
5108	4.97	11.972	3.828	0.6962	3.7214	2044	0.0418	300	0.0233
7108	4.97	15.369	4.324	0.6702	3.4826	2093	0.0468	148	0.0120
2108	4.97	10.866	3.373	0.6024	3.3853	1352	0.0459	384	0.0247
4108	4.97	9.132	2.647	0.6365	3.3204	1669	0.0477	310	0.0180
6108	4.97	11.744	3.968	1.0380	4.9748	8791	0.0719	190	0.0148
8108	4.97	12.460	4.112	0.9045	4.0752	7082	0.0664	191	0.0134
1109	3.87	26.713	6.177	0.4877	3.4414	1656	0.0371	810	0.0391
3109	3.87	23.944	5.362	0.3716	3.0210	593	0.0319	333	0.0185
5109	3.87	24.454	6.409	0.6349	3.5543	1618	0.0433	116	0.0108
7109	3.87	21.224	5.203	0.6470	3.5093	1796	0.0498	137	0.0100
2109	3.87	17.855	5.869	1.0313	4.7506	10084	0.0645	76	0.0049
4109	3.87	17.037	4.926	0.9319	4.3172	4729	0.0643	95	0.0082
6109	3.87	13.669	3.825	0.8657	4.2755	6261	0.0537	106	0.0075
8109	3.87	8.951	2.965	1.1766	5.1677	13963	0.0779	197	0.0168
1110	7.34	10.043	3.258	0.8862	4.1244	4377	0.0584	155	0.0118
3110	7.34	9.605	3.039	0.8221	4.0198	3137	0.0531	239	0.0156
5110	7.34	9.111	3.138	0.6746	3.3914	2161	0.0530	358	0.0220
7110	7.34	10.654	3.287	0.7723	3.6036	2594	0.0606	201	0.0065
2110	7.34	6.946	2.617	1.4962	5.8315	13466	0.1105	1747	0.0866
4110	7.34	7.529	2.773	1.4005	5.6686	12479	0.0887	690	0.0463
6110	7.34	7.476	2.694	1.3596	5.4531	21124	0.0894	567	0.0426
8110	7.34	6.679	2.331	1.3335	4.8609	11264	0.0107	2246	0.1073
1111	5.76	16.034	5.040	0.6294	3.2924	1673	0.0502	274	0.0143
3111	5.76	15.484	5.326	0.5851	3.0845	1693	0.0576	508	0.0275
5111	5.76	15.294	4.293	0.6646	3.5122	2032	0.0457	134	0.0109
7111	5.76	18.610	5.198	0.7839	3.8442	2547	0.0583	150	0.0111
2111	5.76	11.969	4.383	1.3415	6.1710	46877	0.0811	179	0.0109
4111	5.76	13.200	4.370	1.0608	4.8398	7095	0.0710	146	0.0130
6111	5.76	14.185	4.987	1.1870	5.1024	9937	0.0809	238	0.0183
8111	5.76	13.964	4.468	1.1105	4.8497	13319	0.0744	138	0.0100
1112	4.42	25.500	5.894	0.5555	3.3906	1332	0.0355	133	0.0101
3112	4.42	23.783	5.442	0.6040	3.5532	1433	0.0410	92	0.0073
5112	4.42	24.082	5.776	0.4932	3.2484	1004	0.0357	200	0.0138
7112	4.42	24.380	5.796	0.5980	3.5104	1397	0.0416	94	0.0110
2112	4.42	22.231	9.048	1.0297	4.0124	5657	0.0834	356	0.0220
4112	4.42	19.691	6.589	1.0755	4.6839	9481	0.0794	166	0.0155
6112	4.42	19.564	6.455	1.0788	4.8436	10106	0.0725	109	0.0146
8112	4.42	20.193	6.459	1.0638	4.7662	10129	0.0699	144	0.0155
1113	8.11	11.015	3.568	0.8646	4.1497	4460	0.0567	181	0.0116
3113	8.11	12.614	3.705	0.6762	3.6505	1827	0.0456	169	0.0160
5113	8.11	14.878	5.219	0.6951	3.4447	2316	0.0580	408	0.0277
7113	8.11	14.573	4.143	0.6846	3.7000	1945	0.0427	208	0.0167

Run No.	depth (cm)	$\bar{\tau}$ (dynes/cm^2)	r.m.s. (dynes/cm^2)	skewness	kurtosis	χ^2 normal	S-K	χ^2 log normal	S-K
2113	8.11	8.113	2.889	1.3271	5.7711	81534	0.7920	251	0.0223
4113	8.11	10.181	3.688	1.1960	5.1241	12817	0.0743	278	0.0194
6113	8.11	9.595	3.614	0.6999	3.2409	2219	0.0621	788	0.0331
8113	8.11	8.880	3.812	1.2523	5.2555	21093	0.0734	802	0.0501
1114	6.71	22.251	5.643	0.6139	3.5544	1745	0.0441	127	0.0127
3114	6.71	20.631	5.581	0.6888	3.7638	2841	0.0433	124	0.0125
5114	6.71	21.517	5.861	0.5332	3.1820	1126	0.0400	265	0.0167
7114	6.71	25.808	6.168	0.5925	3.5808	1560	0.0382	97	0.0108
2114	6.71	15.410	5.944	1.0186	4.5947	9463	0.0680	83	0.0097
4114	6.71	16.906	6.271	1.0385	4.6330	7746	0.0666	86	0.0065
6114	6.71	16.765	5.557	1.0501	4.7380	7531	0.0713	90	0.0105
8114	6.71	16.339	5.498	1.1237	4.9031	14489	0.0674	267	0.0202
1115	5.36	33.555	7.732	0.5895	3.4786	1525	0.0427	110	0.0066
3115	5.36	30.415	7.231	0.6676	3.6083	1889	0.0494	113	0.0123
5115	5.36	31.082	7.357	0.6294	3.5992	2013	0.0450	83	0.0042
7115	5.36	34.762	7.708	0.5930	3.3888	1424	0.0419	113	0.0083
2115	5.36	21.668	7.710	1.0747	4.5791	6742	0.0798	127	0.0132
4115	5.36	21.891	7.198	1.0138	4.6385	8654	0.0633	116	0.0116
6115	5.36	23.054	7.559	0.9736	4.6816	9205	0.0639	84	0.0074
8115	5.36	22.774	7.960	1.1679	5.1499	16498	0.0715	162	0.0096
1201	3.20	4.113	1.110	0.9394	4.3052	4155	0.0685	539	0.0295
3201	3.20	3.986	1.133	0.9525	4.5040	7473	0.0509	293	0.0179
5201	3.20	3.797	1.036	0.6509	3.4817	2221	0.0561	471	0.0264
7201	3.20	3.939	1.120	0.8844	3.8439	3983	0.0688	278	0.0199
2201	3.20	3.341	1.167	1.1658	5.4207	9149	0.0703	258	0.0132
4201	3.20	2.593	0.963	1.2194	5.7858	68461	0.0720	291	0.0125
6201	3.20	1.149	0.462	1.3181	6.3464	99462	0.0707	319	0.0120
8201	3.20	1.955	0.795	1.2353	5.3178	21043	0.0815	334	0.0108
1202	2.41	7.012	1.920	0.8234	3.6836	3695	0.0600	382	0.0241
3202	2.41	6.078	1.507	0.6555	3.2957	1953	0.0555	220	0.0121
5202	2.41	7.325	1.821	0.8506	3.7360	3864	0.0770	535	0.0358
7202	2.41	6.416	1.626	0.9146	4.3577	6457	0.0632	220	0.0161
2202	2.41	5.360	2.052	1.0755	4.7457	13410	0.0730	218	0.0070
4202	2.41	3.882	1.613	1.0134	4.5315	8663	0.0742	355	0.0173
6202	2.41	4.204	1.696	0.9496	4.3063	5338	0.0696	575	0.0167
8202	2.41	3.801	1.657	1.0168	4.7012	6819	0.0581	615	0.0347
1203	1.92	11.511	2.916	0.6477	3.2511	1873	0.0575	186	0.0101
3203	1.92	10.291	2.637	0.6463	3.3150	1795	0.0515	130	0.0082
5203	1.92	11.272	2.888	0.5890	3.3234	1546	0.0424	264	0.0191
7203	1.92	9.656	2.608	0.7076	3.6397	2154	0.0565	170	0.0100
2203	1.92	8.400	2.597	1.0331	4.6622	6719	0.0669	225	0.0160
4203	1.92	7.626	2.331	1.0133	4.5434	7670	0.0671	362	0.0218
6203	1.92	7.269	2.105	0.9513	4.6874	18914	0.0493	163	0.0136
8203	1.92	6.897	1.815	1.0049	4.6442	10864	0.0633	413	0.0255
1204	4.69	6.648	1.817	0.7398	3.9797	5600	0.0439	321	0.0155
3204	4.69	5.965	1.670	1.0435	4.8288	17492	0.0637	312	0.0183
5204	4.69	6.231	1.804	0.7771	3.8764	3323	0.0523	304	0.0171
7204	4.69	6.299	1.773	0.8657	4.0412	9819	0.0652	373	0.0225
2204	4.69	5.534	1.984	1.0194	4.6983	8448	0.0736	168	0.0116
4204	4.69	5.372	1.807	0.9225	3.9346	5369	0.0658	266	0.0161
6204	4.69	6.732	2.166	0.8073	4.1551	3999	0.0486	401	0.0195
8204	4.69	6.106	2.002	0.7835	3.8080	3538	0.0514	260	0.0150
1205	3.35	11.265	2.799	0.7473	3.6548	2682	0.0582	127	0.0113
3205	3.35	10.340	2.547	0.7918	3.9065	3270	0.0521	234	0.0120
5205	3.35	10.480	2.597	0.8380	4.1375	4336	0.0542	124	0.0061
7205	3.35	9.556	2.462	0.8140	3.9954	3679	0.0535	237	0.0132
2205	3.35	9.395	3.172	1.0527	4.6234	10585	0.0752	124	0.0120
4205	3.35	7.060	2.407	0.8492	3.9915	4165	0.0558	236	0.0132
6205	3.35	6.135	2.179	1.0616	4.9884	10548	0.0710	135	0.0081
8205	3.35	5.179	1.967	0.9987	4.6683	10032	0.0589	230	0.0182
1206	2.80	16.871	3.725	0.4528	2.7995	1366	0.0411	104	0.0112
3206	2.80	18.099	3.992	0.2559	2.4221	1096	0.0339	145	0.0171
5206	2.80	19.577	3.856	0.3734	2.6058	1487	0.0394	109	0.0127
7206	2.80	18.116	3.971	0.3111	2.5955	1510	0.0476	189	0.0207
2206	2.80	13.292	3.943	0.9713	4.5607	7540	0.0639	134	0.0074
4206	2.80	11.118	3.508	1.0551	4.5653	5499	0.0767	218	0.0181
6206	2.80	10.575	3.317	1.0766	4.7918	10050	0.0715	253	0.0118
8206	2.80	11.351	3.280	1.1240	4.8669	9925	0.0818	451	0.0295

Run No.	depth (cm)	$\bar{\tau}$ (dynes/cm^2)	r.m.s. (dynes/cm^2)	skewness	kurtosis	χ^2 normal	S-K	χ^2 log normal	S-K
1207	5.49	9.095	2.389	0.6539	3.4936	1846	0.0491	161	0.0094
3207	5.49	9.168	2.420	0.6773	3.6744	2737	0.0503	173	0.0089
5207	5.49	8.637	2.260	0.6658	3.7470	1597	0.0442	169	0.0098
7207	5.49	8.036	2.299	0.9046	4.0272	4367	0.0638	280	0.0196
2207	5.49	7.153	2.412	1.0581	5.0036	14133	0.0669	164	0.0077
4207	5.49	6.224	2.132	1.2316	6.0916	13133	0.0649	251	0.0093
6207	5.49	5.580	2.070	1.1622	5.5993	34364	0.0730	221	0.0080
8207	5.49	4.288	1.673	0.9770	4.7594	8873	0.0658	1681	0.0221
1208	4.15	15.053	3.811	0.4647	2.9902	1069	0.0381	162	0.0147
3208	4.15	14.952	3.794	0.5458	2.9854	1598	0.0488	135	0.0120
5208	4.15	14.414	3.817	0.4978	2.8120	1295	0.0387	208	0.0177
7208	4.15	16.919	4.039	0.3667	2.6445	1160	0.0434	179	0.0152
2208	4.15	11.889	3.721	1.0789	5.0033	12408	0.0683	122	0.0092
4208	4.15	8.886	2.963	1.1690	5.4957	18216	0.0686	124	0.0079
6208	4.15	9.386	3.012	0.9734	4.4752	9978	0.0643	231	0.0144
8208	4.15	9.685	3.087	1.1003	4.8669	9003	0.0752	354	0.0228
1209	3.54	22.233	3.617	-.5112	2.4110	3281	0.1239	2894	0.1075
3209	3.54	19.332	3.912	0.0744	2.2002	1043	0.0359	256	0.0290
5209	3.54	22.030	3.496	-.4355	2.0407	2475	0.1036	1878	0.0904
7209	3.54	22.893	3.397	-.7587	2.4573	4165	0.1530	4290	0.1417
2209	3.54	14.187	4.403	1.0494	4.6672	11849	0.0729	194	0.0182
4209	3.54	12.662	4.058	1.0005	4.2553	5678	0.0747	268	0.0213
6209	3.54	13.425	4.250	1.0068	4.5609	10247	0.0685	106	0.0103
8209	3.54	12.607	3.808	1.1090	4.8932	9233	0.0727	272	0.0162
1210	6.43	8.509	2.252	0.8575	4.0932	5188	0.0547	138	0.0069
3210	6.43	7.851	2.233	0.8515	4.2471	3977	0.0530	182	0.0099
5210	6.43	10.542	2.668	0.5984	3.5179	1449	0.0394	236	0.0184
7210	6.43	10.475	2.732	0.7553	3.6543	2576	0.0558	202	0.0176
2210	6.43	5.277	1.951	1.0801	4.9018	10665	0.0705	408	0.0218
4210	6.43	6.673	2.172	1.0896	4.8360	12045	0.0759	306	0.0225
6210	6.43	5.353	1.800	0.8777	3.9899	3856	0.0629	126	0.0088
8210	6.43	5.028	1.500	0.9777	3.0100	4086	0.0701	135	0.0100
1211	5.12	15.097	3.607	0.5304	2.9455	1490	0.0420	194	0.0139
3211	5.12	14.154	3.416	0.5970	3.2774	1911	0.0451	116	0.0092
5211	5.12	15.674	3.897	0.5300	2.9776	1728	0.0444	83	0.0101
7211	5.12	16.505	3.835	0.4159	2.7856	1223	0.0398	116	0.0143
2211	5.12	10.622	3.397	0.9008	4.1586	7136	0.0593	123	0.0112
4211	5.12	9.821	3.232	1.0449	4.6199	5163	0.0723	168	0.0118
6211	5.12	10.642	3.232	0.9959	4.3250	5624	0.0737	259	0.0212
8211	5.12	9.297	2.746	1.1157	5.1996	14474	0.0654	189	0.0112
1212	4.30	18.279	3.864	0.1916	2.4374	831	0.0241	178	0.0224
3212	4.30	18.750	3.951	0.1319	2.2481	961	0.0318	191	0.0231
5212	4.30	21.649	3.960	-0.4480	2.1448	2930	0.1146	2193	0.0985
7212	4.30	21.601	3.728	-.3439	2.1053	2203	0.0903	1544	0.0789
2212	4.30	12.247	3.923	0.9369	4.3336	4035	0.0642	107	0.0100
4212	4.30	12.319	4.030	0.9354	4.1873	4470	0.0603	219	0.0131
6212	4.30	14.396	4.366	0.9531	4.3121	5927	0.0640	130	0.0079
8212	4.30	14.057	4.126	1.0227	4.5209	6860	0.0719	205	0.0167
1213	7.39	8.022	2.212	0.7016	3.5493	2258	0.0500	217	0.0098
3213	7.39	7.979	2.204	0.7058	3.8700	5110	0.0398	335	0.0167
5213	7.39	10.916	2.887	0.7519	3.9594	3944	0.0463	124	0.0086
7213	7.39	7.504	2.021	0.7519	3.8500	2931	0.0563	138	0.0101
2213	7.39	7.549	2.540	1.0303	4.9684	127772	0.0664	232	0.0117
4213	7.39	10.385	3.323	0.9429	4.3436	649	0.0666	117	0.0086
6213	7.39	8.183	2.849	1.1927	5.4554	18000	0.0744	169	0.0105
8213	7.39	7.195	2.758	1.9431	4.9350	1079	0.0814	155	0.0108
1214	5.49	14.380	3.662	0.4488	3.1326	994	0.0273	309	0.0243
3214	5.49	13.521	3.393	0.4968	3.1267	1140	0.0332	263	0.0169
5214	5.49	15.600	3.896	0.4428	2.8424	1242	0.0372	195	0.0217
7214	5.49	16.141	3.756	0.4431	2.8761	1296	0.0416	88	0.0099
2214	5.49	13.061	4.069	1.0218	4.7845	12285	0.0572	98	0.0072
4214	5.49	17.007	5.243	1.0136	4.3178	6576	0.0721	240	0.0162
6214	5.49	10.326	3.614	1.2963	5.5881	17941	0.0810	349	0.0173
8214	5.49	7.805	2.653	1.2406	5.4697	25372	0.0770	202	0.0119
1215	4.72	25.533	1.696	-2.9360	12.0142	150000	0.0435	212000	0.4061
3215	4.72	24.367	2.663	-1.4685	4.2144	11584	0.2632	20024	0.2591
5215	4.72	26.016	0.871	-3.7062	19.2450	175000	0.3019	187000	0.4963
7215	4.72	26.192	0.253	-1.4601	8.3287	62969	0.3321	24764	0.4471

Run No.	depth (cm)	$\bar{\tau}$ (dynes/cm^2)	r.m.s. (dynes/cm^2)	skewness	kurtosis	χ^2 normal	S-K	χ^2 log normal	
2215	4.72	12.755	3.914	0.9144	4.5640	5385	0.0534	65	0.0067
4215	4.72	13.472	4.273	0.9951	4.4634	8088	0.0701	109	0.0121
6215	4.72	14.068	4.398	1.0552	4.6927	12802	0.0689	258	0.0208
8215	4.72	13.725	4.946	1.0906	4.5060	8231	0.0820	218	0.0126